NASA CR-165,603

NASA CR-165603

ELECTRIC THRUSTER RESEARCH

Prepared for

LEWIS RESEARCH CENTER

NATIONAL AERONAUTICS AND SPACE ADMINISTRATION

GRANT NSG 3011

December 1981

Harold R. Kaufman and Raymond S. Robinson
Department of Mechanical Engineering
Colorado State University
Fort Collins, Colorado

1. Report No.
NASA CR-165603

2. Government Accession No.

3. Recipient's Catalog No.

4. Title and Subtitle
Electric Thruster Research

5. Report Date
December, 1981

6. Performing Organization Code

7. Author(s)
Harold R. Kaufman and Raymond S. Robinson

8. Performing Organization Report No.

10. Work Unit No.

9. Performing Organization Name and Address
Department of Mechanical Engineering
Colorado State University
Fort Collins, Colorado 80523

11. Contract or Grant No.
NSG 3011

13. Type of Report and Period Covered
Contr. Report

12. Sponsoring Agency Name and Address
National Aeronautics and Space Administration
Washington, D.C. 20546

14. Sponsoring Agency Code

15. Supplementary Notes
Contr. Manager, Vincent K. Rawlin
NASA Lewis Research Center
Cleveland, Ohio 44135

16. Abstract

The first part of this report is a continuing study of the multipole discharge chamber of an electrostatic ion thruster, with the ultimate goal of reducing discharge losses. No reductions in discharge losses were obtained in any of a variety of bias experiments conducted with a multipole discharge chamber of an electrostatic thruster, despite repeated demonstration of anode potentials more positive than the bulk of the discharge plasma. The most promising trend in these bias experiments was the reduction of the penalty associated with biased anode operation as the magnetic integral above the biased anodes was increased.

The second part is a continuing study of the hollow cathode. The use of hollow cathodes with assembled construction, as opposed to welded construction, appears practical. This approach is particularly promising for larger cathodes at higher emission, where the thermal expansion problems would be more serious with the present welded construction. Successful operation without emissive oxide offers the opportunity for accurate analyses of the electron emission and heat flow in a hollow cathode. Operation without oxide also offers the possibility of more reliable starting in programs where repeated or prolonged exposure to air after operation is a necessity.

The study of the Hall-current accelerator in the last two parts represents a sharp departure from past work of this Grant. The experimental configuration of the Hall-current thruster that was tested had a uniform field throughout the ion generation and acceleration regions. To obtain reliable ion generation, it was necessary to reduce the magnetic field strength, to the point where excessive electron backflow was required to establish ion acceleration. This problem should be resolvable by using a nonuniform magnetic field strength, with ion generation restricted to a reduced field strength region. It also may be resolvable by the use of a more sophisticated electrode geometry in the ion generation region.

The theoretical study of ion acceleration with closed electron drift paths resulted in two classes of solutions. One class has the continuous potential variation in the acceleration region that is normally associated with a Hall-current accelerator. The other class has an almost discontinuous potential step near the anode end of the acceleration region. This step includes a significant fraction of the total acceleration potential difference. This latter class corresponds to the anode-layer accelerator in U.S.S.R. literature.

17. Key Words (Suggested by Author(s))
Electric propulsion
Ion sources
Plasma physics

18. Distribution Statement
Unclassified-Unlimited

19. Security Classif. (of this report)
Unclassified

20. Security Classif. (of this page)
Unclassified

21. No. of Pages

22. Price*

* For sale by the National Technical Information Service, Springfield, Virginia 22161

N82-24285#

TABLE OF CONTENTS

LIST OF FIGURES

I. INTRODUCTION

There are four major parts to this annual report. The first is a continuing study of the multipole discharge chamber of an electrostatic ion thruster. This portion of the effort is directed at furthering the understanding of discharge-chamber operation, with the ultimate goal of reducing discharge losses.

The second part is a continuing study of the hollow cathode, with emphasis on assembled (nonwelded) construction and operation without emissive oxide.

The third and fourth parts are devoted to the Hall-current accelerator, and represent a significant departure from past ion thruster work in this Grant. The third part is an experimental study of a Hall-current accelerator, while the fourth part is a general theoretical study of ion acceleration with a transverse magnetic field and a closed electron drift path. The Appendix is also related to the last two parts in that it includes five summary papers on ion accelerators wtih closed electron drift paths. These papers were originally published in the U.S.S.R. and are reproduced here together with translations.

II. ION CONTAINMENT

by Larry E. Frisa

The efficiency of an ion thruster is important for electric space propulsion. The discharge loss (the power used to generate ions) is a major factor in this efficiency. Reduction of the discharge loss, then, would permit ion thrusters to become more efficient.

Discharge-loss correlations have indicated that, for similar utilization conditions, the volume production cost for ions is essentially constant.[1] This means that discharge losses can be reduced, again for similar utilization conditions, only by extracting a larger fraction of the ions produced. This fraction of ions extracted could be increased if some portion of the discharge chamber walls could be configured and operated so that ions were reflected back into the chamber, instead of the usual recombination with electrons that occurs at surfaces.

Such ion reflection, or containment, has been proposed in the past. Discharge losses have been low enough in some designs to indicate that some degree of ion containment might have been attained.[2-3] On the other hand, preliminary anode bias experiments have failed to indicate any significant degree of containment.[4] The experiments described herein were further attempts to determine if ion containment could be obtained in a discharge chamber.

Apparatus

The thruster used for the ion containment experiments is rectangular in shape and has been described in previous publications.[5-6] Argon gas was used as the propellant. The rectangular design of this thruster makes it easy to change anodes, hence convenient to use for ion containment experiments. Except for a short general description, the apparatus description herein will emphasize the aspects directly involved in these experiments.

The internal dimensions of the discharge chamber (circumscribed by the screen grid and pole pieces) are 7.5 cm deep, 10 cm wide, and 45 cm long. Two cross sections with different anodes are shown in Fig. 2-1. The 45 cm dimension is normal to the paper in Fig. 2-1, and there are no pole pieces or anodes at the ends of the discharge chamber. The ion-beam extraction area is 5 × 40 cm, with a 58% open screen grid within this area.

Anodes. The first type of back anodes used in the ion containment experiments were the narrow anodes (Fig. 2-1 (a)), which were part of the original design. The anode surfaces exposed directly to the discharge plasma were 0.4 cm wide, while the length was 44.5 cm. In this original configuration, no anode was installed behind the cathode. (Thus for Fig. 2-20, only three back anodes were used. All other tests used four anodes.) The second type of anodes used (Fig. 2-1 (b)) are called wide anodes. These wide anodes had 2.0 cm wide strips attached to the discharge side of the narrow anodes, and the same 44.5 cm length as the narrow anodes. These wide strips were slightly bent in cross section, as indicated in Fig. 2-1 (b).

Thermal warping problems with the designs of Figs. 2-1 (a) and (b) were indicated by increasing discharge losses with duration of operation, distortion after use, and, for the wide anodes, shorting to the pole pieces. Because of these problems, a new strip design was fabricated using 1.6 mm thick stainless steel, 43.2 cm long. This strip anode design is compared to the narrow anode design in Fig. 2-2, and

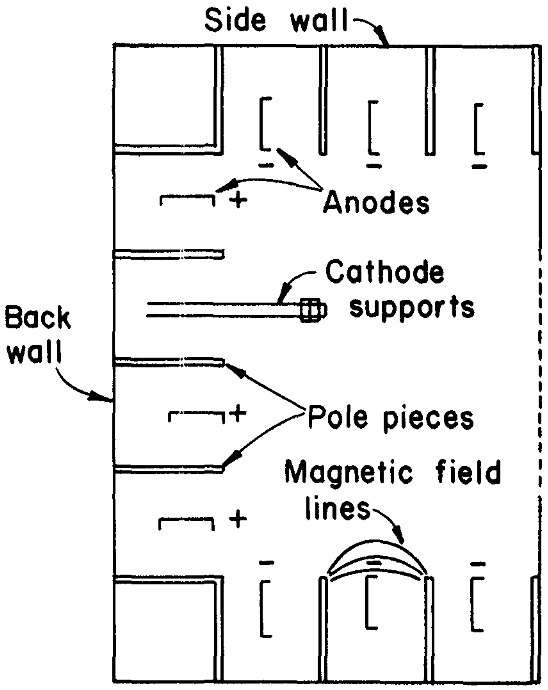

(a) Narrow anodes

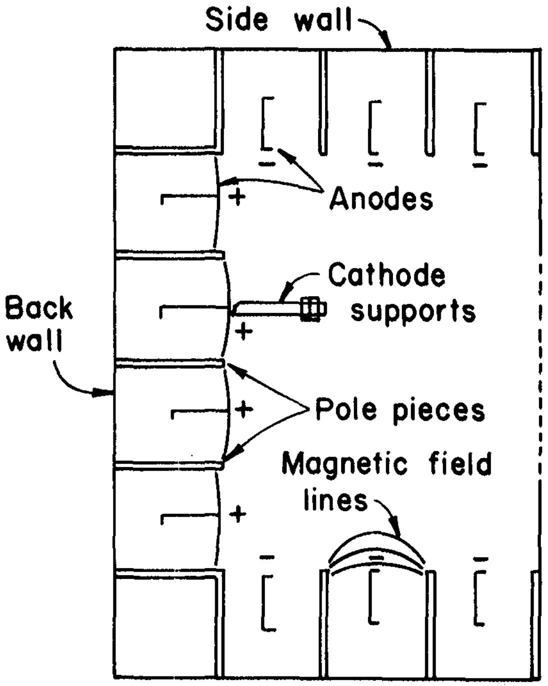

(b) Wide anodes

Fig. 2-1. Discharge-chamber cross section.

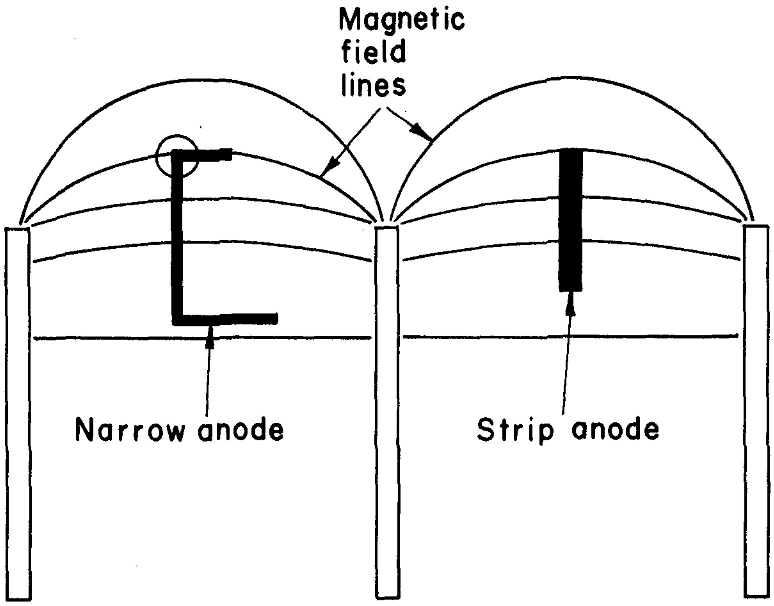

Fig. 2-2. Comparison of narrow and strip anodes between pole pieces.

shown in more detail in Fig. 2-3. The strip anodes were held in place using support brackets of 0.55 mm thick stainless steel, spot welded to the heavier anode strips. The bracket at one end of each anode was slotted to allow for thermal expansion.

Magnetic fields. The thruster was operated with two basic magnetic field configurations. The first was that of the original design, and used six Alnico V permanent magnets, 6.4 mm diameter and 25 mm long, between each pair of pole pieces. In this configuration, field strength between all pairs of pole pieces was approximately the same. The mean calibration value for the magnets used in the original configuration was, after disassembly, $18.9 \pm 1.4 \times 10^{-4}$ T. (This was a measurement at a location 2.8 cm radially out from the center of the magnet, and serves as a relative indication of magnet strength.)

The second configuration was one in which the number of magnets in the back wall (both "back center" and "back corner" locations in Fig. 2-4) were doubled. As a more minor change at the same time, the original magnets were remagnetized, giving a calibration value of $20.7 \pm 0.3 \times 10^{-4}$ T. Also, the new magnets added to the back were from a different shipment, resulting in a remagnetized calibration value of $19.5 \pm 0.5 \times 10^{-4}$ T.

Magnetic field measurements were taken between adjacent pairs of pole pieces. This was done by centering the magnetic probe between a pair of pole pieces, then moving the probe (while taking measurements) parallel to the 2.5 cm pole-piece faces (see Fig. 2-4). The magnetic field distributions obtained in this manner for the end location (see Fig. 2-4) are shown in Figs. 2-5 and 2-6 for the first and second magnetic field configurations. The increase of the maximum from

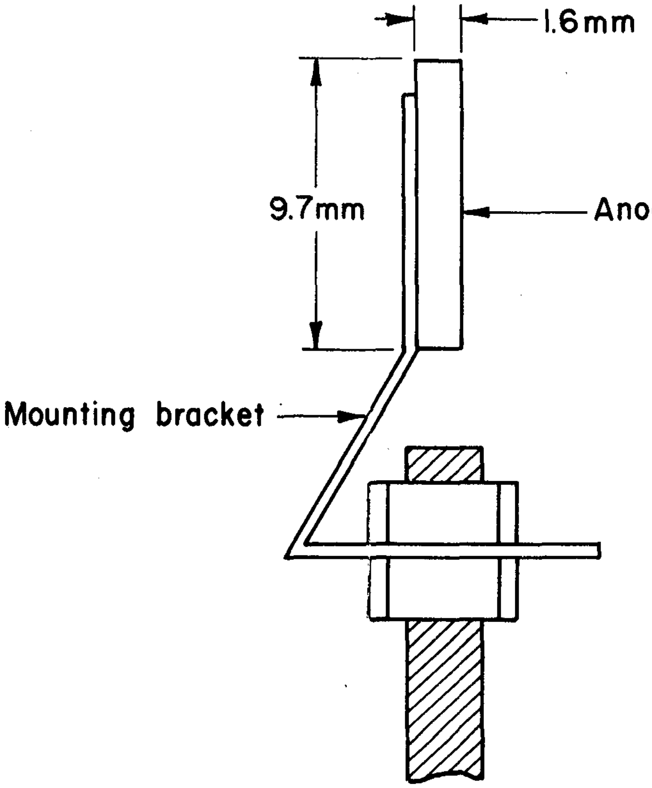

End view

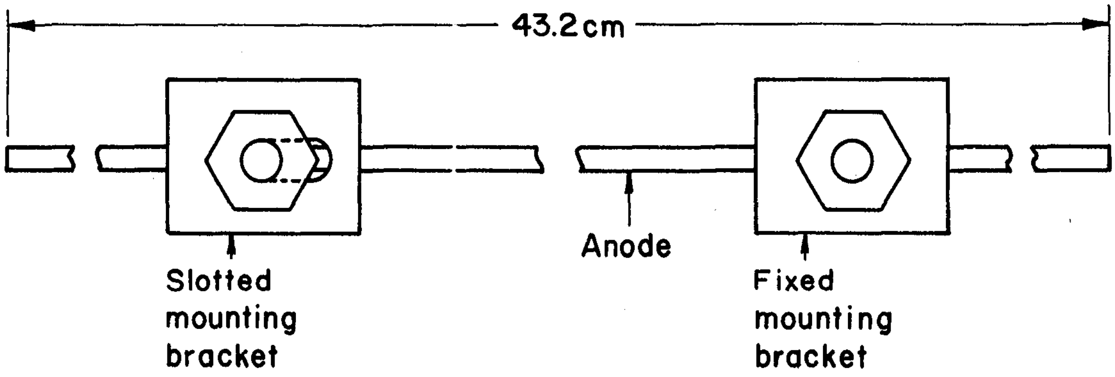

Bottom view

Fig. 2-3. Design of strip anodes.

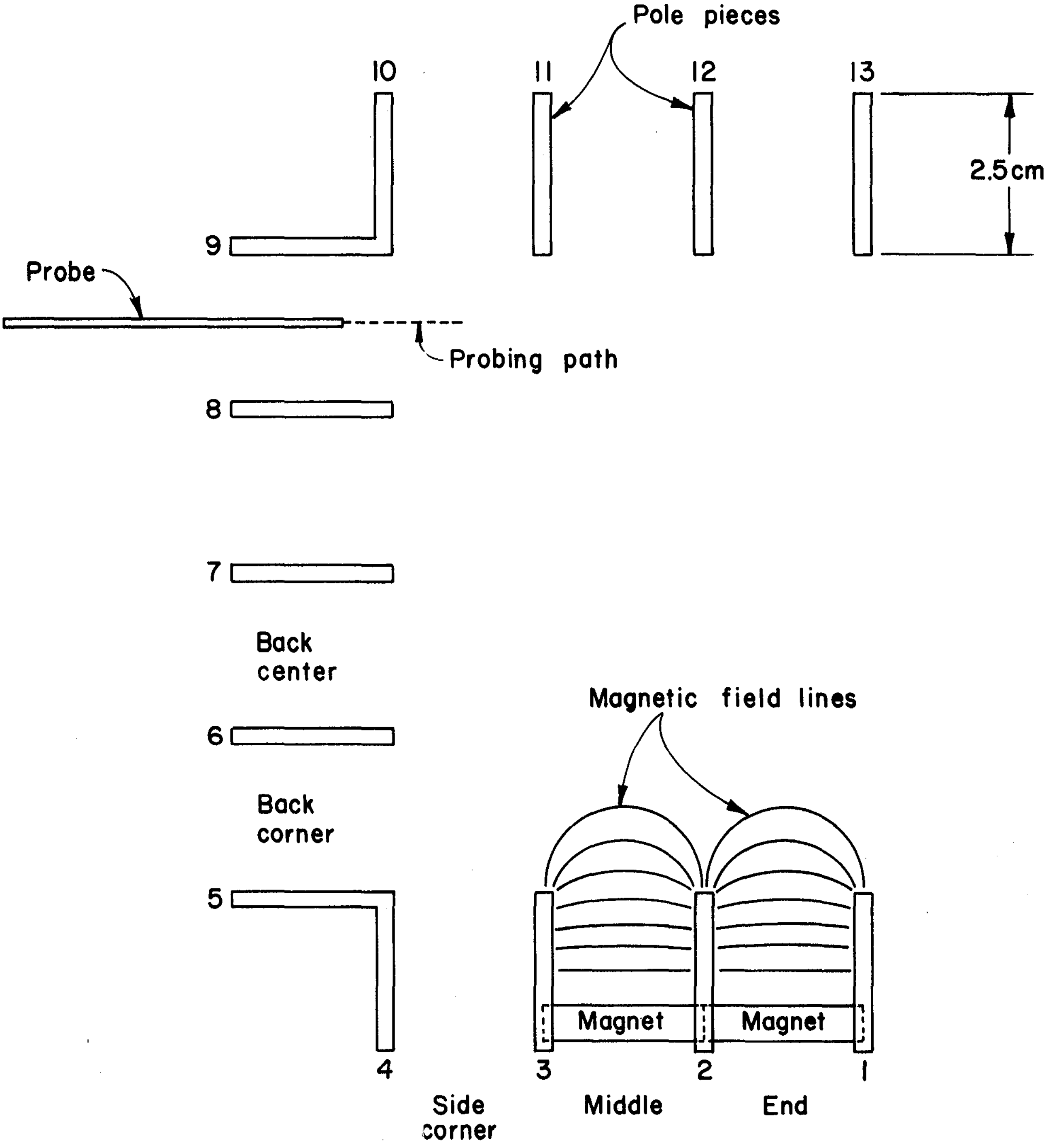

Fig. 2-4. Location of probe between pole pieces. Pole pieces numbering and anode locations are also shown.

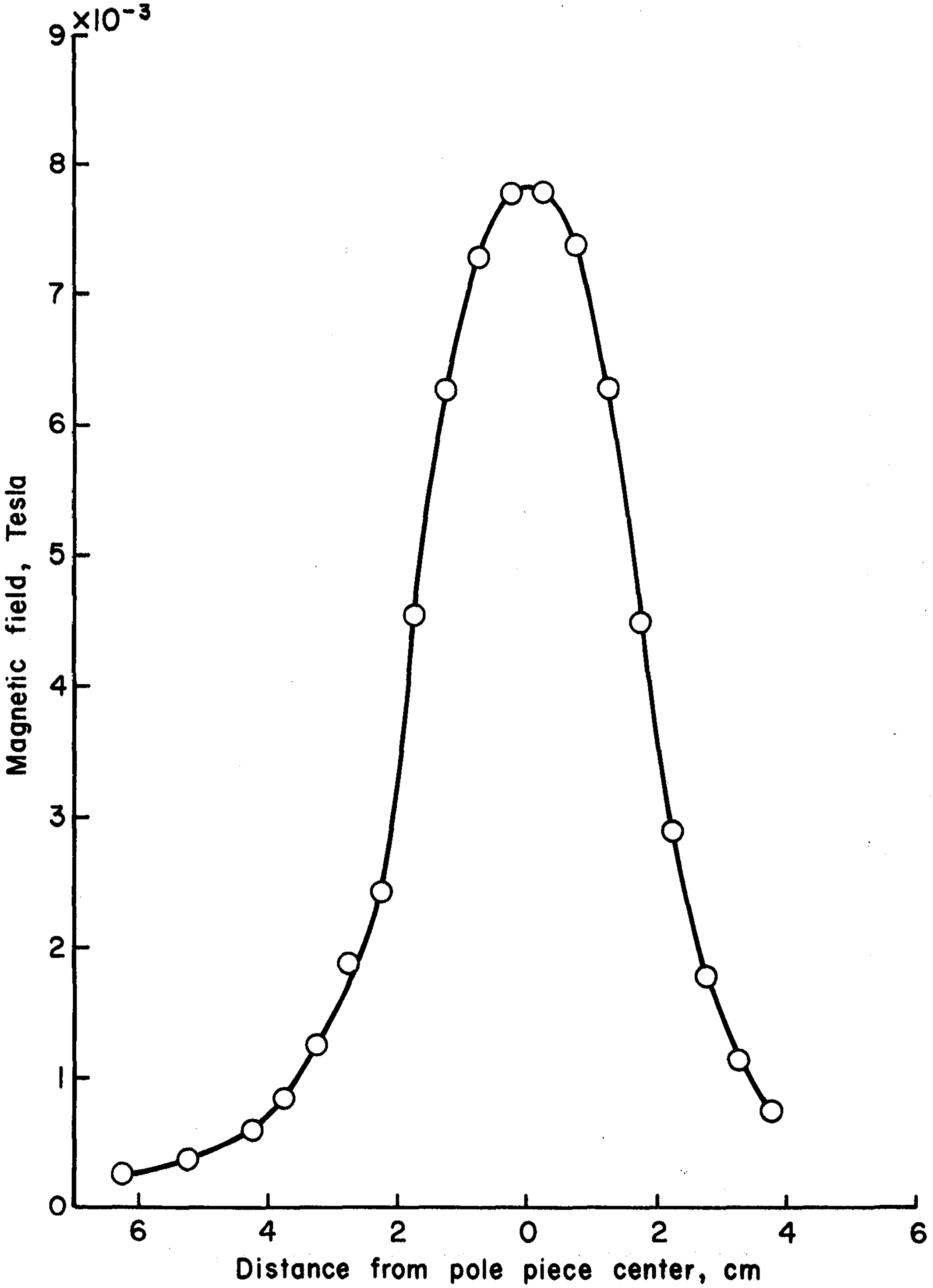

Fig. 2-5. Magnetic field distribution for an end anode location and the first magnetic field configuration.

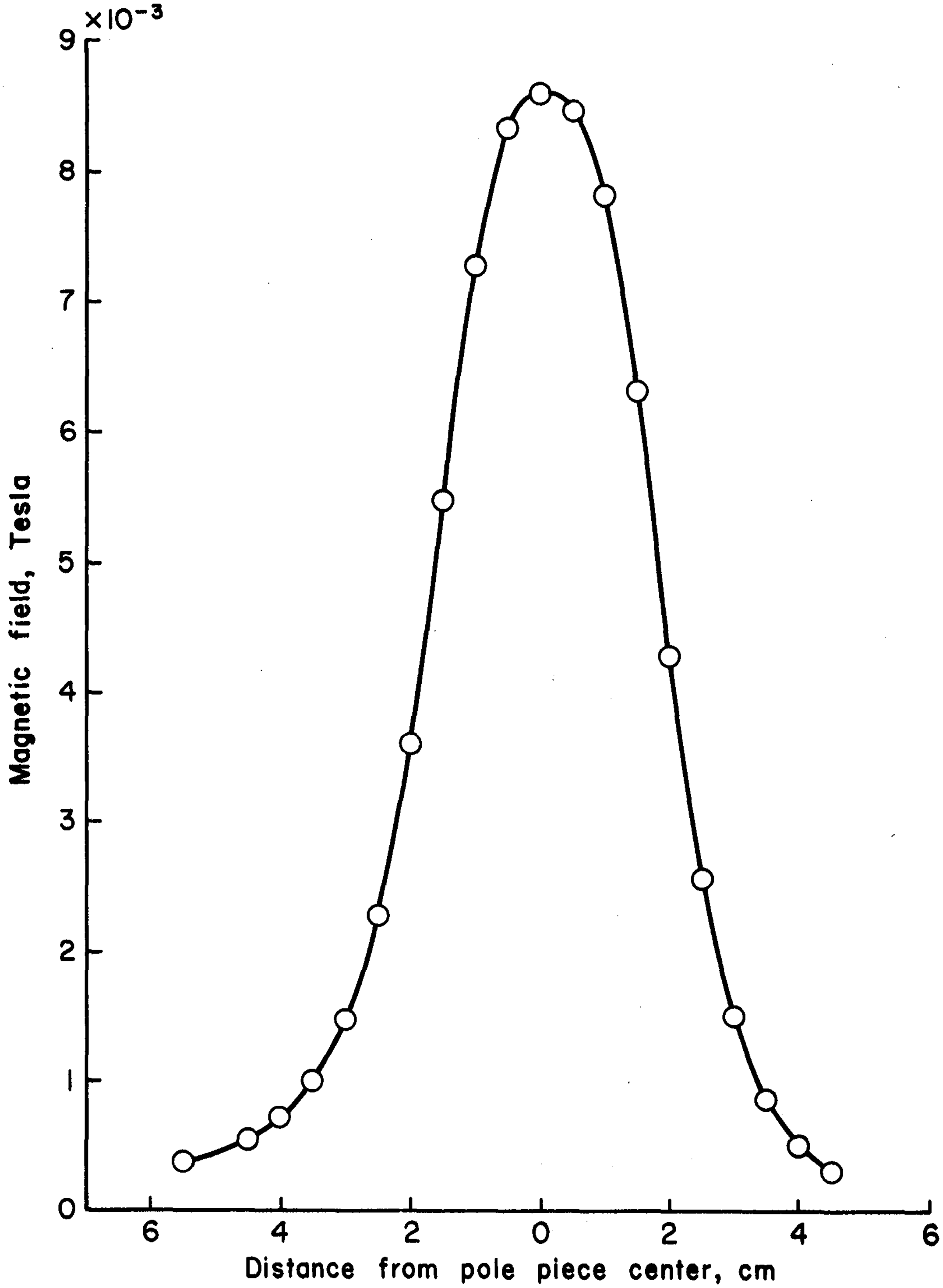

Fig. 2-6. Magnetic field distribution for an end anode location and the second magnetic field configuration.

7.8×10^{-3} to 8.6×10^{-3} T was associated with the remagnetization described earlier. The magnetic field distributions for the other locations of the second configuration are shown in Figs. 2-7 through 2-10. These distributions were used to calculate the magnetic-field integral values ($\int Bdx$) between the anodes and the bulk of the plasma. In Figs. 2-5 through 2-10, the center of the discharge chamber is always to the right.

Ferromagnetic powder maps were also made of the two configurations and are shown in Figs. 2-11 and 2-12. These maps are helpful in understanding qualitative differences between the fields for the two configurations, particularly around pole pieces.

The total flux through a magnet was calculated by measuring the magnetic field in a plane normal to the magnet's axis, and passing through its center. These measurements were found to agree with

$$B = K/[16 + (r/R)^2]^{3/2} , \tag{2-1}$$

where B is the magnetic flux density, R is the magnet's radius, r is the radial distance from the magnet axis, and K is a constant selected to fit the experimental data from a single magnet. Taking the mean value of K, the total flux through one magnet was found to be $3.26 \pm 0.28 \times 10^{-5}$ T-m^2 (Webers). The corresponding flux density in one magnet was found to be 1.01 ± 0.09 T. This procedure was checked by integrating the magnetic flux between two pole pieces and dividing by the number of magnets. This latter method gave the flux through one magnet as $3.24 \pm 0.10 \times 10^{-5}$ T-m^2. The two procedures were thus in excellent agreement.

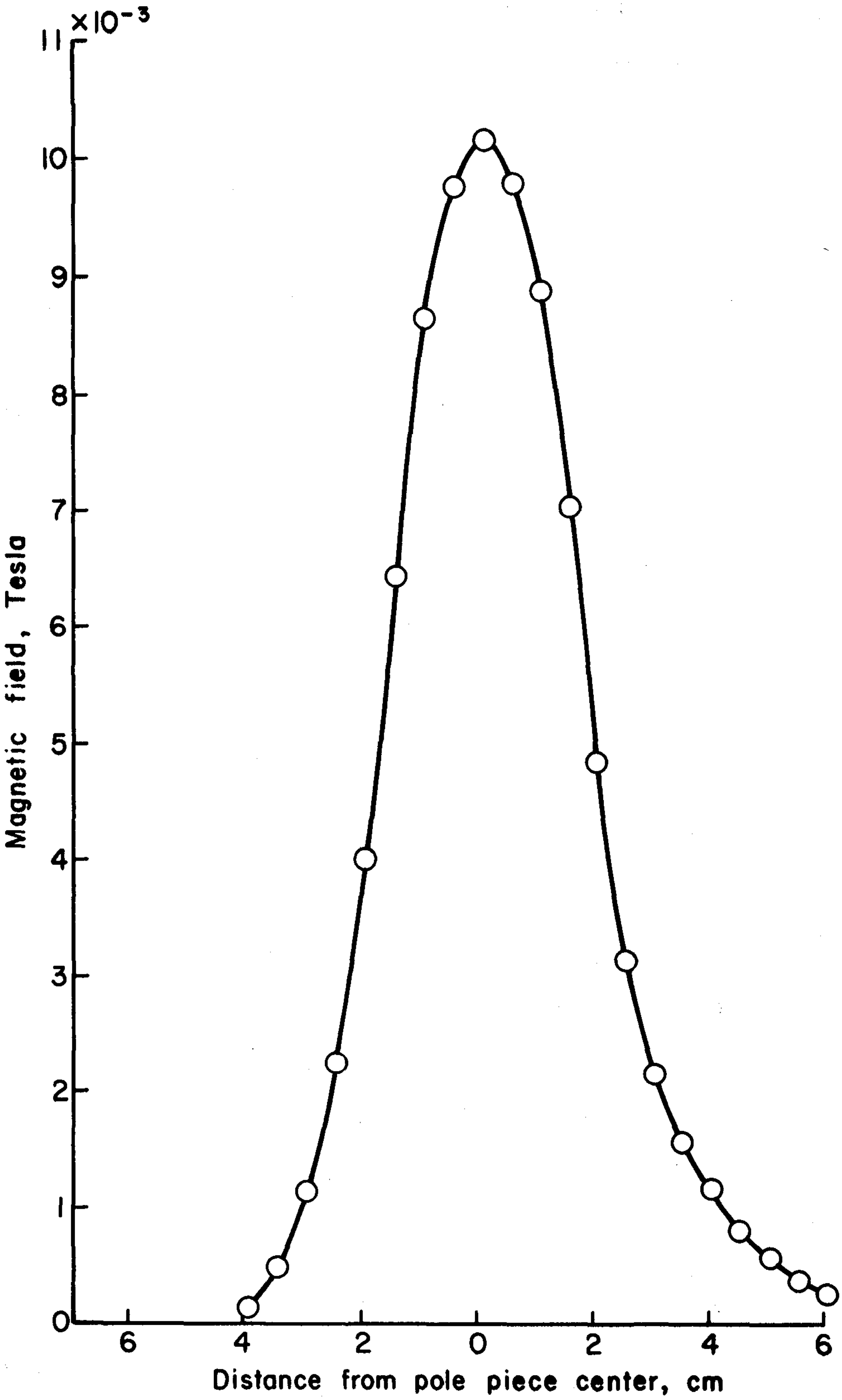

Fig. 2-7. Magnetic field distribution for a middle anode location and the second magnetic field configuration.

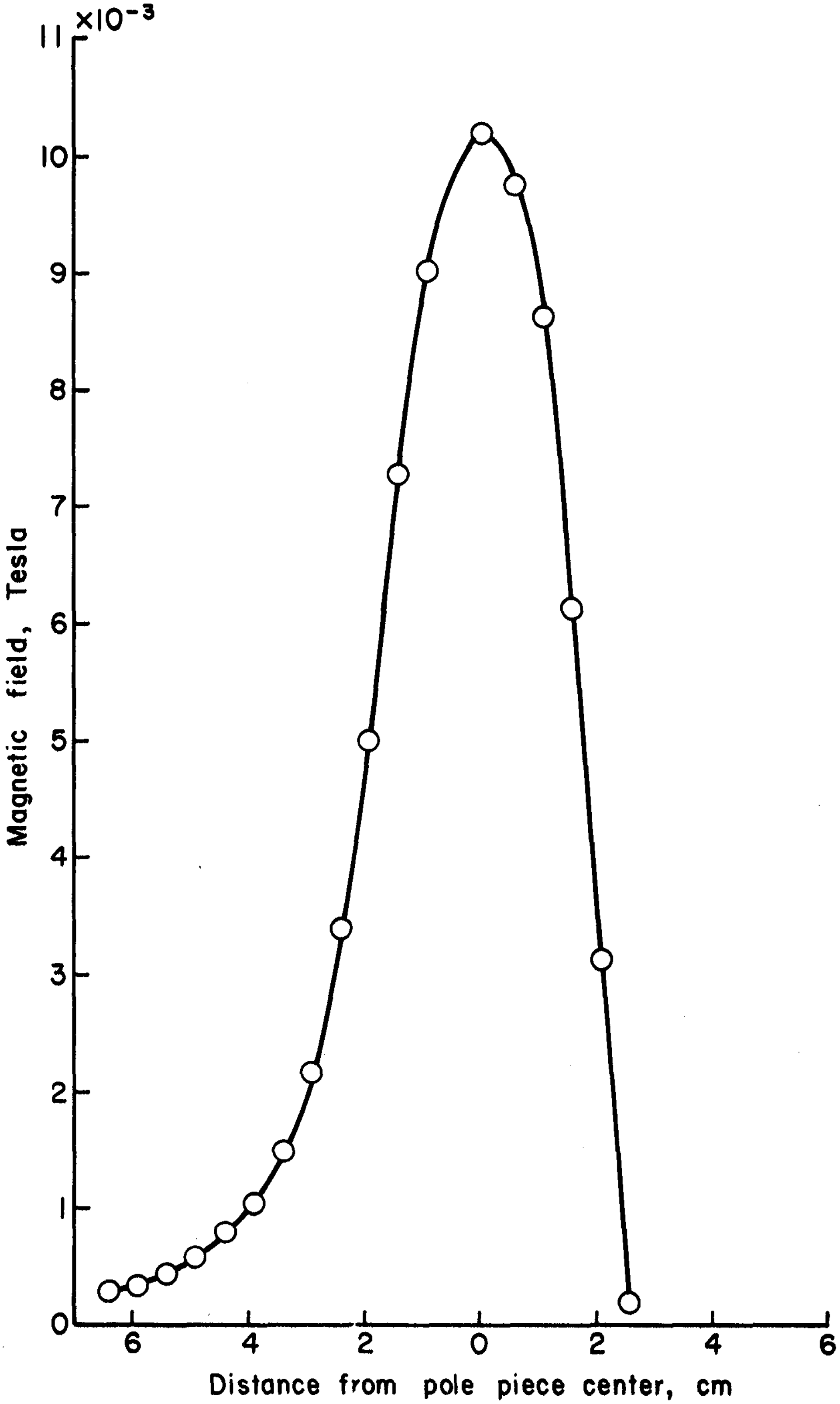

Fig. 2-8. Magnetic field distribution for a side-corner anode location and the second magnetic field configuration.

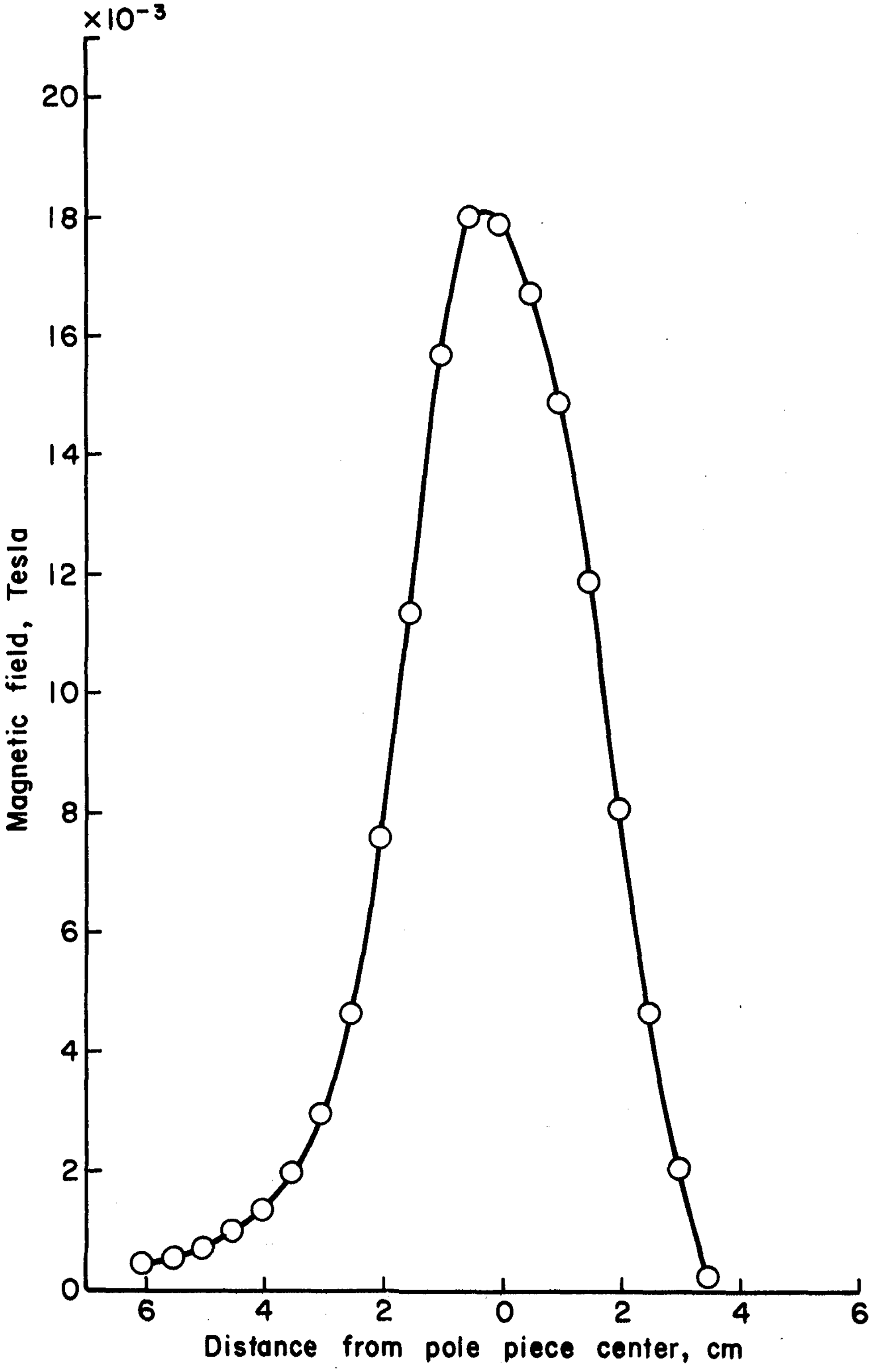

Fig. 2-9. Magnetic field distribution for a back corner anode location and the second magnetic field configuration.

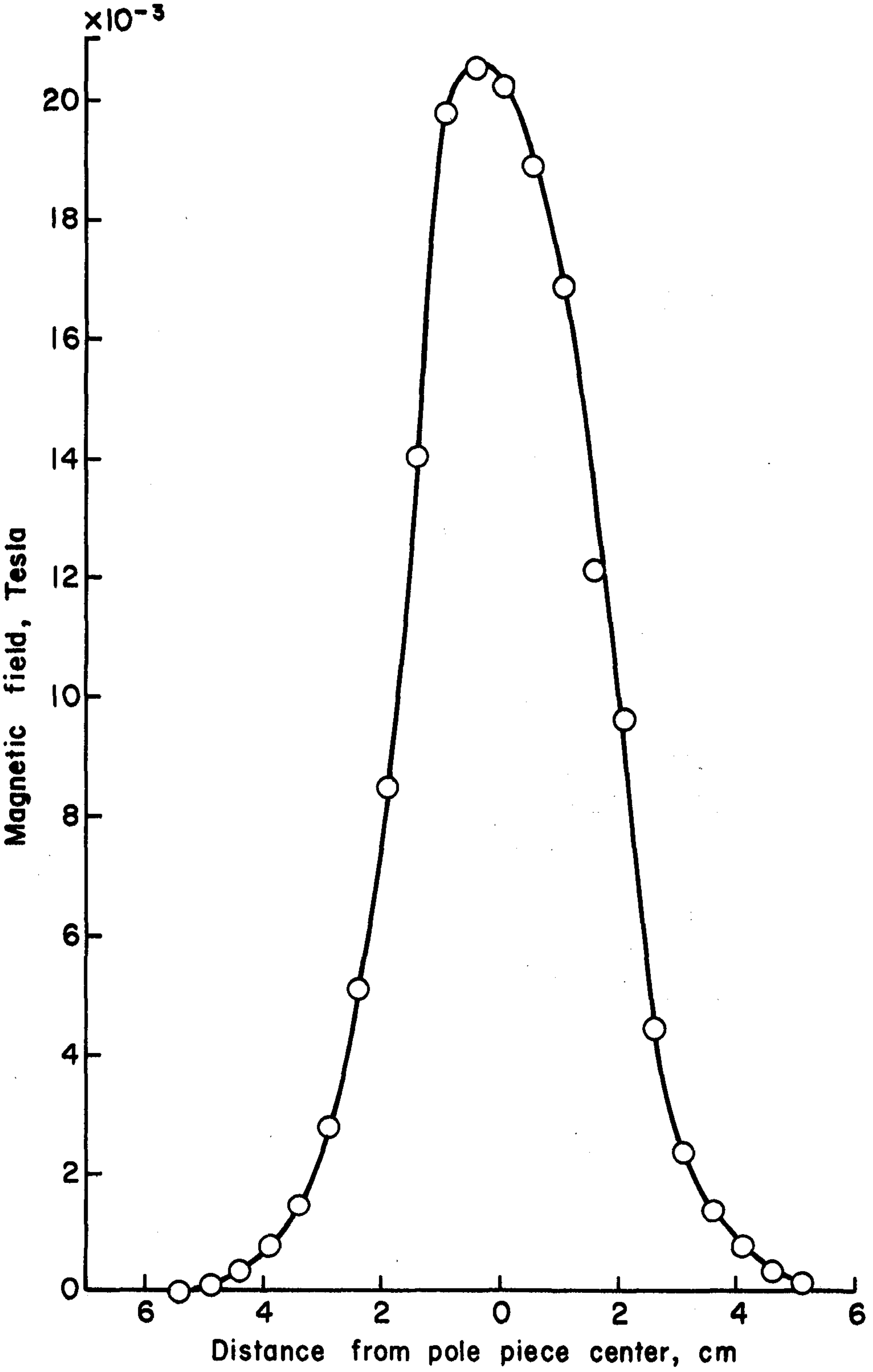

Fig. 2-10. Magnetic field distribution for a back center anode location and the second magnetic field configuration.

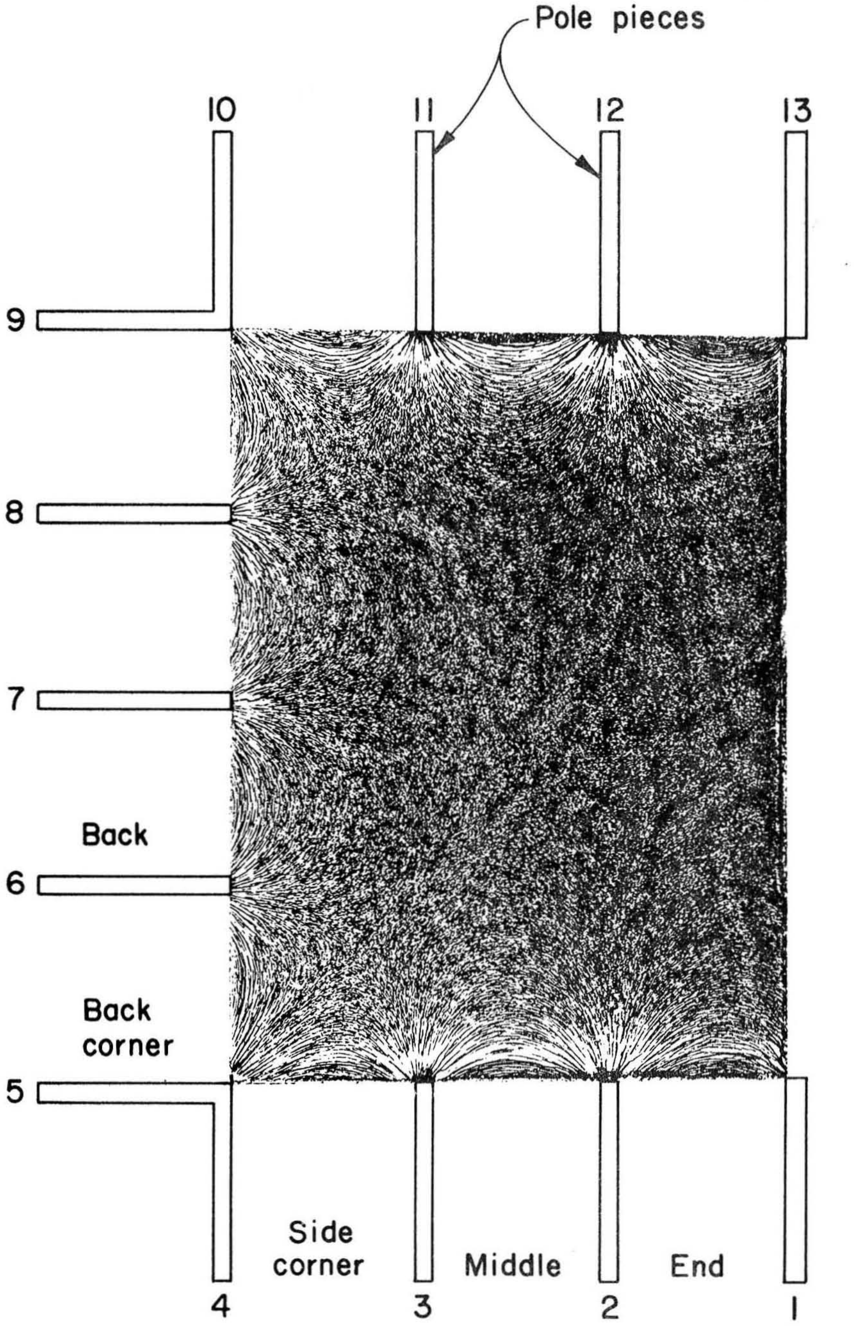

Fig. 2-11. Ferromagnetic powder map of the discharge chamber for the first magnetic field configuration.

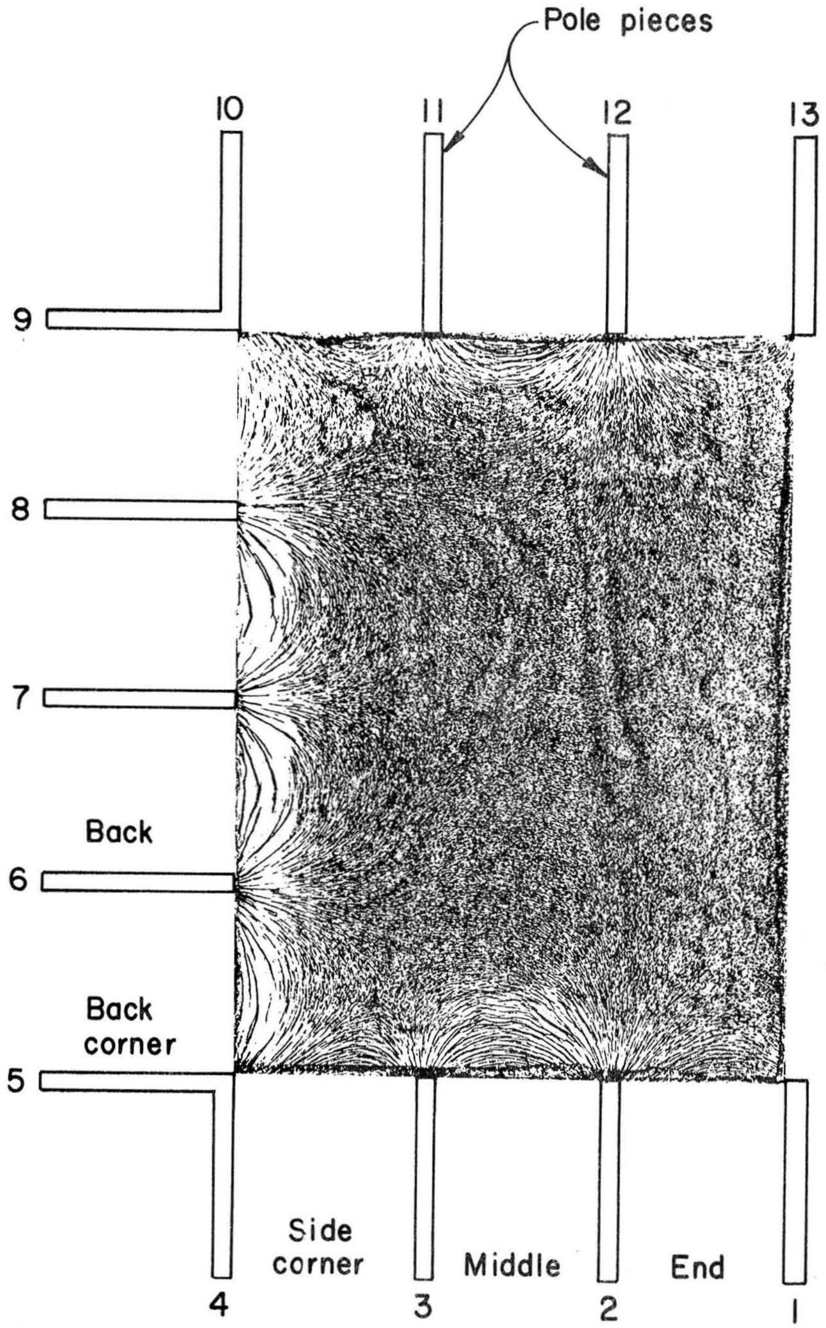

Fig. 2-12. Ferromagnetic powder map of the discharge chamber for the second magnetic field configuration.

With the doubled magnetic field at the back wall of the discharge chamber, it was found necessary to move the cathode farther into the discharge chamber. The magnetic field distribution of Fig. 2-10 indicated that the field strength was essentially zero at 4.0 cm from the edges of the back pole pieces (5.3 cm from the back pole-piece centers). The cathode was put at that location.

Plasma probe. The plasma probe consisted of a Ta wire, 0.74 mm in diameter, and 3-4 mm long. Probe voltages were referenced to the biased anodes. Some measurements were initially made along the long dimension of the discharge plasma. After verifying plasma uniformity, measurements were restricted to a location at the center of the discharge chamber, between the cathode and screen grid. The narrow anodes were used for these measurements.

Procedure

Bias configurations. The thruster was operated in four different bias configurations. Except for changes associated with these bias configurations, the operating conditions were: discharge (V_D, I_D) 40 V, 1 A; screen, 460 V; accelerator (V_a), -500 V; decelerator (V_d), 0 V; beam (V_b, I_b), 500 V, 100 mA; accelerator impingement, 7 mA; neutralizer heater, 25 V (ac), 9.0 A; main cathode heater, 20 V (dc), 25 A; Ar flow ($\dot{m}$), 472 mA-equiv; bell-jar pressure (P), 4×10^{-4} Torr.

The first bias configuration used is indicated in Fig. 2-13 (a). The side anodes were held at +40 V relative to the discharge chamber body and the center connection of the cathode, while the back anodes were biased more positive than the side anodes. Note that the main cathode was heated with direct current to minimize noise. However, the discharge supply was attached to a center electrode in the

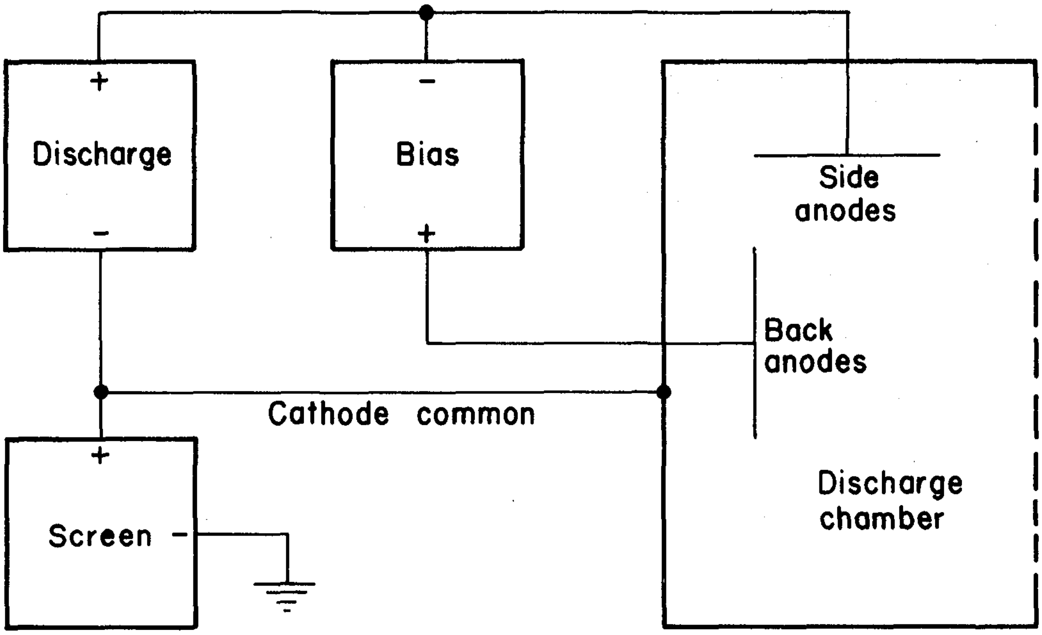

(a) First bias configuration

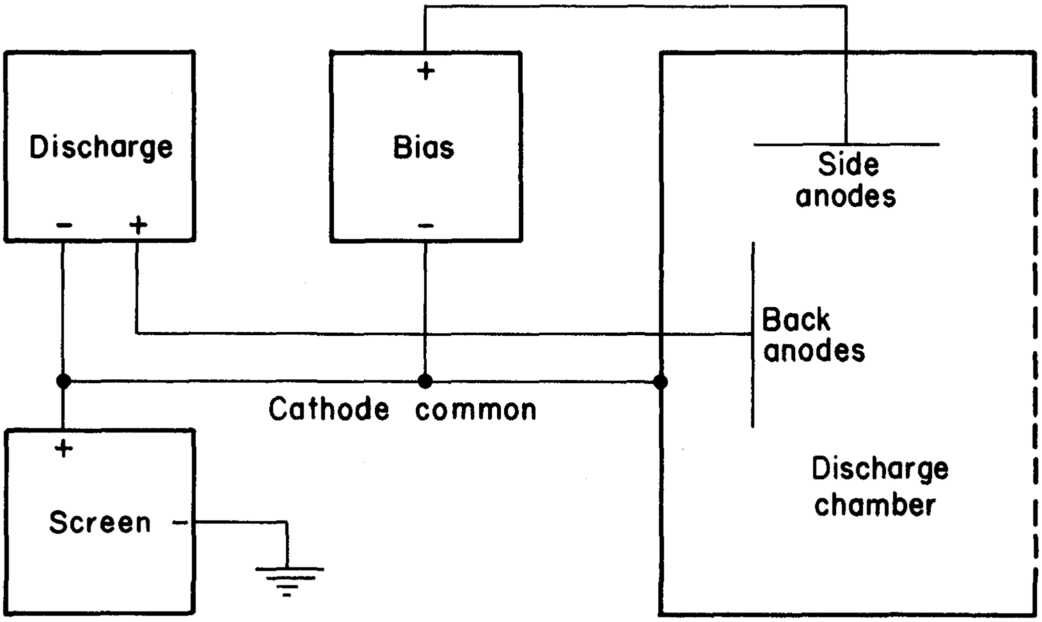

(b) Second bias configuration

Fig. 2-13. Schematic diagrams for bias configurations.

cathode, resulting in a cathode voltage distribution analogous to an alternating-current supply with a center tap.

The second bias configuration, indicated in Fig. 2-13 (b), was similar to the first, except that the back anodes were maintained at +40 V relative to the body and cathode, while the side anodes were biased negative as much as -12 V relative to the back anodes.

The third configuration, Fig. 2-14 (a), differed from the first only in that the discharge-chamber body and screen were not connected, hence "floated". (The side anodes were again maintained at +40 V relative to the cathode, while the back anodes were biased positive up to +20 V relative to the side anodes.)

In the last bias configuration investigated, Fig. 2-14 (b), the discharge chamber body and all the pole pieces were biased from -20 V to +12 V relative to the anodes, which were maintained at +40 V relative to the cathode and screen. Inasmuch as the ends of the discharge chamber had no anodes or pole pieces, sheets of insulation were used at these locations to avoid excessive loss of high-energy electrons.

Discharge losses. The discharge losses were, of course, used to indicate the degree of ion containment achieved. These discharge losses were calculated using the following equations:

For the first and third bias configurations, Figs. 2-13 (a) and 2-14 (a), the discharge losses were calculated from

$$\mathrm{eV/ion} = [V_D(I_D-I_b) + V_{bias}(I_{bias}-I_b)]/I_b; \qquad (2\text{-}2)$$

For the second configuration, Fig. 2-13 (b), the discharge losses were calculated from

$$\mathrm{eV/ion} = [V_D(I_D-I_b) + V_{bias}I_{bias}]/I_b \; ; \qquad (2\text{-}3)$$

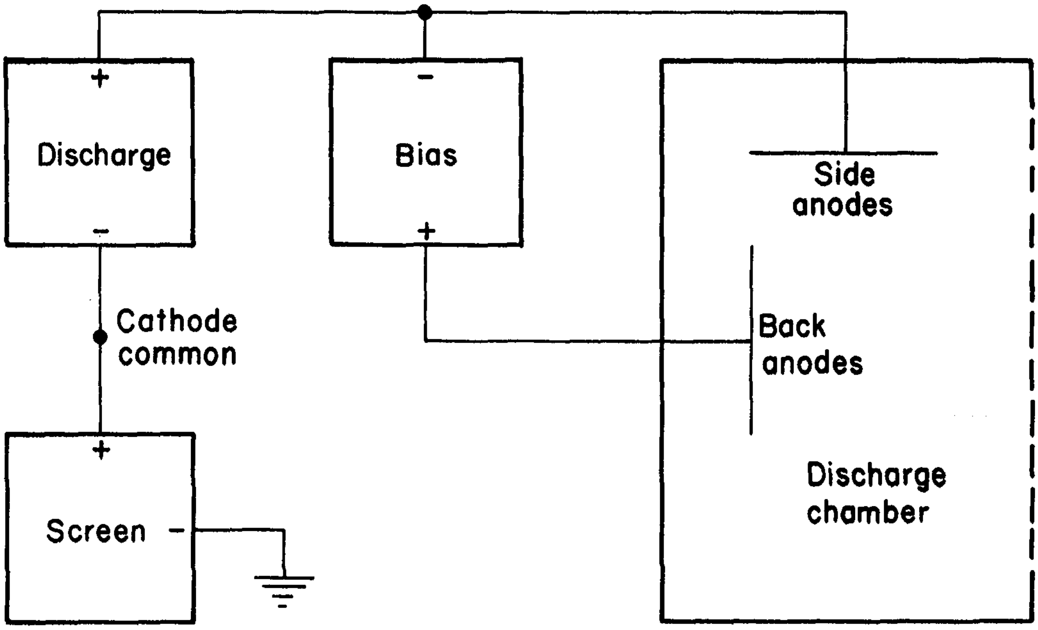

(a) Third bias configuration

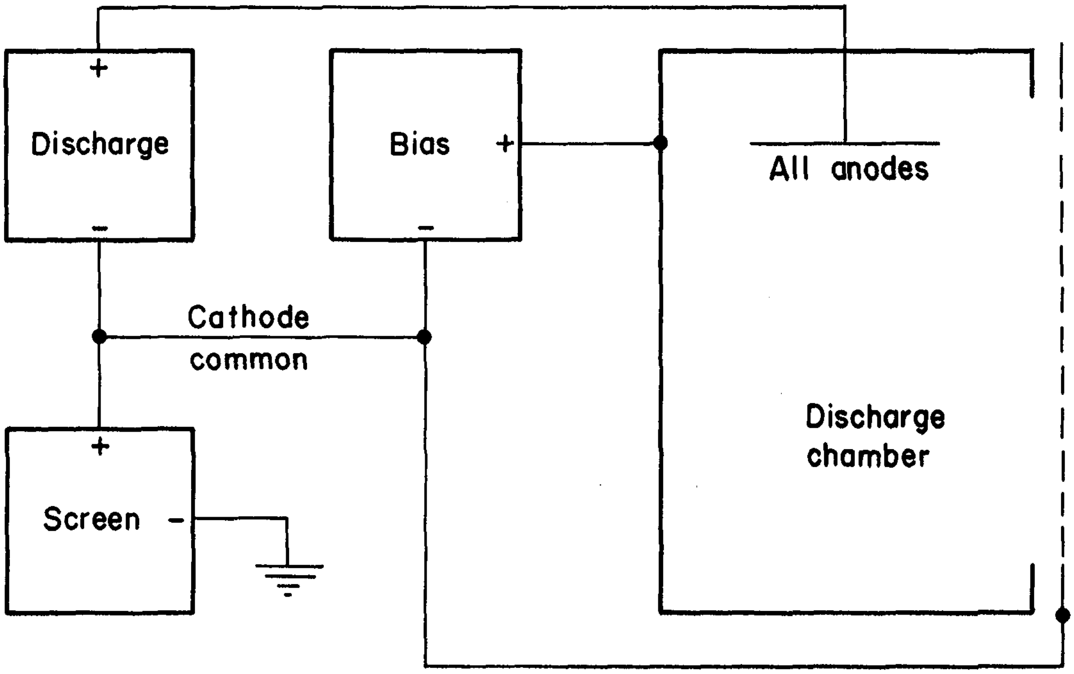

(b) Fourth bias configuration

Fig. 2-14. Schematic diagrams for bias configurations.

For the fourth and last configuration, Fig. 2-14 (b), the discharge losses were calculated from Eq. (2-3) when $V_D > V_{bias}$ and from

$$eV/ion = [V_D I_D + V_{bias}(I_{bias} - I_b)]/I_b \tag{2-4}$$

when $V_{bias} > V_D$; where I_D and V_D are the discharge current and voltage, I_{bias} and V_{bias} are the bias current and voltage, and I_b is the beam current.

In each case the beam current, I_b, was subtracted from the most positive supply. Ignoring the bias supplies in Figs. 2-13 and 2-14 for the moment, the ions originate at plasma potential. Thus any positive potential above screen potential, up to plasma potential, appears as kinetic energy in the beam ions. Because plasma potential is usually within a few volts of anode potential, it is customary with circuit diagrams similar to those in Figs. 2-13 and 2-14 to assume that only $V_D(I_D - I_b)$ is the power that contributes to the ion production. (Note that this calculation would be different if the positive high-voltage supply were connected to the anodes instead of the cathode/screen.) In a generalization of this approach with a bias supply, the beam current has been subtracted from the most positive electrodes in the discharge. The error in this approach is that the discharge power is underestimated by an amount $(V_+ - V_p)I_b$, where V_+ is the most positive electrode potential and V_p is the plasma potential. This magnitude of error did not significantly alter the results presented herein.

Calculation of plasma properties. The plasma properties in the discharge chamber were analyzed using the two-group electron model, low-energy Maxwellian background plus monoenergetic primaries.[7]

Some of the probe traces obtained under bias conditions did not show a clearly defined two-group distribution. Still, the plasma potential was felt to be sufficiently accurate to indicate plasma potential trends relative to the anode potential. Specifically, the results presented herein would be valid if the plasma potential were in error by several volts, which is larger than can be justified by the departure from the assumed two-group model.

Results and Discussion

Plasma uniformity. Plasma properties are shown in Figs. 2-15 through 2-19 as a function of distance in the long dimension of the discharge chamber. Narrow anodes were used in these plasma-property tests. In each case the properties are essentially constant within the chamber, except for end regions where the end wall of the discharge chamber was approached. The plasma potential had a mean value about 6 V positive relative to the anodes, the mean Maxwellian electron temperature was about 9 eV, while the primary electron energy averaged 40 eV. The mean Maxwellian electron density was about 6.5×10^{15} m^{-3}, while that of the primary electrons was about 4×10^{14} m^{-3}. Note that the discharge in these earlier tests was 50 V instead of the otherwise standard 40 V.

The uniformity of the plasma properties indicated in Figs. 2-15 through 2-19 was the justification for the use of single point plasma properties (at the center of the discharge chamber) in all subsequent tests.

Standard magnetic field. Bias tests were conducted first with the original magnetic field. Each of the anodes were adjusted to have a magnetic field integral (between the anode and the center of the discharge chamber) of at least 56×10^{-6} T-m (56 Gauss-cm). This value was chosen for the original design as being sufficient to prevent primary electrons from directly reaching the anodes.

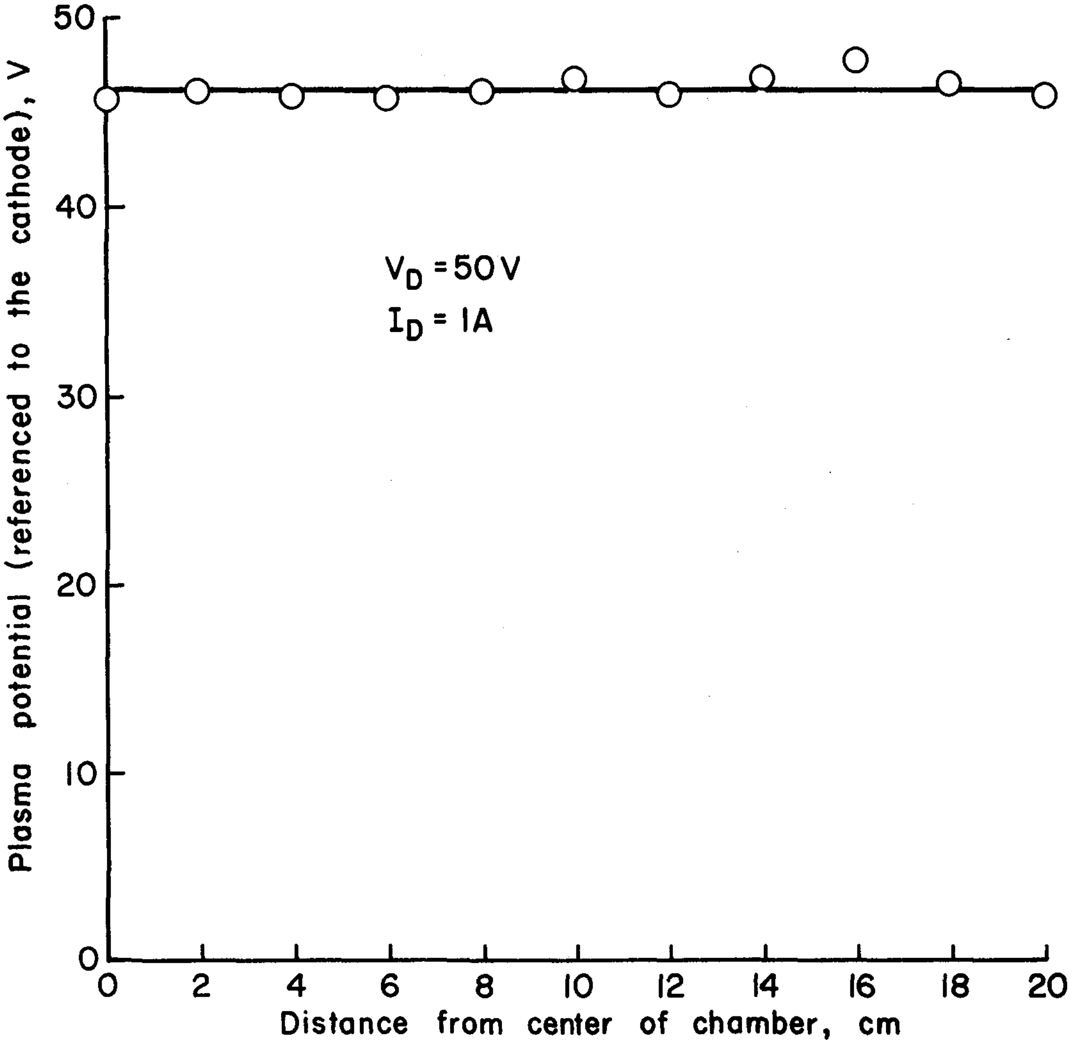

Fig. 2-15. Plasma potential versus distance from the center of the discharge chamber.

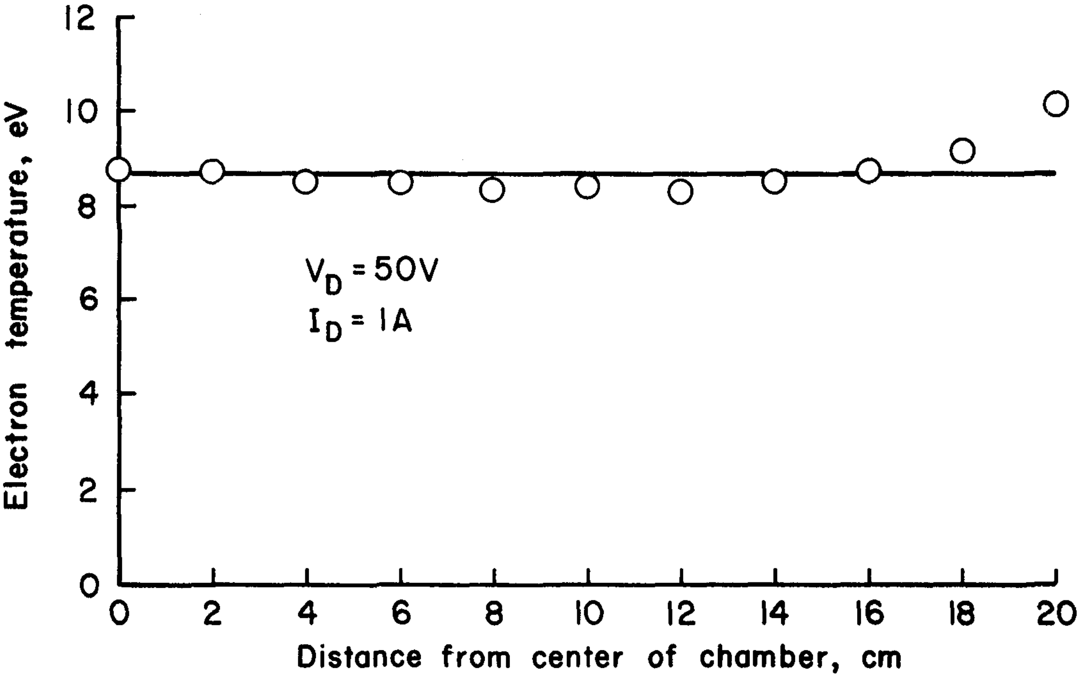

Fig. 2-16. Electron temperature versus distance from the center of the discharge.

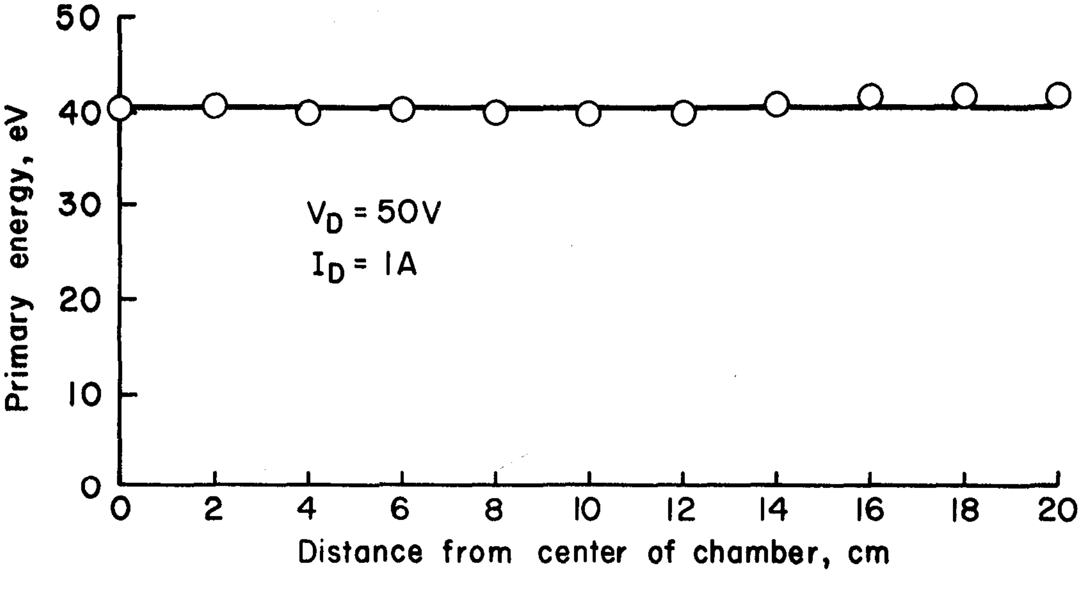

Fig. 2-17. Primary electron energy versus distance from the center of the discharge chamber.

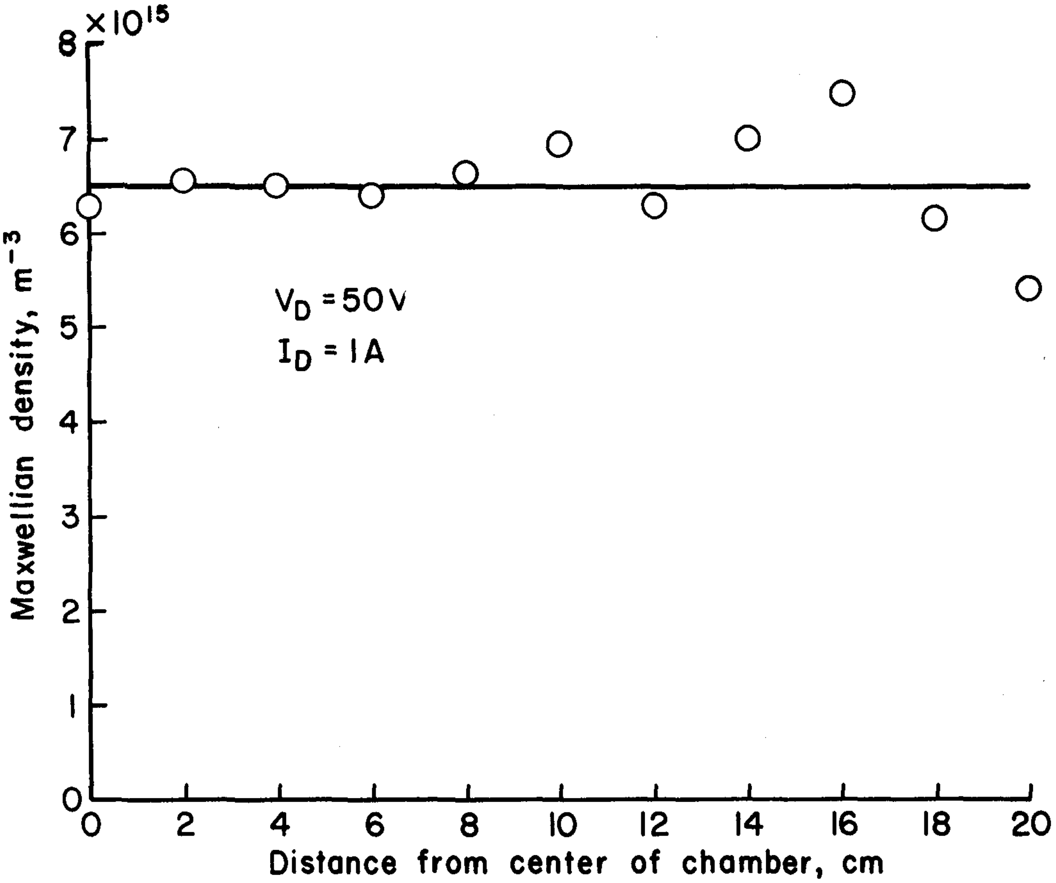

Fig. 2-18. Maxwellian electron density versus distance from the center of the discharge chamber.

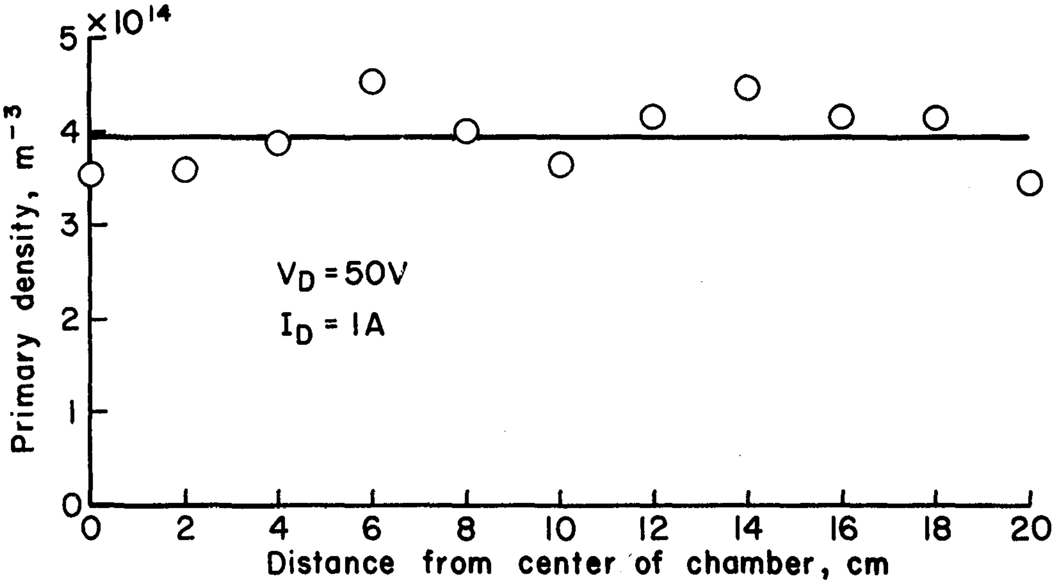

Fig. 2-19. Primary electron density versus distance from the center of the discharge chamber.

The discharge loss curves obtained using the first bias configuration (side anodes at 40 V, back anodes biased more positive) are shown in Figs. 2-20 through 2-22 for the narrow anodes and two settings of the wide anodes (see Fig. 2-1 for narrow and wide anode shapes). The bell-jar pressure was held constant at 4×10^{-4} Torr during these tests. The discharge currents were varied from about 1 to 10 A to obtain the range of beam current shown. The narrow anodes, Fig. 2-20, showed about a 20% increase in discharge loss in going from 0 to +10 V relative bias of the back anodes.

In the hope of providing more anode area to reflect ions, similar bias tests were conducted with the wide anodes, Fig. 2-21. The adverse effect on discharge losses of a given positive bias was nearly doubled with the wide anodes.

Analysis of Langmuir probe data, to be described later, indicated that the wide anodes were less isolated from the discharge plasma than the narrow anodes. To provide an increased magnetic integral, all back anodes were moved 3 mm further away from the discharge. Data taken with this modified anode location are shown in Fig. 2-22. To the extent that comparison is possible, the effect of anode bias is about the same in Figs. 2-20 and 2-22.

The fraction of total discharge current going to the back anodes is shown in Fig. 2-23 as a function of bias voltage for the three different anode configurations of Figs. 2-20 through 2-22. The modified location for the wide anodes is seen to move the current distribution to the back anodes back closer to that for the original narrow anodes.

Plasma properties obtained from the centrally located Langmuir probe are shown in Figs. 2-24 through 2-26. The electron temperatures

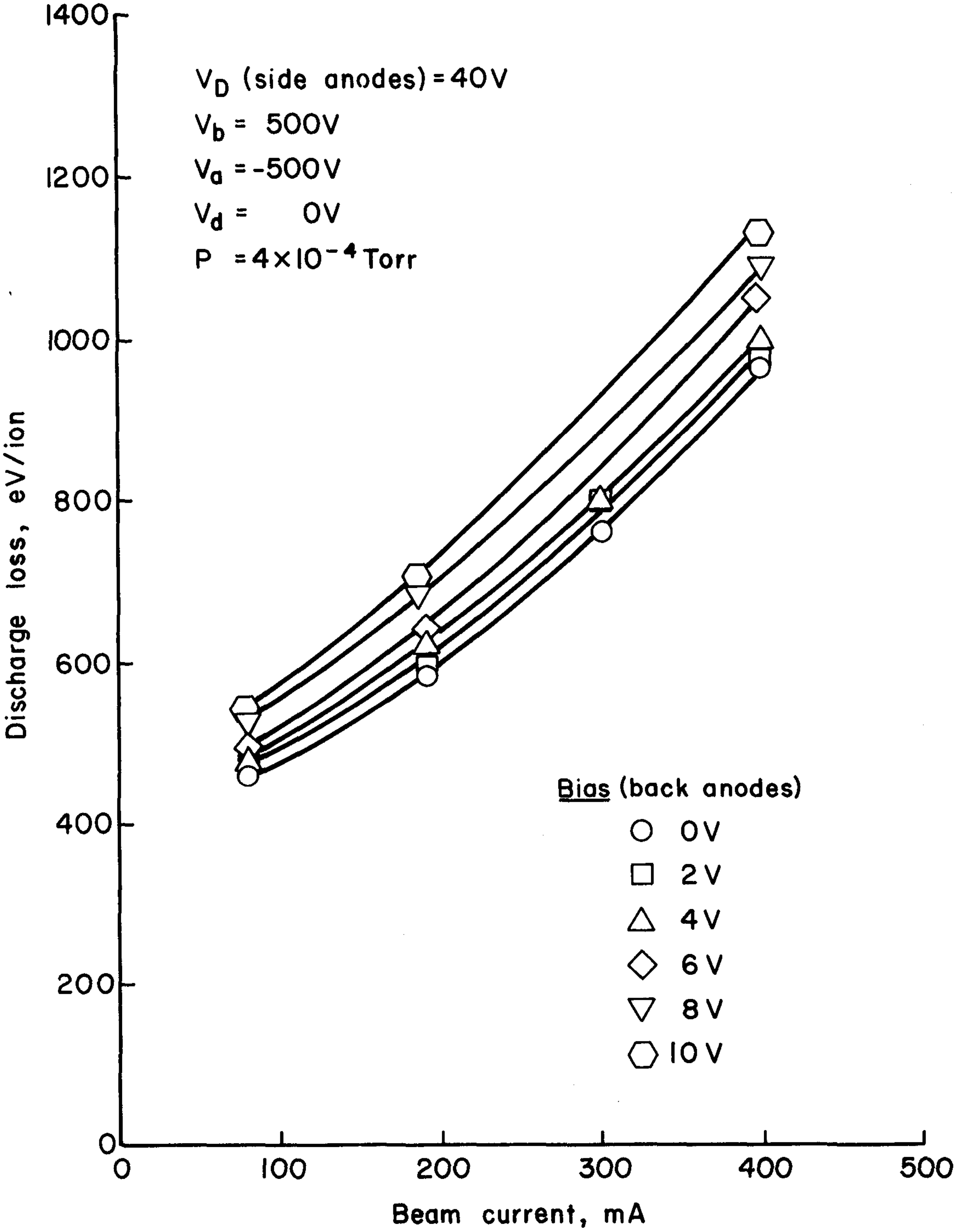

Fig. 2-20. Discharge loss versus beam current for the narrow anodes in the first bias configuration. The first magnetic field configuration and the standard magnetic integral were used.

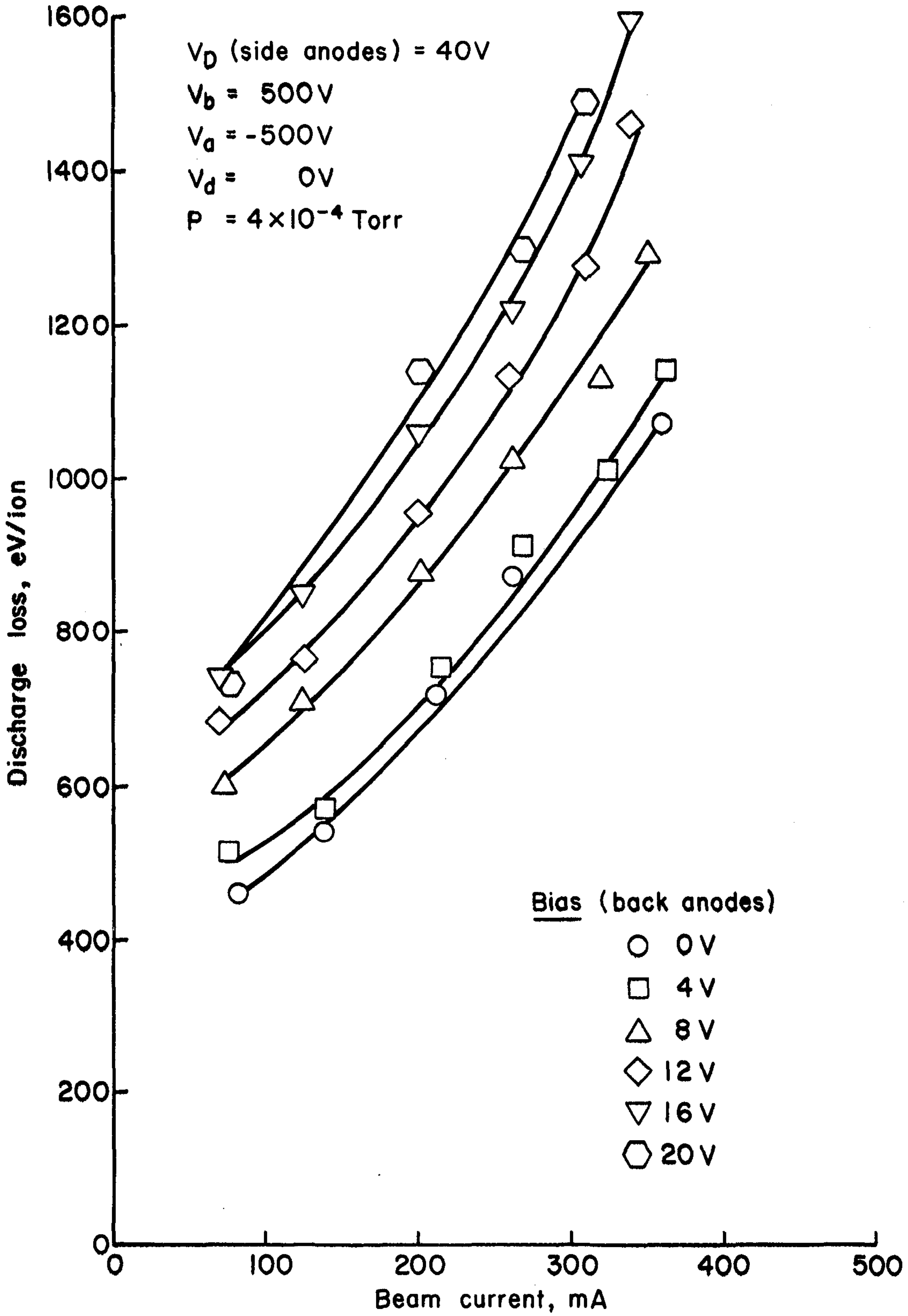

Fig. 2-21. Discharge loss versus beam current for the wide anodes in the first bias configuration. The first magnetic configuration was used with a less than standard magnetic integral.

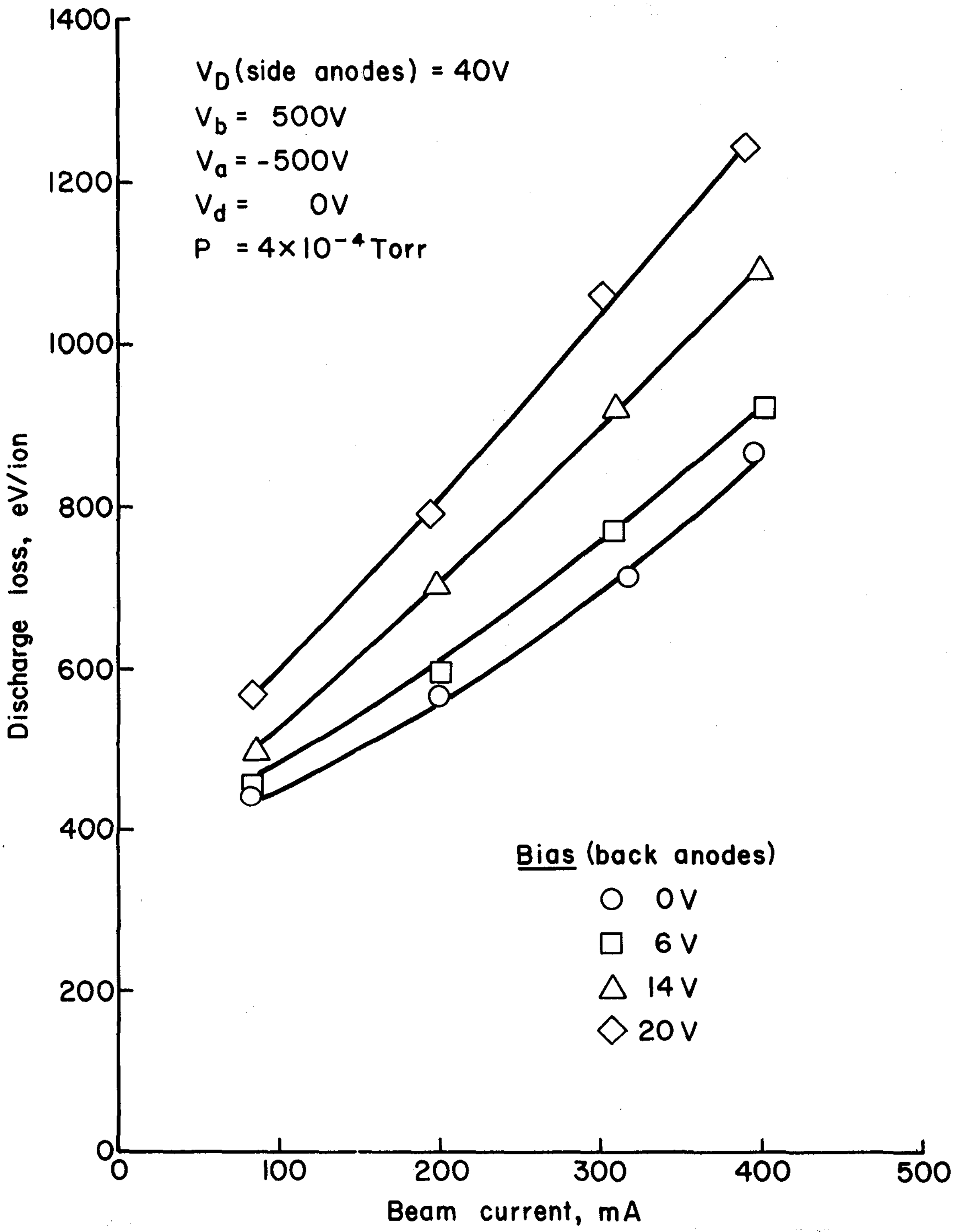

Fig. 2-22. Discharge loss versus beam current for the wide anodes in the first bias configuration. The first magnetic configuration and the standard magnetic integral were used.

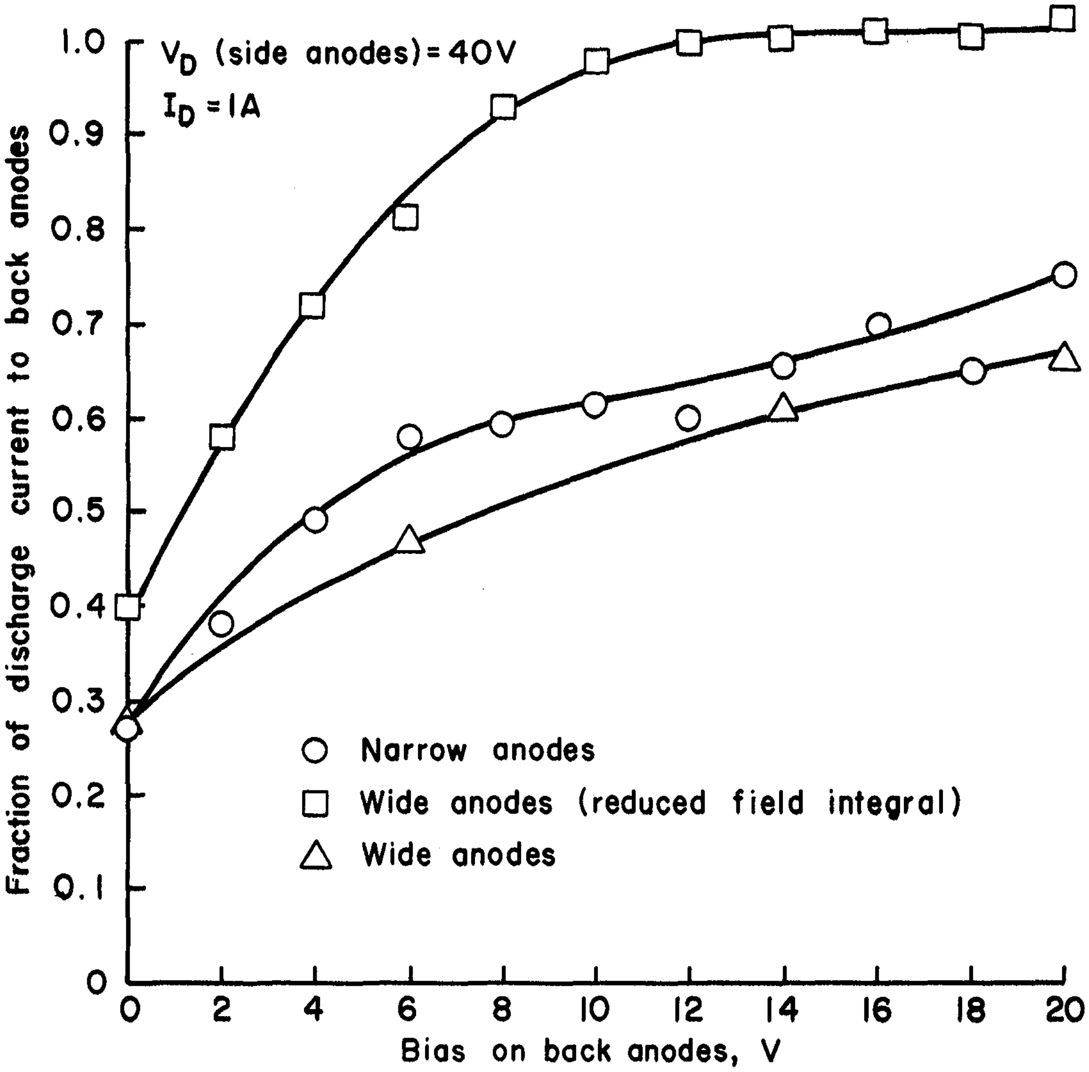

Fig. 2-23. Fraction of the total discharge current to the back anodes versus bias on the back anodes. (Data correspond to Figs. 2-20 through 2-22.)

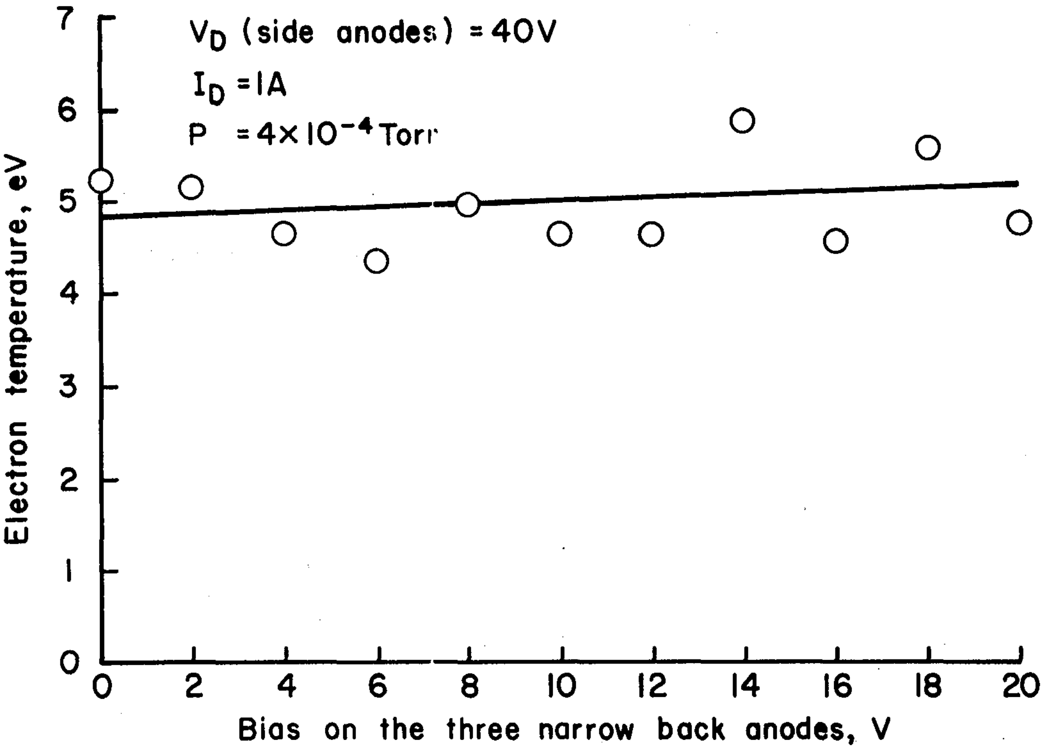

(a) Narrow anodes

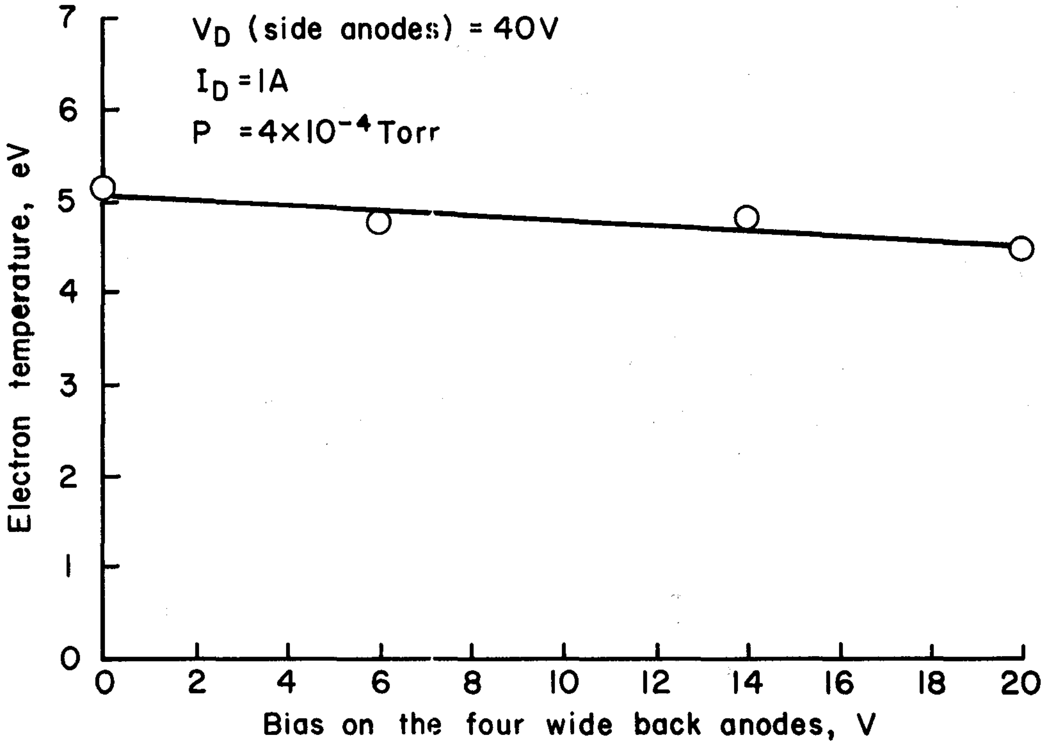

(b) Wide anodes

Fig. 2-24. Electron temperature versus bias. (Data correspond to Figs. 2-20 and 2-22.)

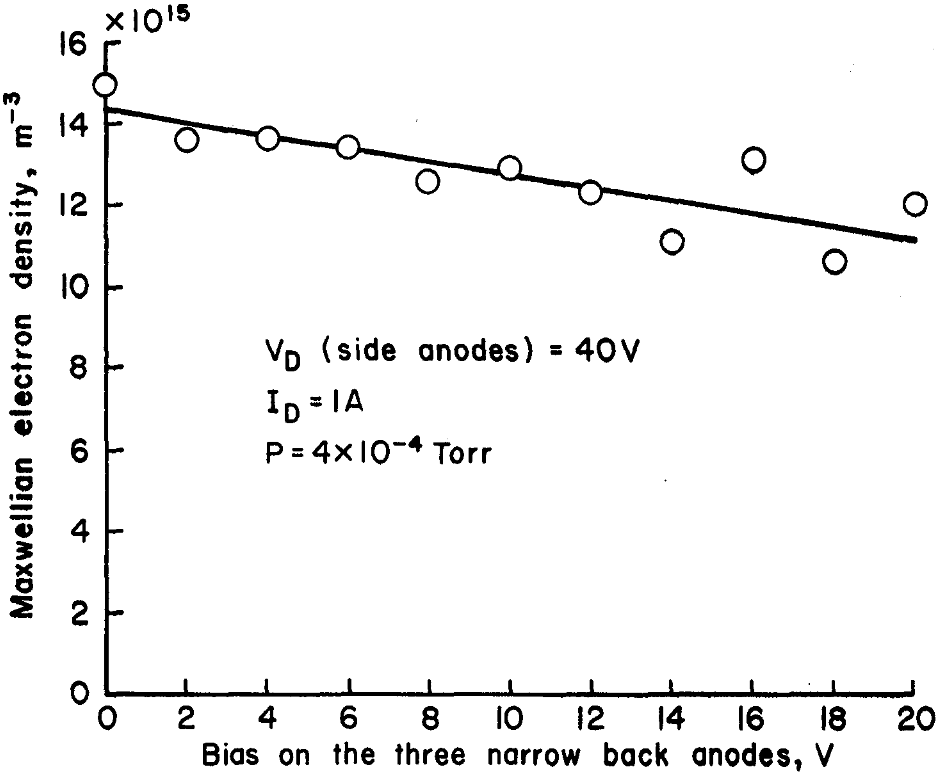

(a) Narrow anodes

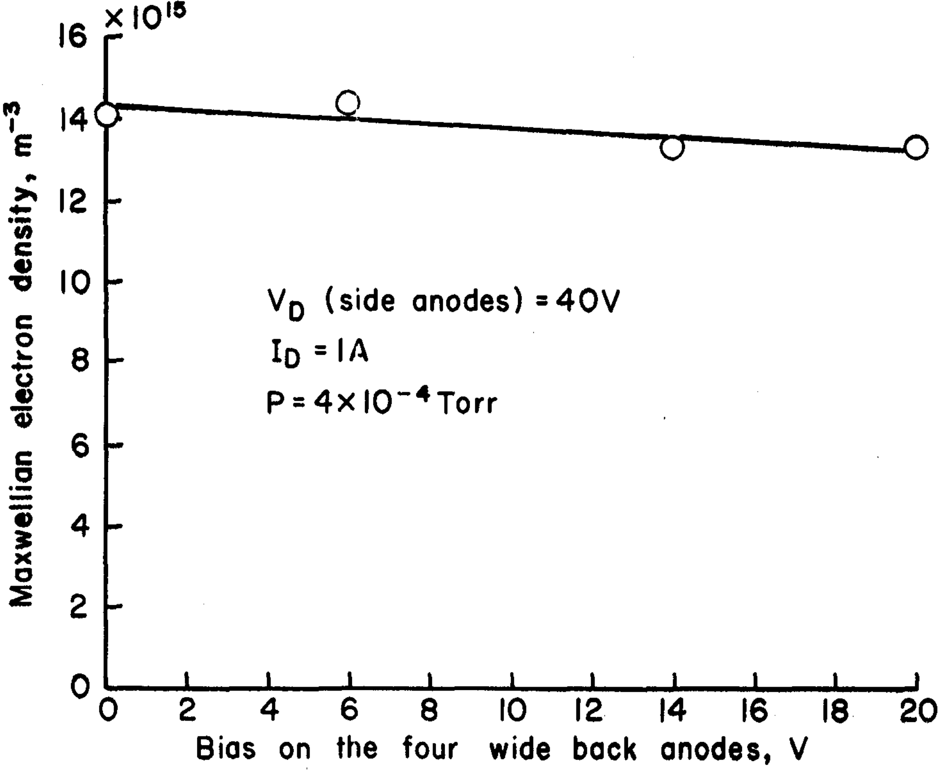

(b) Wide anodes

Fig. 2-25. Maxwellian electron density versus bias. (Data correspond to Figs. 2-20 and 2-22.)

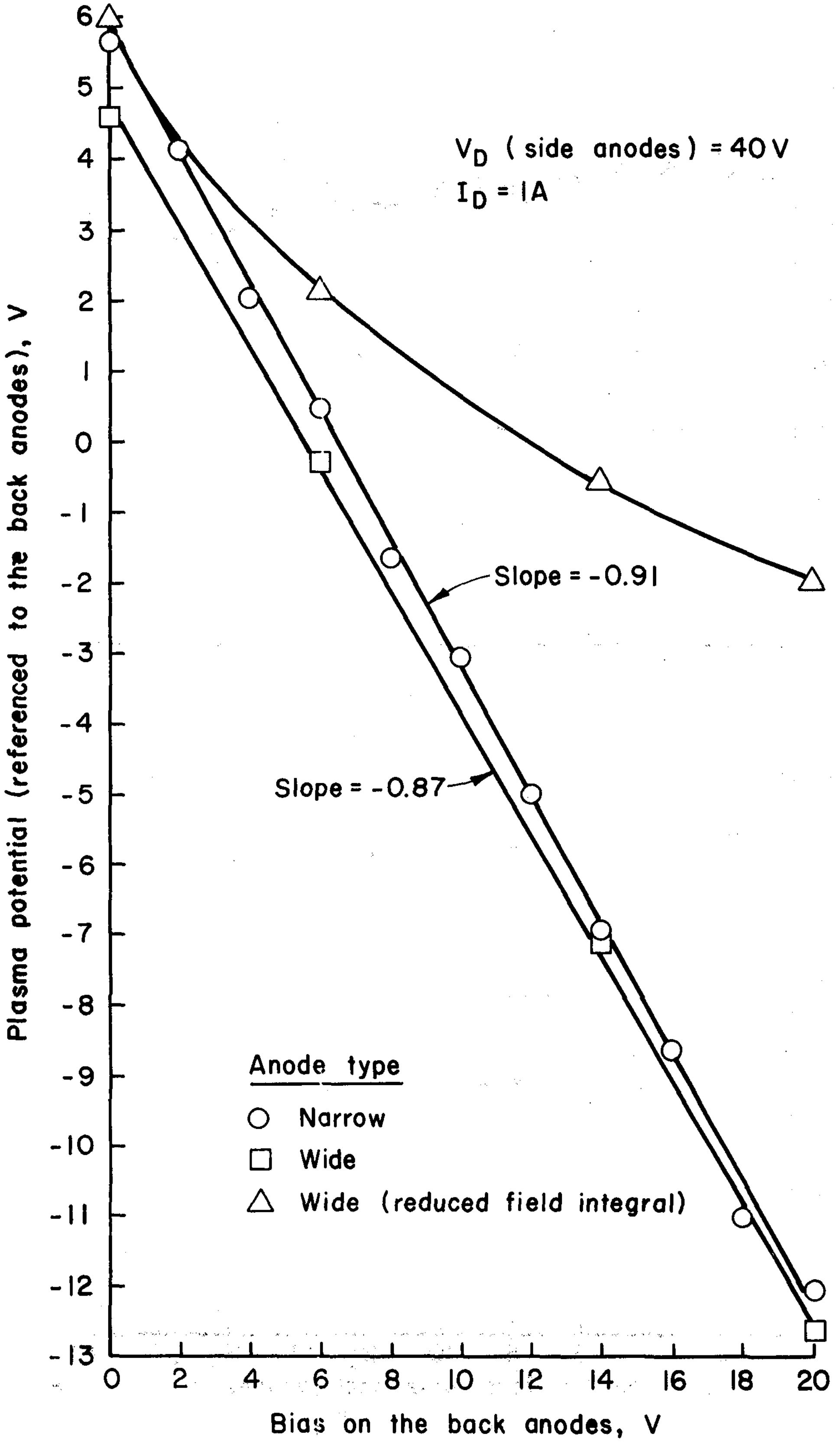

Fig. 2-26. Plasma potential versus back anode bias for three anode configurations. (Data correspond to Figs. 2-20 through 2-22.)

and densities for the narrow anodes and original location of wide anodes, Figs. 2-24 and 2-25, show only moderate effect of increased bias. The most significant effect of bias appears to be on the plasma potential, Fig. 2-26.

For both the original narrow anodes and the wide anodes with modified location, the back anodes were essentially decoupled from the discharge plasma during bias operation. This decoupling was shown by the approximately 0.9 V increase in anode-plasma potential difference for each 1 V increase in positive bias for the anodes. The original location of the wide anodes resulted in much less decoupling, 0.4-0.6 V change for each 1 V of bias change.

As mentioned above, the original narrow anodes had magnetic integrals of at least 56×10^{-6} T-m. The wide anodes in their original locations had, midway between pole pieces, magnetic integrals of 58×10^{-6} T-m for the back corners and 52×10^{-6} T-m for the back center locations. (These locations are defined in Fig. 2-4.) In addition, because of the width of the wide anodes and the effects of warping, the magnetic integrals for edges of the wide anodes may have been considerably less. After recessing the wide anodes by 3 mm, the magnetic integrals for the wide anodes, again midway between pole pieces, were increased to 78×10^{-6} T-m in the back corners and 69×10^{-6} T-m in the back center locations.

Some additional tests with the other bias configurations were also conducted with the standard magnetic field configuration, Figs. 2-27 through 2-30. In Fig. 2-27, the discharge losses are shown for the second bias configuration, with back anodes at +40 V and the side anodes biased negative relative to the back anodes. The wide anodes

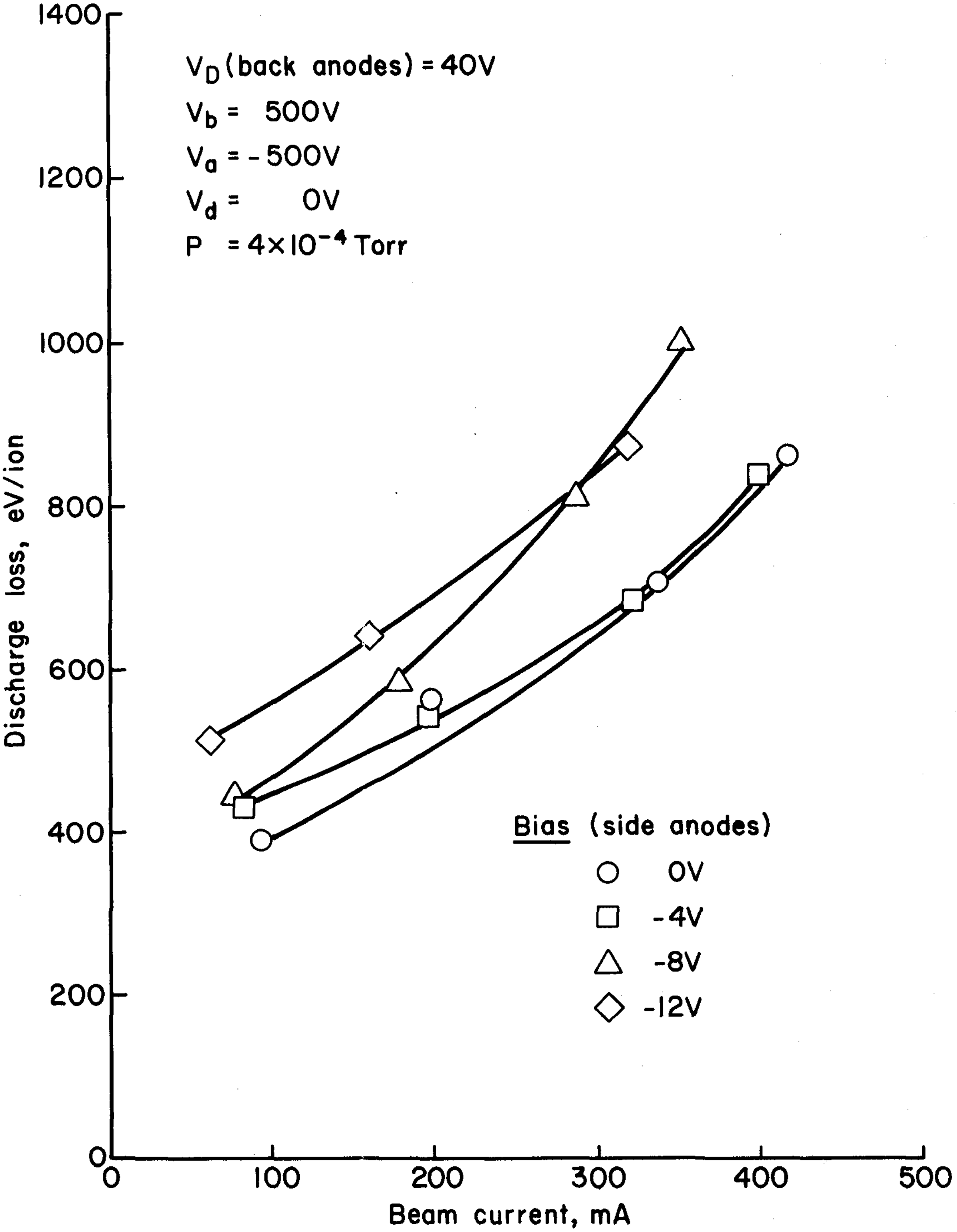

Fig. 2-27. Discharge loss versus beam current for the wide anodes in the second bias configuration. The first magnetic field configuration and the standard magnetic integral were used.

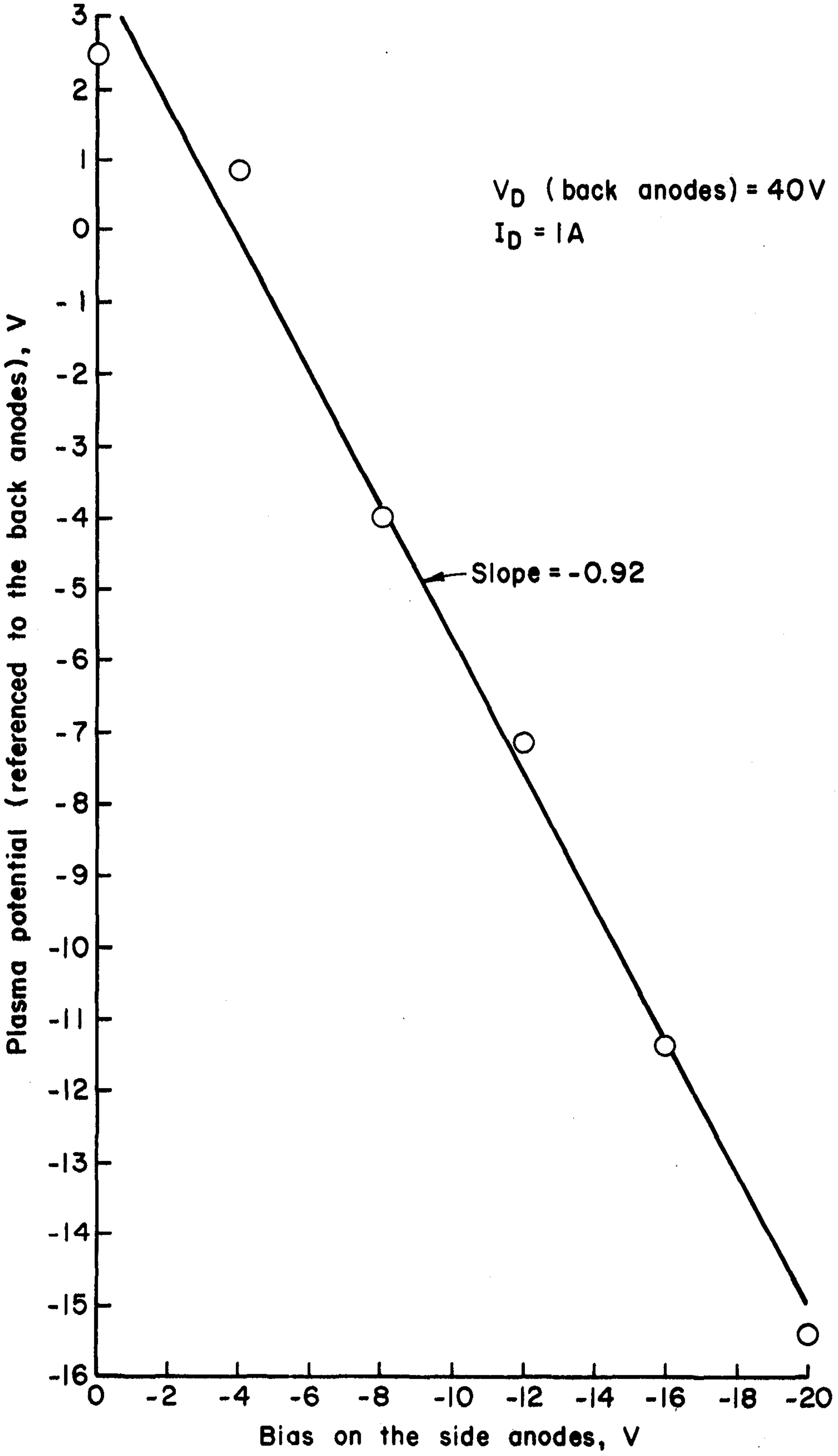

Fig. 2-28. Plasma potential versus side anode bias for the second bias configuration. (Data correspond to Fig. 2-27.)

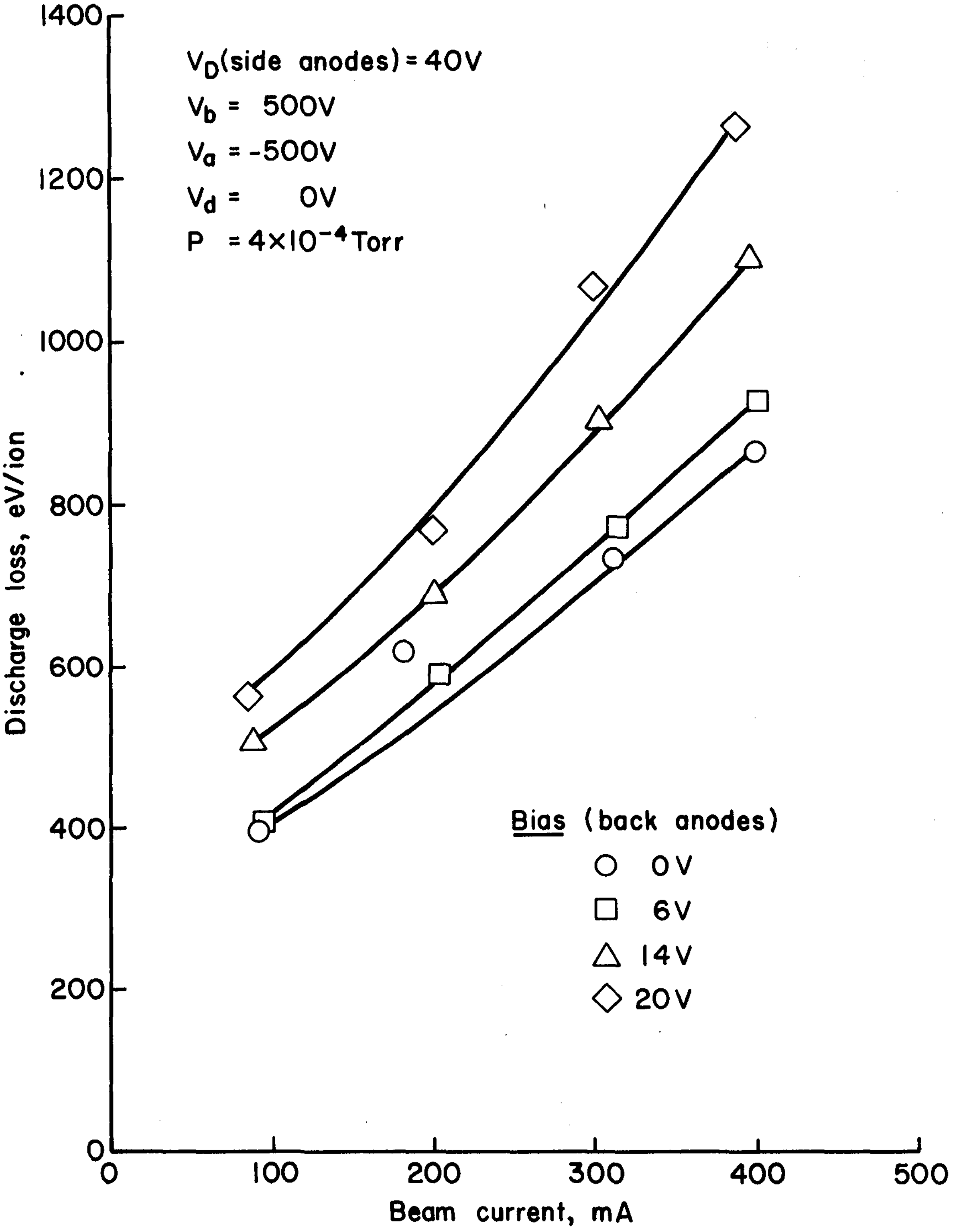

Fig. 2-29. Discharge loss versus beam current for the wide anodes in the third bias configuration. The first magnetic field configuration and the standard magnetic integral were used.

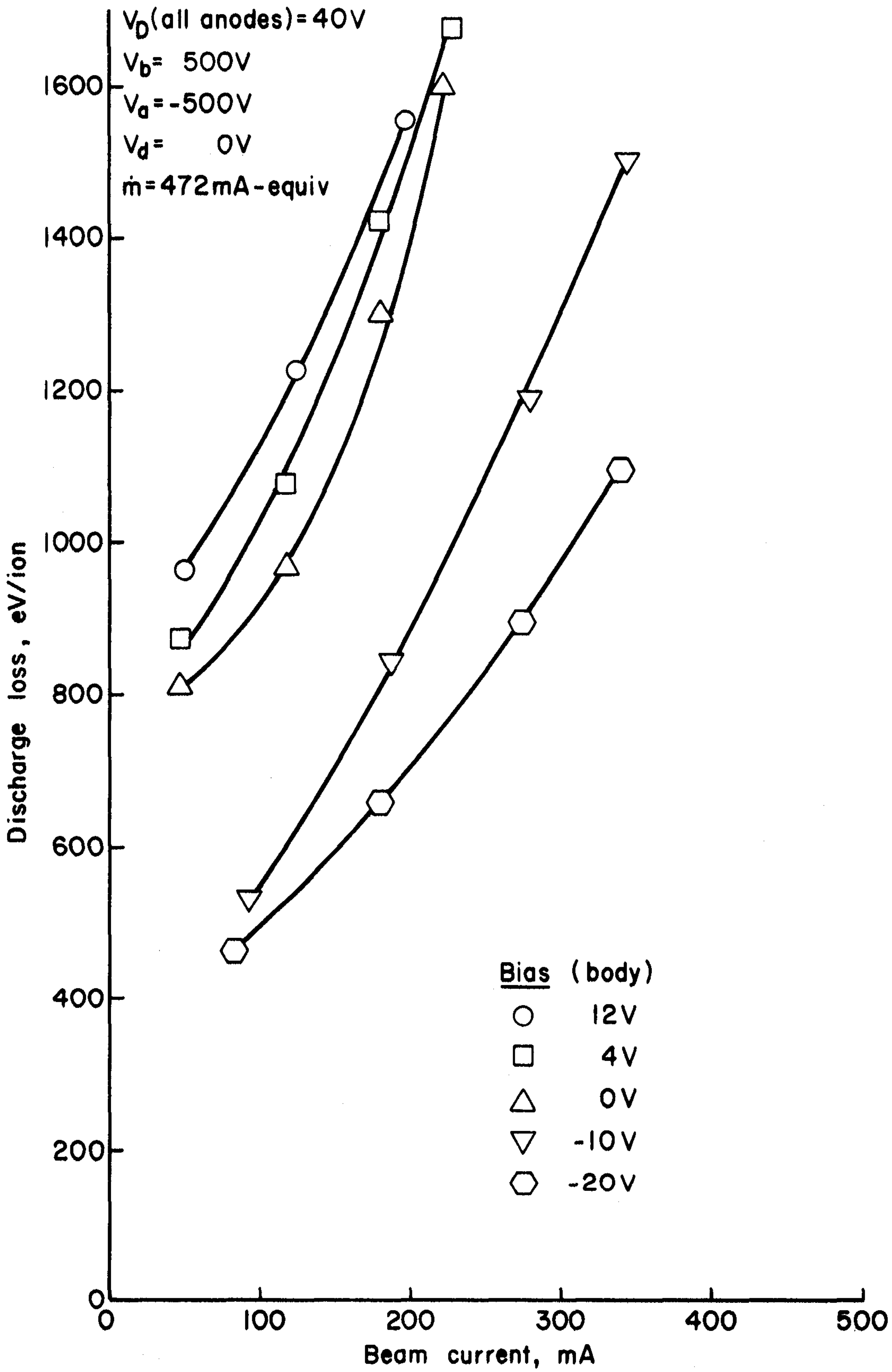

Fig. 2-30. Discharge loss versus beam current for the narrow anodes in the fourth bias configuration. The first magnetic field configuration and the standard magnetic integral were used.

with their modified locations were used here, and some of the results (see -8 V, in particular) appear to be affected by warping of the wide anode surface. Other than these possible effects of warping, the results are similar to those with the same anodes and the first bias configuration. The corresponding plasma potential, Fig. 2-28, also showed the same ~0.9 V change in plasma potential relative to the back anodes for each 1 V change in bias.

The discharge losses for the third bias configuration, with floating discharge-chamber body, are shown in Fig. 2-29. The wide anodes with modified locations were used here, and, again, there is no significant departure from results with the first bias configuration.

Discharge loss data for the fourth bias configuration, with biased pole pieces, are shown in Fig. 2-30. The narrow anodes were used in these tests. All bias operation with this configuration shows higher losses than the standard configuration (Fig. 2-20, with no bias). Part of the difference was due to a change in operating procedure. In the earlier tests, bell-jar pressure was held constant at 4×10^{-4} Torr. It was felt that holding the gas flow to the thruster constant (at 472 mA-equiv) might provide more constant thruster operating conditions. The two operating procedures are approximately equivalent at a 100 mA beam current, but diverge increasingly at higher beam currents.

In Fig. 2-30, the losses rise sharply as the pole pieces reach plasma potential. This sharp rise can be explained by the increased electron current loss associated with the more dense Maxwellian electrons. The loss increases for lower (more negative) biases are smaller, but still no beneficial effect could be found for biasing pole pieces positive of their usual -40 V (relative to anodes) value.

Increased magnetic field. After the magnetic field near the back anodes was doubled, the strip anodes (Figs. 2-2 and 2-3) were tested with the first and fourth bias configurations. The use of the strip anodes was based on the warping problems encountered with the narrow and wide anodes (which were made of thinner sheet metal), together with the lack of any clear evidence that anode width was significant.

For the first test with the increased magnetic field, the back strip anodes were moved far enough into the discharge chamber to reduce their magnetic integrals to about 56×10^{-6} T-m. With these anode field integrals and the fourth bias configuration (biased pole pieces), the data of Fig. 2-31 were obtained.

Again, no benefit of biased operation was found. In comparing the data of Fig. 2-31 to the similar data obtained with the original magnetic configuration, Fig. 2-30, two things are evident. First, the data in Fig. 2-31 are more regular, indicating less effect of warping on performance. Second, the adverse effect of a given bias level was generally decreased with the increased magnetic field.

Because the magnetic integral protecting the anodes was the same in both cases, this difference did not appear to be associated with the anodes. Referring back to Figs. 2-11 and 2-12 for the ferromagnetic powder field maps, it is clear that the increased magnetic field will result in stronger "mirrors" and smaller loss cones for the escaping electrons. The higher magnetic field thus results in less coupling of the discharge plasma with the pole pieces, hence less electron loss to the pole pieces at a given bias.

The strip anodes were also tested in the first bias configuration (back anodes biased positive) with both the original 56×10^{-6} T-m

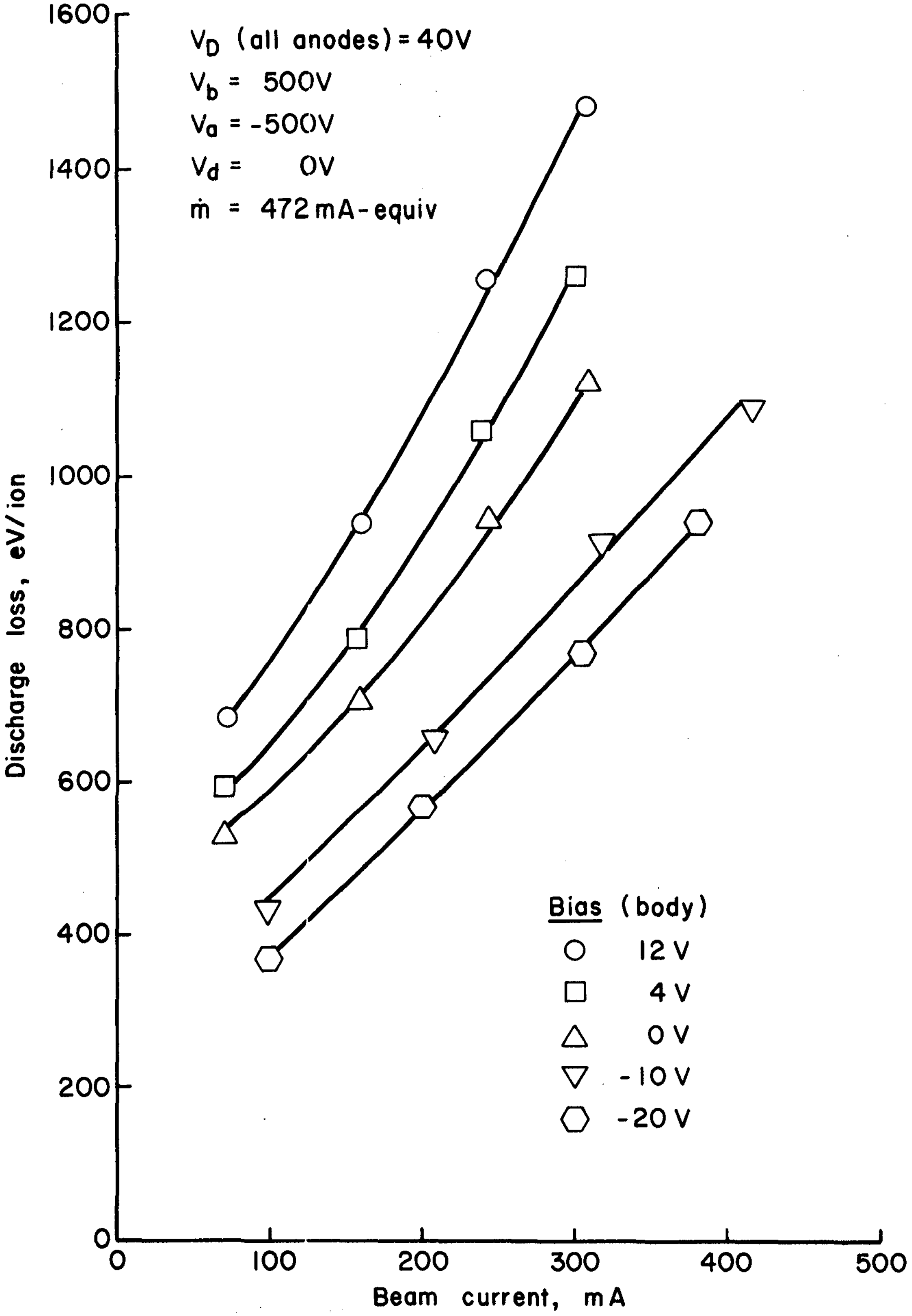

Fig. 2-31. Discharge loss versus beam current for the strip anodes in the fourth bias configuration. The second magnetic configuration and the standard magnetic integral were used. Note that bias voltage here is given relative to anodes.

integral and increased values of 112 × 10^{-6} T-m, or more, for the back anodes. The increased back magnetic field was used for both of these tests, so the integral difference simply corresponded to a displacement of the anodes.

The discharge losses for the 56 × 10^{-6} T-m integral value are shown in Fig. 2-32. Comparing these results with the supposedly similar results with the original magnetic field, Fig. 2-20, the adverse effect of the same bias is slightly greater in Fig. 2-32 for a 100 mA beam, and slightly less near 400 mA. For the same field integral, then, there is no large difference between the added losses due to biasing for the two magnetic fields.

For the increased integral, Fig. 2-33, the adverse effect of back anode bias is sharply reduced. For the same +20 V bias, the higher magnetic integral results in about half the loss increase.

The plasma potentials corresponding to the two field integrals of Figs. 2-32 and 2-33 are shown in Fig. 2-34. Although both configurations are believed to be above the minimum magnetic integral of about 56 × 10^{-6} T-m, found for the original magnetic field, the lower integral was clearly not as isolated from the discharge plasma as the higher value.

There are at least two possible explanations for the results shown in Fig. 2-34. The use of a magnetic integral is based on a nearly constant conduction area.[8] In moving the anodes further out into the discharge chamber to obtain the 56 × 10^{-6} T-m integral with the doubled number of magnets, the average magnetic field line above the anode becomes longer. This means that the mean conduction area (parallel to field lines) becomes more curved, and has a greater magnitude. As one explanation, then, the same magnetic integral with the

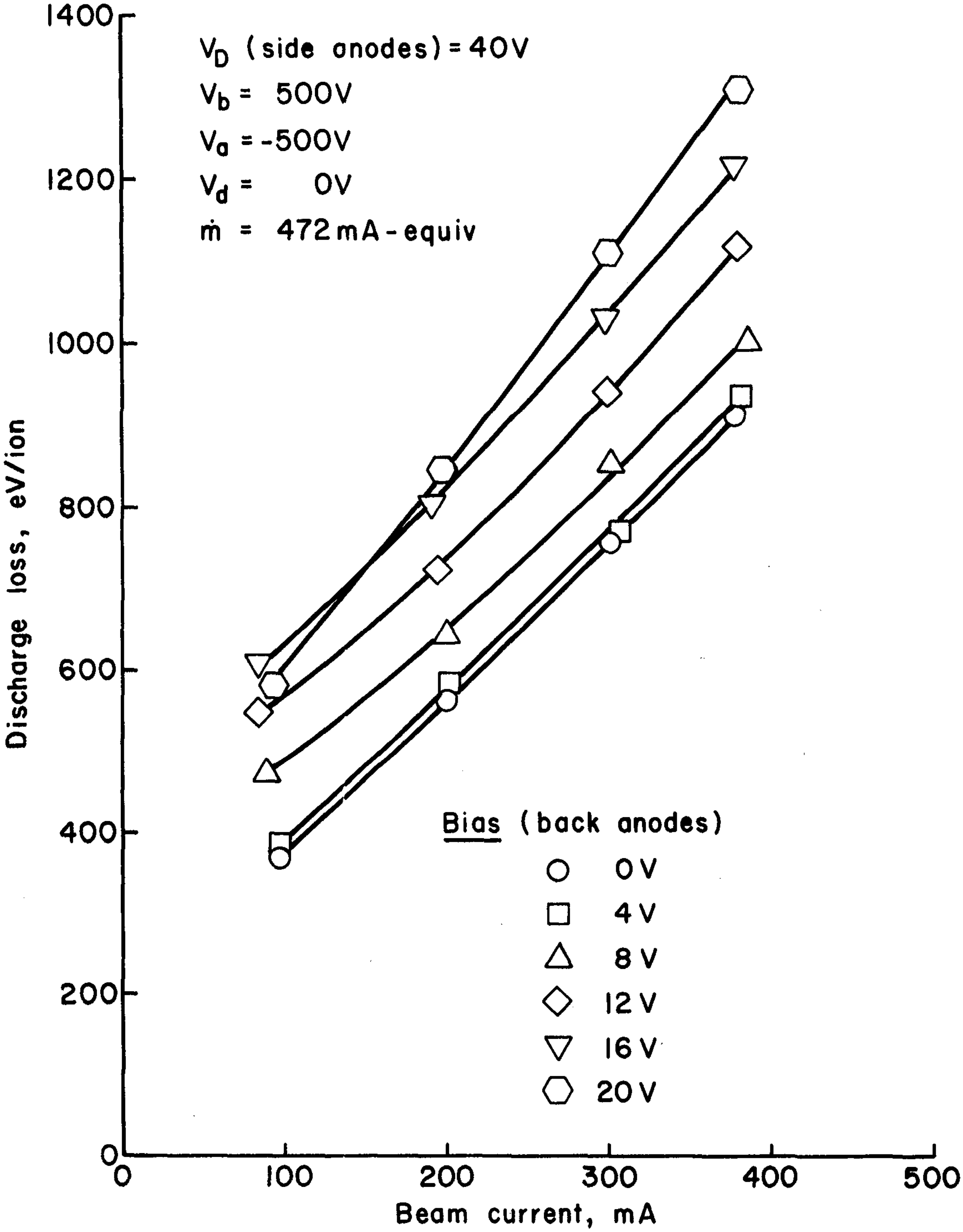

Fig. 2-32. Discharge loss versus beam current for the strip anodes in the first bias configuration. The second magnetic configuration and the standard magnetic integral were used.

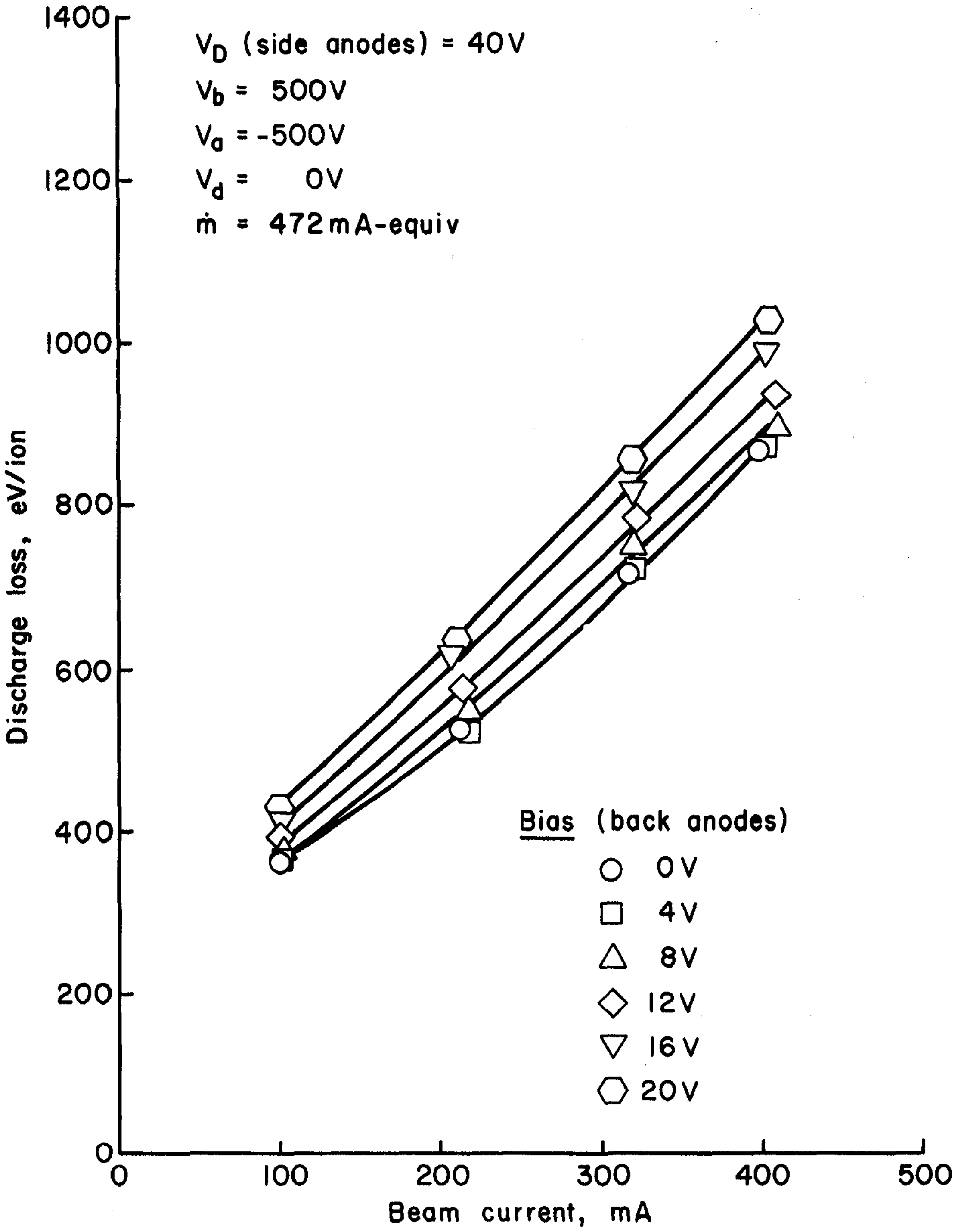

Fig. 2-33. Discharge loss versus beam current for the strip anodes in the first bias configuration. The second magnetic configuration and doubled magnetic integral were used.

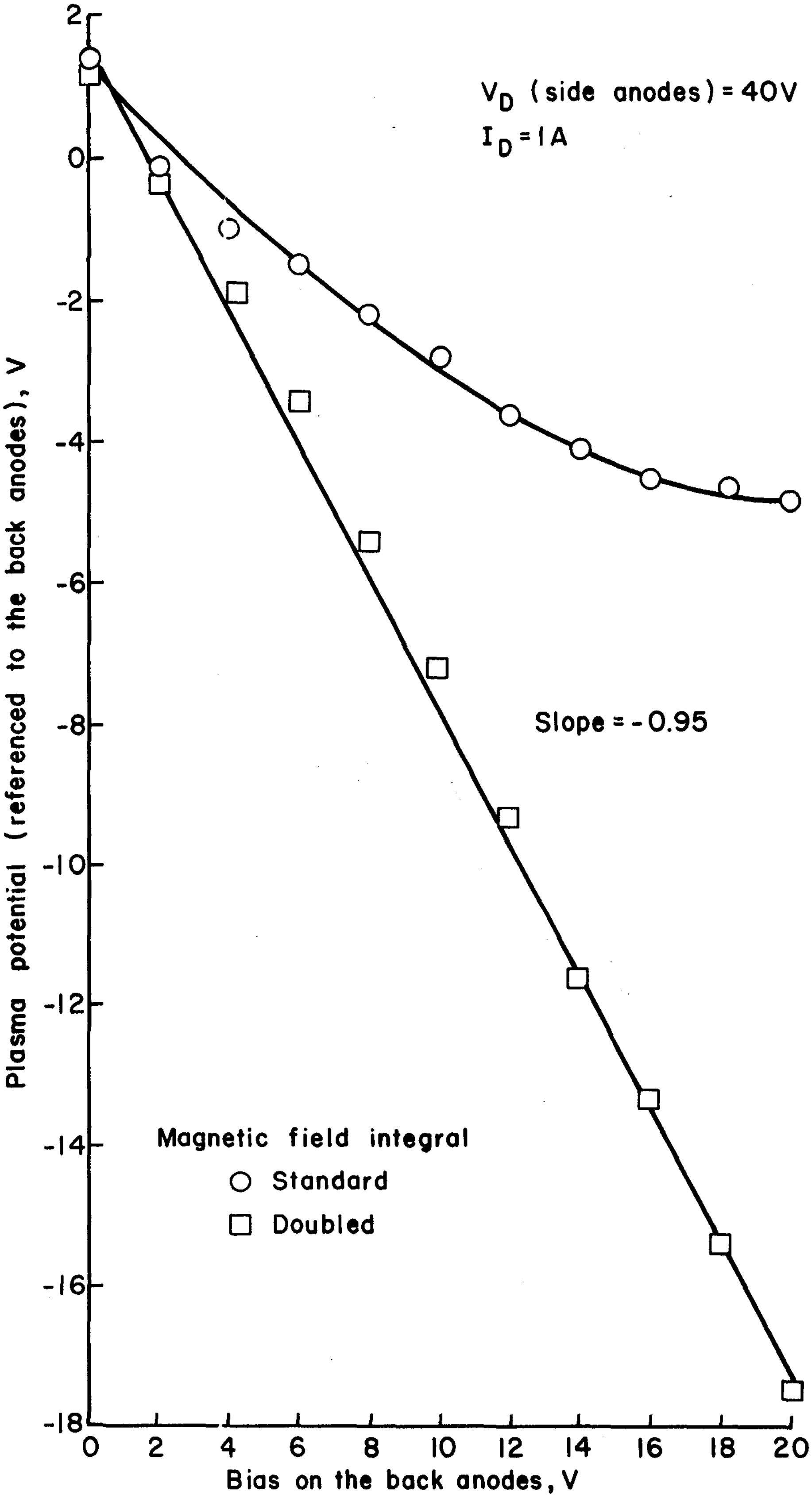

Fig. 2-34. Plasma potential versus back anode bias. (Data correspond to Figs. 2-32 and 2-33.)

doubled number of magnets results in a lower impedance connection to the plasma. Closer coupling to that plasma potential should, therefore, not be surprising.

As a second possible explanation, the exact value of the magnetic integral can be a critical matter, as shown by the effect of a 3 mm anode displacement for the wide anodes (see Fig. 2-26). Mechanical tolerances, thermal motion, and variation of field strength along the pole pieces all combine to produce spatial and timewise variation in integral values. Perhaps the mean integral for the data of Fig. 2-32 was actually slightly less than that of Fig. 2-20.

Conclusions

From the magnitudes of magnetic integrals used and the plasma potentials obtained with these magnetic integrals, it appears that considerable isolation of the anodes from the discharge plasma potential was possible at, or above, $55\text{-}60 \times 10^{-6}$ T-m. This value range for the magnetic integral is approximately what was required to prevent energetic primary electrons from having direct trajectories to the most positive anodes.

The anode width did not appear to be a major parameter in determining discharge losses.

Despite the use of several bias configurations and the frequent demonstration of anodes biased positive relative to the discharge plasma, there was no example of reduced discharge losses due to biased operation. One can infer from the absence of beneficial effects that, if ion reflection took place near the positive anodes, the added power required for biasing more than offset the gains due to ion reflection.

The most significant result of this biasing appears to be the sharp reduction in biasing losses at the high magnetic integral value (112×10^{-6} T-m). Further increases in the magnetic integral for positively biased anodes may show that the benefits of biasing may outweigh the biasing losses at sufficiently high values of this integral.

The possibility of beneficial effects of biasing at high magnetic integrals is consistent with the apparent previous observation of reduced losses,[2-3] where, although not evaluated, it is believed that very high integral values were used. The use of much higher integrals also implies the possibility of discharge stability problems. These problems were presumably the reason for the use of an auxiliary plasma anode in some earlier tests.[2-3] More recently, conductivity calculations have indicated that an excessive minimum discharge voltage can result from a high magnetic integral.[1] It is hoped that the greater knowledge of plasma processes available now would permit a rapid resolution of any stability problems.

References

1. H. R. Kaufman and R. S. Robinson, "Ion Source Design for Industrial Applications," AIAA Paper No. 81-0668, Apr. 1981. Also NASA Contr. Rep. CR-165334, Jan. 1981.

2. R. D. Moore, "Magneto-Electrostatically Contained Plasma Ion Thruster," AIAA Paper No. 69-260, Mar. 1969.

3. W. D. Ramsey, "12-cm Magneti-Electrostatic Containment Mercury Ion Thruster Development," J. Space. Rockets, Vol. 9, pp. 318-321, May 1972.

4. H. R. Kaufman, R. S. Robinson, and D. C. Trock, "Inert-Gas Thruster Technology," AIAA Paper No. 81-0721, Apr. 1981.

5. R. S. Robinson, H. R. Kaufman, and C. M. Haynes, "A 5 × 40 cm Rectangular-Beam Multipole Ion Source," AIAA Paper No. 81-0667, Apr. 1981.

6. C. M. Haynes, "Rectangular Beam (5 × 40 cm) Multipole Ion Source," NASA Contr. Rep. CR-165239, Dec. 1980.

7. W. B. Strickfaden and K. L. Geiler, "Probe Measurements of the Discharge in an Operating Electron Bombardment Engine," AIAA Journal, Vol. 1, No. 8, p. 1815, Aug. 1963.

8. H. R. Kaufman and R. S. Robinson, "Plasma Processes in Inert Gas Thrusters," AIAA Paper No. 79-2055, Oct./Nov. 1979.

III. HOLLOW CATHODES

by R. P. Stillwell

The hollow cathode investigation reported herein used oxide-free components, mechanically assembled. This approach has advantages from the research viewpoint in that such cathodes are easy to fabricate and there is no confusion as to the work functions of the surfaces involved. These advantages, in research, should eventually be translated into more rapid progress. The effectiveness of mechanically assembled construction, as opposed to electron-beam welded construction, should also be significant for future large hollow cathodes. That is, the assembled construction should avoid the thermal stress problems of welded assembly using dissimilar materials and section thicknesses.

In a previous report,[1] a rolled foil insert was found to be the most efficient oxide-free emission surface. This present investigation continues the study of a rolled foil insert. Graphite tips were also used in the previous study.[1] The work reported herein uses both graphite and tungsten tips. The internal starting electrode described earlier is also used throughout this investigation.

The propellant gas was in all cases Ar. Ar represents a greater departure than Xe from previous Hg experience, hence was felt to be more productive for a research investigation.

Apparatus and Procedure

The typical test arrangement for a hollow cathode is indicated in Fig. 3-1. The body of the hollow cathode was a 6.4 mm outside diameter Ta tube, 6.3 cm long. Unless otherwise indicated, the tube thickness was 0.25 mm. The Ta tube was mounted in an Al block, onto which the other components were connected.

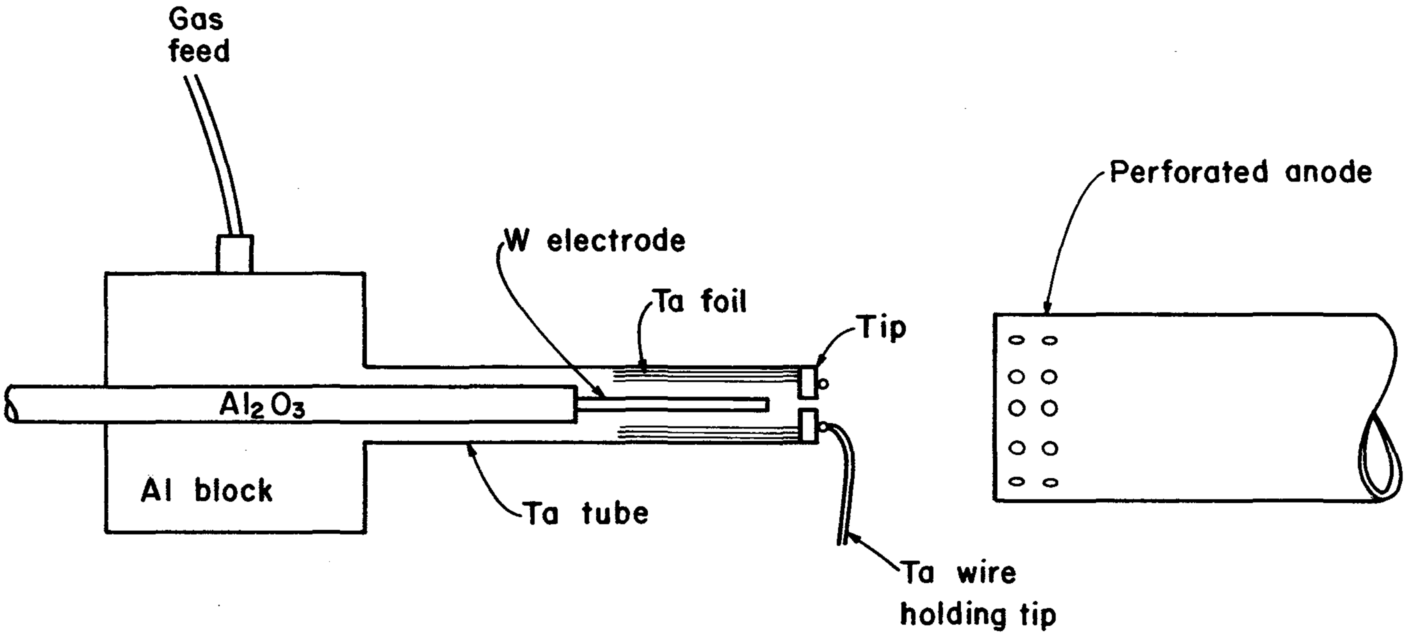

Fig. 3-1. Hollow cathode assembly.

The rolled-foil inserts used in these tests were fabricated from 0.013-mm thick Ta. The inserts were typically cut to 4 × 8.6 cm, textured by pressing the foil against 50-grit abrasive paper using an elastomer for pressure, and rolled into about a five-turn insert with a length of 4 cm. Where noted, the length (the 4 cm dimension) was varied and untextured foil was used.

A stainless steel perforated cylinder, 5 cm in diameter and 7.6 cm long, was used as the anode. The position of the anode in Fig. 3-1 is displaced for clarity. Unless otherwise specified, the tip of the cathode was flush with the near end of the anode.

The only gas introduced into the 45-cm diameter vacuum chamber was the Ar flow through the hollow cathode.

As indicated earlier, an internal starting electrode was used to initiate emission. After initiation, the starting discharge was turned off. Because there was no external source of heat after the starting discharge was turned off, a minimum emission was required to maintain operation. This minimum depended on Ar flow and cathode geometry, but was typically 3-4 A.

The testing procedure was to take current-voltage characteristics, with the current varied from the minimum required to maintain operation up to either the power supply limit (25 A) or the emission limit.[1-2] Tests were typically conducted at Ar flows of 0.6, 0.7, 0.8, 0.9, and 1.0 A-equiv.

Tip Configuration and Material

Four tip geometries, shown in Fig. 3-2, were used in this investigation. The tip shown in Fig. 3-2(a) was fabricated from graphite of

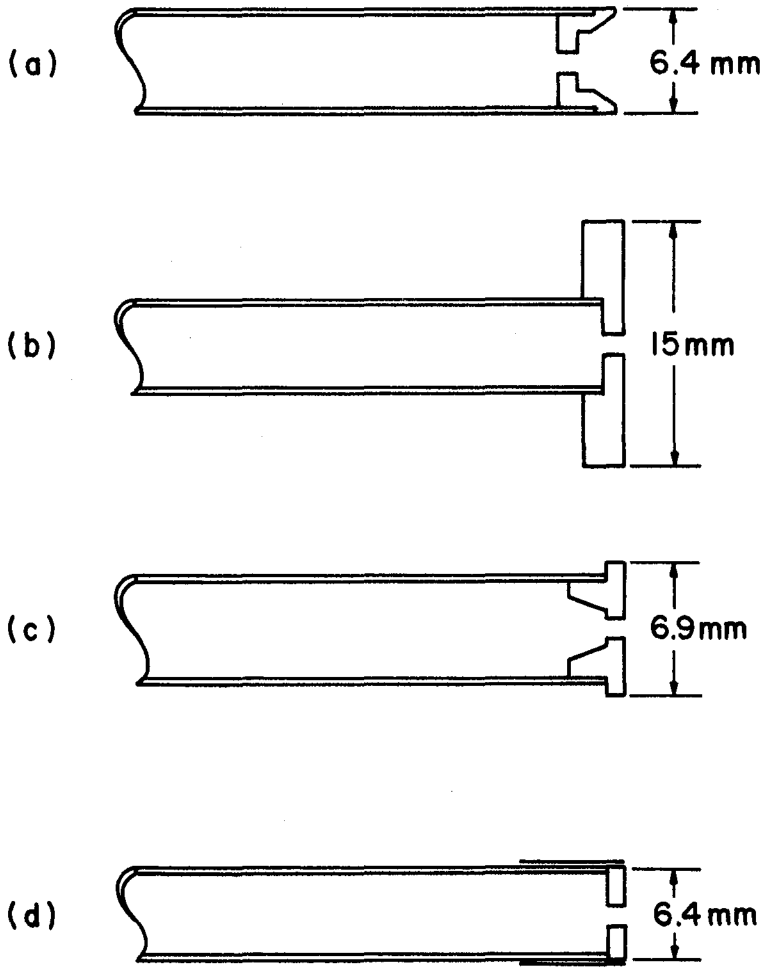

Fig. 3-2. Tip geometries.

unknown composition. The tips of Figs. 3-2(b) and (c) were fabricated from grade HPD-1 (Union Poco), which is a high density graphite that typically has trace metals in hundreds of parts per million. The tip design of Fig. 3-2(d) was fabricated from both grade HPD-1 graphite and W. In all tips the cylindrical hole length was 1 mm.

Hole diameter. Tests were initially conducted with the configuration indicated in Fig. 3-2(a), which was the final one used during the previous support period of this grant. A tip of this configuration was tested with hole diameters of both 0.71 and 1.1 mm. The ratio of powers for these two hole sizes is plotted in Fig. 3-3 as a function of emission. Since the power is proportional to the voltage when current is held constant, the ratio of anode voltage would be the same as the ratio of power shown. In all cases the power (and voltage) at a given emission level was less for the larger hole diameter.

A high discharge power is undesirable for a hollow cathode from the viewpoint of excessive losses. It is also undesirable from the viewpoint of the high sputtering rates encountered at higher voltages. For the main discharge cathode of an inert gas thruster, then, the larger hole diameter would be preferred. It should be kept in mind, however, that the 1 mm thickness in the vicinity of the tip hole was a selection based, in part, on the requirement for long thruster lifetime and past wear rates encountered with Hg. The smaller 0.71 mm diameter hole thus had a length-to-diameter ratio of 1.4, while the 1.1 mm diameter hole had a ratio of 0.9. With the longer length-to-diameter ratio, the smaller hole was a considerably greater obstacle to plume-neutralizing ions diffusing from the inside to the outside - much greater than would be indicated by the hole cross sections alone. If wear rates were low enough to permit thinner tips to be used, some of

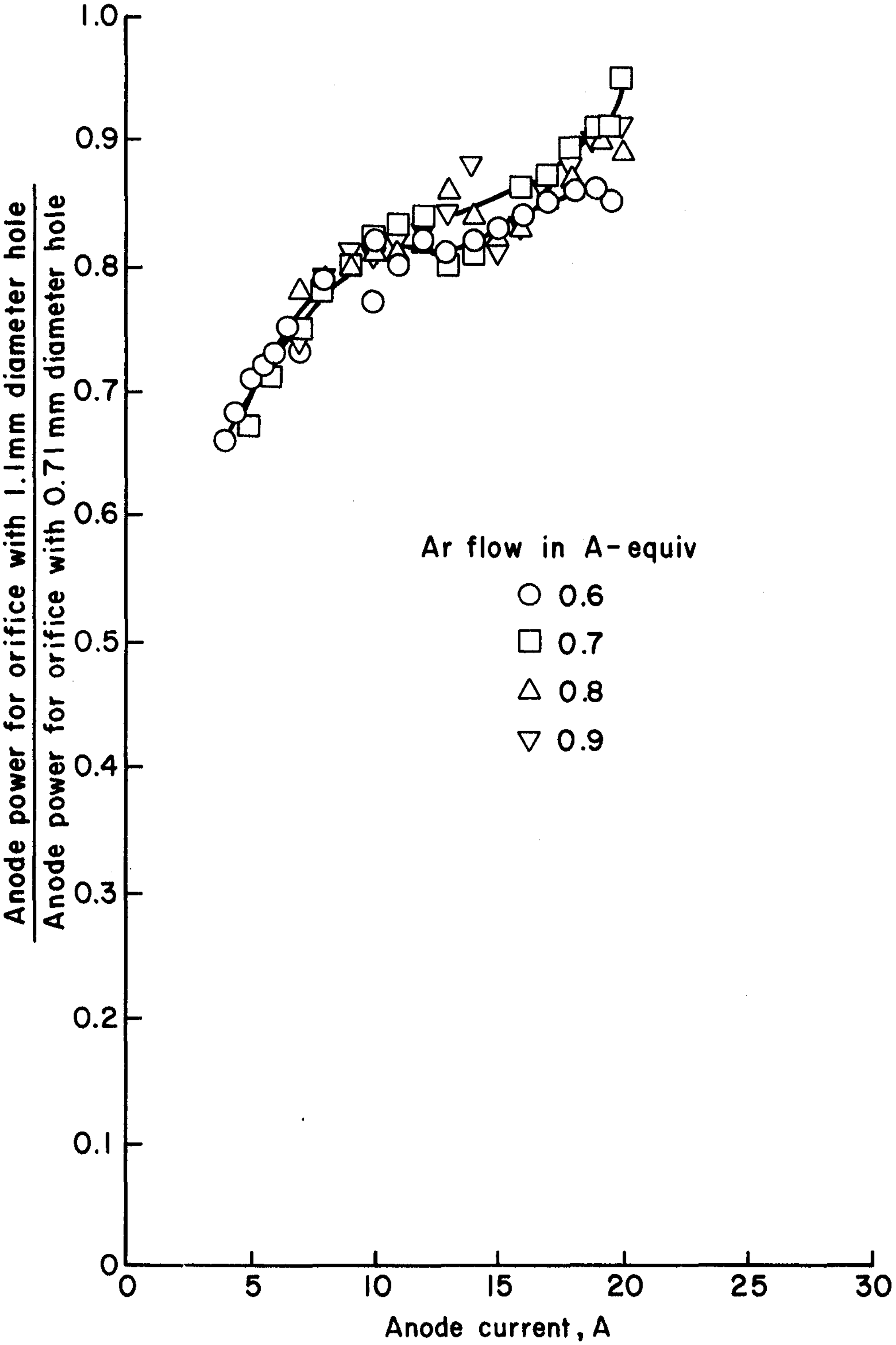

Fig. 3-3. Comparison of cathode performance with two orifice diameters, for the tip geometry of Fig. 3-2(a) and textured insert.

the adverse effects of a smaller hole diameter, shown in Fig. 3-3, might not be observed.

Radiation area. The tip geometries shown in Figs. 3-2(a) and (b) were chosen to permit comparison of considerably different thermal designs. The design of Fig. 3-2(b), with a diameter of 15 mm, had a large external radiating area. The design of Fig. 3-2(c) has a much smaller external radiating area, although the area exposed to the internal plasma was increased at the same time.

The experimental performance for these two configurations is shown in Fig. 3-4. The only clearcut difference is that for the higher Ar flow rates (0.8 and 0.9 A-equiv. in Fig. 3-4(c) and (d)), the maximum emission is higher for the smaller tip diameter.

The data in Fig. 3-4 also illustrate a trend evident throughout this investigation. That is, as the flow rate of Ar increased, the maximum emission also increased.

Erosion rate. A problem encountered with the graphite tips was that of rapid erosion. This problem was first encountered with the graphite tip indicated in Fig. 3-2(a). Because the graphite composition was unknown for this tip, it was decided that the erosion should be evaluated for a tip of known composition. Using the tip design of Fig. 3-2(c), made of HPD-1 graphite, the tip hole was observed to increase from 0.71 mm to 1.0 mm during 19 hours of operation. The hole diameter was measured after every few hours of operation, so that this is known to be a continual erosion process rather than rapid wear during a short time at some unusual operating condition. The erosion process involved in this rapid wear is not clear. The sputter yield of graphite is quite low, so it does not appear that simple sputter erosion can be the main cause.

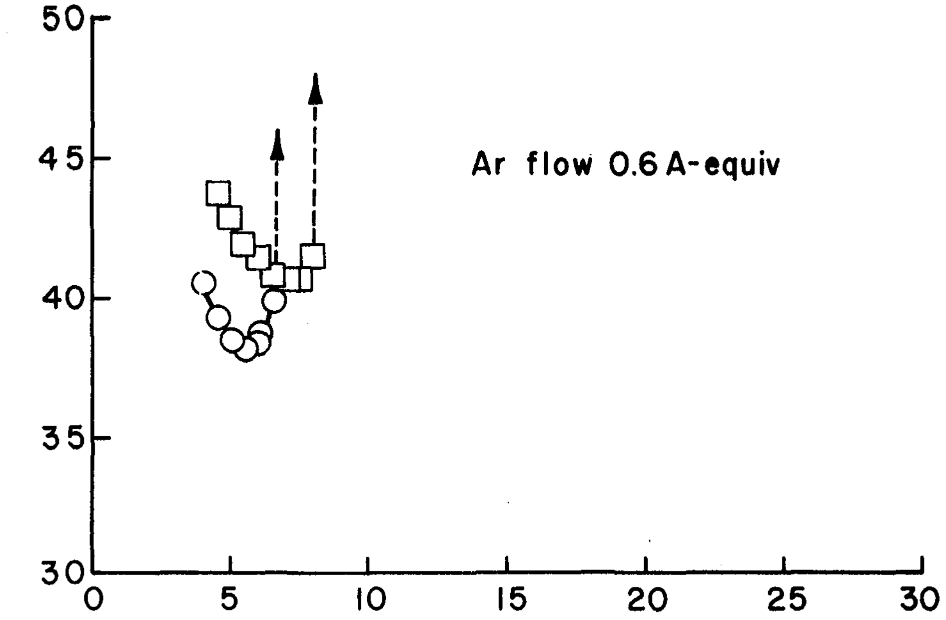

(a) 0.6 A-equiv Ar flow.

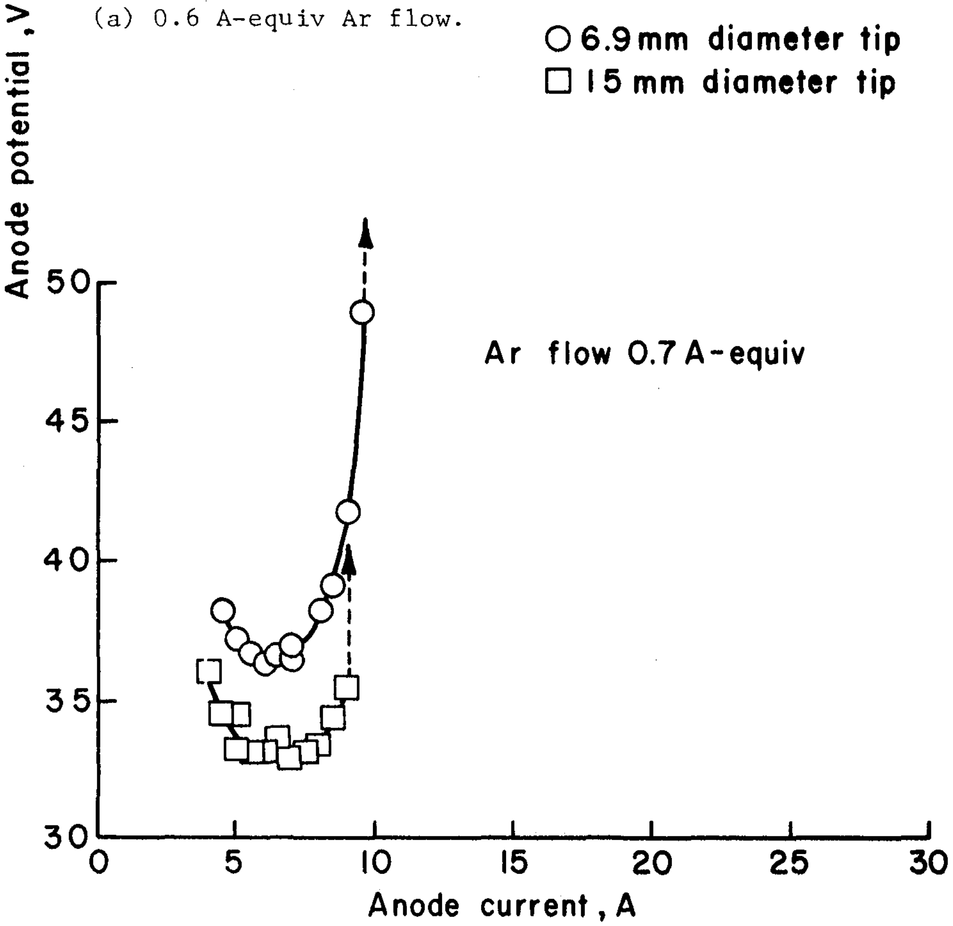

(b) 0.7 A-equiv Ar flow.

Fig. 3-4. Comparison of two tip geometries with orifice diameter of 0.71 mm and a plain insert.

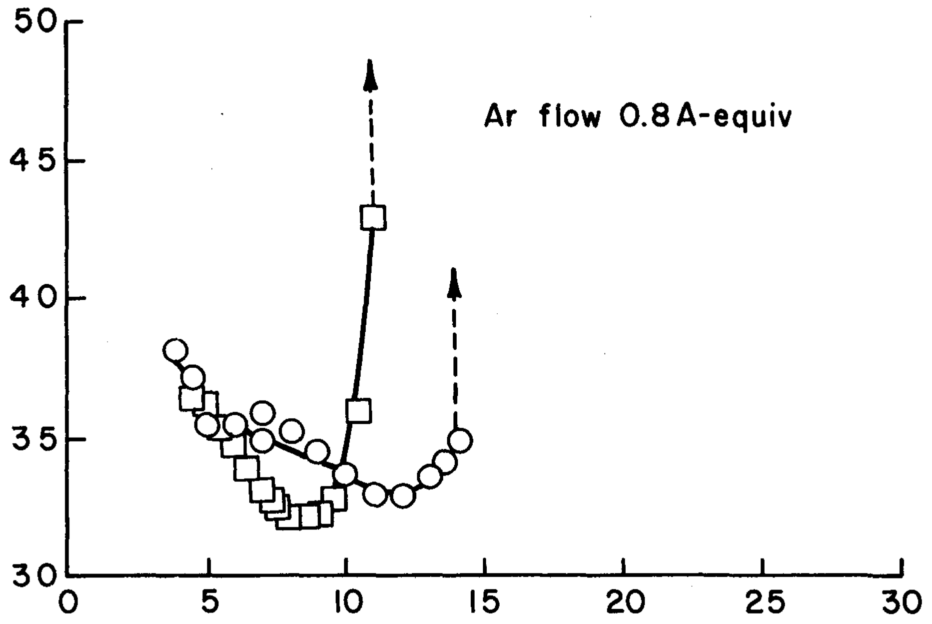

(c) 0.8 A-equiv Ar flow.

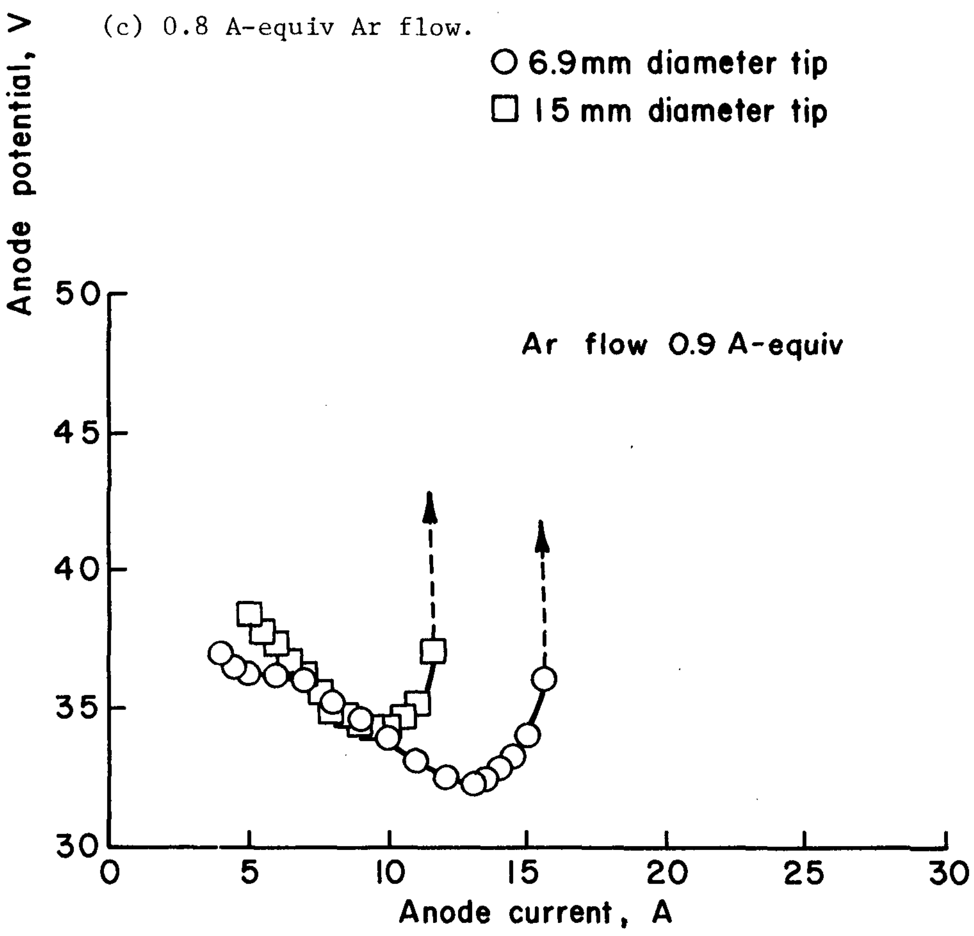

(d) 0.9 A-equiv Ar flow.

Fig. 3-4. (Concluded)

Tip material. The erosion rate found for the graphite tip was clearly unacceptable for space applications. In an attempt to reduce orifice erosion, it was decided to try W for the tip material. Due to the difficulty in machining W, the simple design of Fig. 3-2(d) was adopted. The tip was a 6.4 mm diameter disc, 1 mm thick, with a centered 1.0 mm diameter hole. Since this design is a simple disc without provision for centering in the Ta tube, a 0.013-mm-thick piece of Ta was spot welded to the Ta tube to perform this centering function. This W tip was operated for 16 1/2 hours with no measurable wear evident with an optical microscope.

Because the change in tip material was associated with a change in design, a similar tip configuration was also fabricated from HPD-1 graphite. The cathode performance obtained using the two tip materials is indicated in Fig. 3-5. At all combinations of emission and Ar flow that could be compared, the W tip showed lower powers and voltages than the graphite tip. In addition, the maximum emission was increased by the use of W.

The difference in power required for the two tip materials is consistent with the hypothesis that the plasma discharge supplies whatever power is required for the emission surface to reach emission temperature.[1*] Because the potential variation is small from the anode to the plasma within the hollow cathode, most of the discharge power (emission times anode-cathode potential difference) appears as cathode heat. Because the plasma is densest near the cathode tip, much of this heat is lost to the tip. Graphite has an emissivity in the operating

---

[*] The emission within a hollow cathode is believed to be by a combination of thermionic and high-field processes. The concern here is only with the effect of temperature.

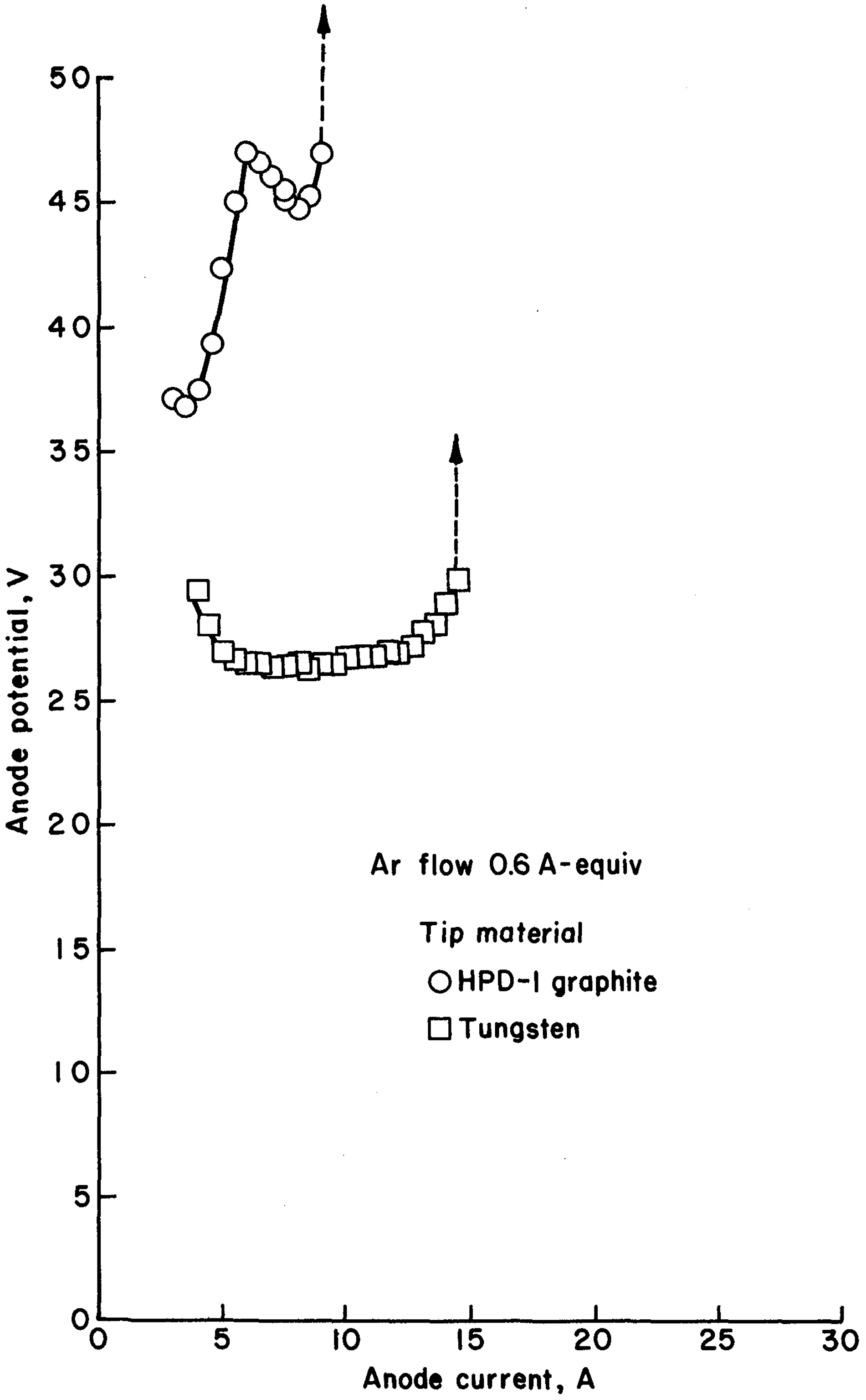

(a) 0.6 A-equiv Ar flow.

Fig. 3-5. Comparison of hollow cathode performance with graphite and tungsten tips. (Tip of Fig. 3-2(d) with 1.0 mm diameter orifice, textured insert, and thick walled cathode tube.)

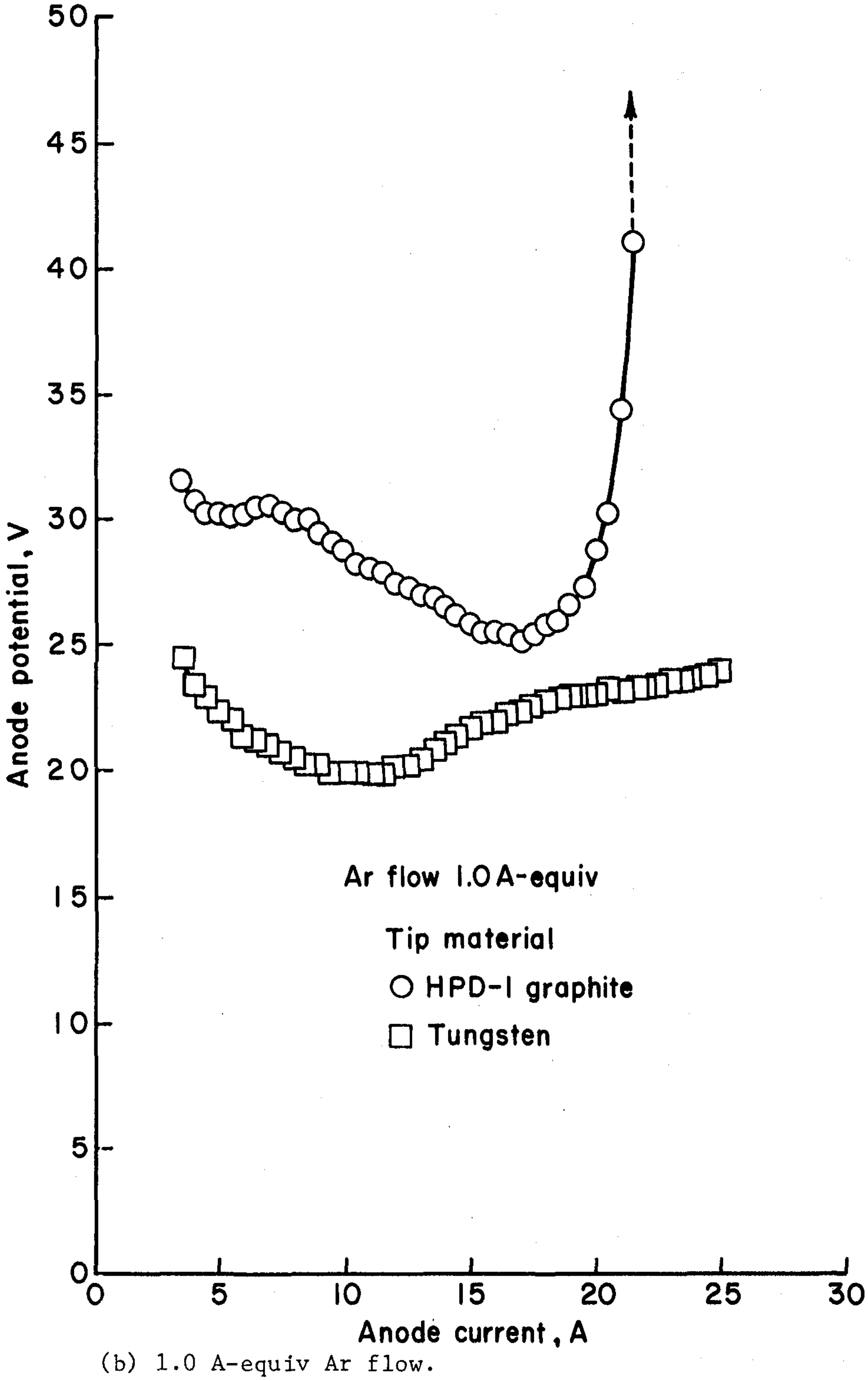

(b) 1.0 A-equiv Ar flow.

Fig. 3-5. (Concluded)

range for temperature of 0.80-0.85, while that of W is 0.2-0.3. The lower power required for the W is therefore explained as simply due to lower heat loss with this material. While the tip, itself, is not believed to be a source of significant emission, its heat balance will directly affect the inside temperature of the foil insert, which is believed to be the major emission source.

Note that the more efficient thermal design (with W) had higher maximum emissions. This is similar to the trend observed with different tip diameters (Figs. 3-2(b) and (c)). It is suspected that the difference in internal configuration obscured some of the difference that might otherwise have been expected with different tip diameters.

Insert configuration. After the cathode emission has been initiated by the starter electrode, the discharge power is the only heat input to the cathode. As discussed previously, most of the discharge power appears as heating power inside the cathode. A change in insert configuration that reduces heat flow to the outside of the cathode should thus be expected to reduce the power required to maintain emission temperature at the inside of the insert, which, in turn, should reduce the anode voltage required for a given emission level.

With this reasoning in mind, textured (described in the Apparatus and Procedure section) and untextured foil inserts were compared in terms of operating characteristics. The intent of the texturing was, of course, to minimize contact between foil layers. At the high operating temperatures for the inside layers of the foil insert, some bonding would be expected to take place at any contact area. With plain surfaces, a high degree of direct thermal loss would be expected after this bonding takes place. With a textured surface, though, thermal conduction must follow a labyrinth path.

The textured-to-plain power ratio is presented in Fig. 3-6 for several Ar flow rates. In all cases the textured insert showed substantial (10-40%) reductions in discharge power.

The insert length was also varied. One might expect a shorter insert to provide less insulation for thermal conduction to the Ta tube, hence be less efficient. On the other hand, experience with oxide coated inserts indicates that most of the emission is from the first 2 mm near the tip.[3] Three insert lengths were tested: 1, 2.5, and 4 cm. These tests employed a W tip with a 1.0 mm hole diameter (Fig. 3-2(d)). As indicated in the Apparatus and Procedure section, textured inserts were used. The results of these tests are shown in Fig. 3-7.

The tests of different insert lengths did not show a clearcut result for voltage at a given emisison, hence for heating power. Where differences were found, the medium length (2.5 cm) showed the lowest anode voltage. For maximum emission, the highest value was found for the shortest insert. Depending on the parameter of interest, then, somewhere in the 1-2.5 cm range of length appeared of most interest.

Tube thickness. The Ta tubes used in previous hollow cathode investigations[1-2] and in the majority of the studies reported herein had 0.25 mm-thick walls. When ordering more Ta tubing for this investigation, it was found that the 0.25-mm wall thickness was no longer available for the 6.4 mm outside diameter used herein. The closest that could be obtained to the original tubing had a wall thickness of 0.51 mm. This change in wall thickness resulted in tests to determine the effect of this change on performance.

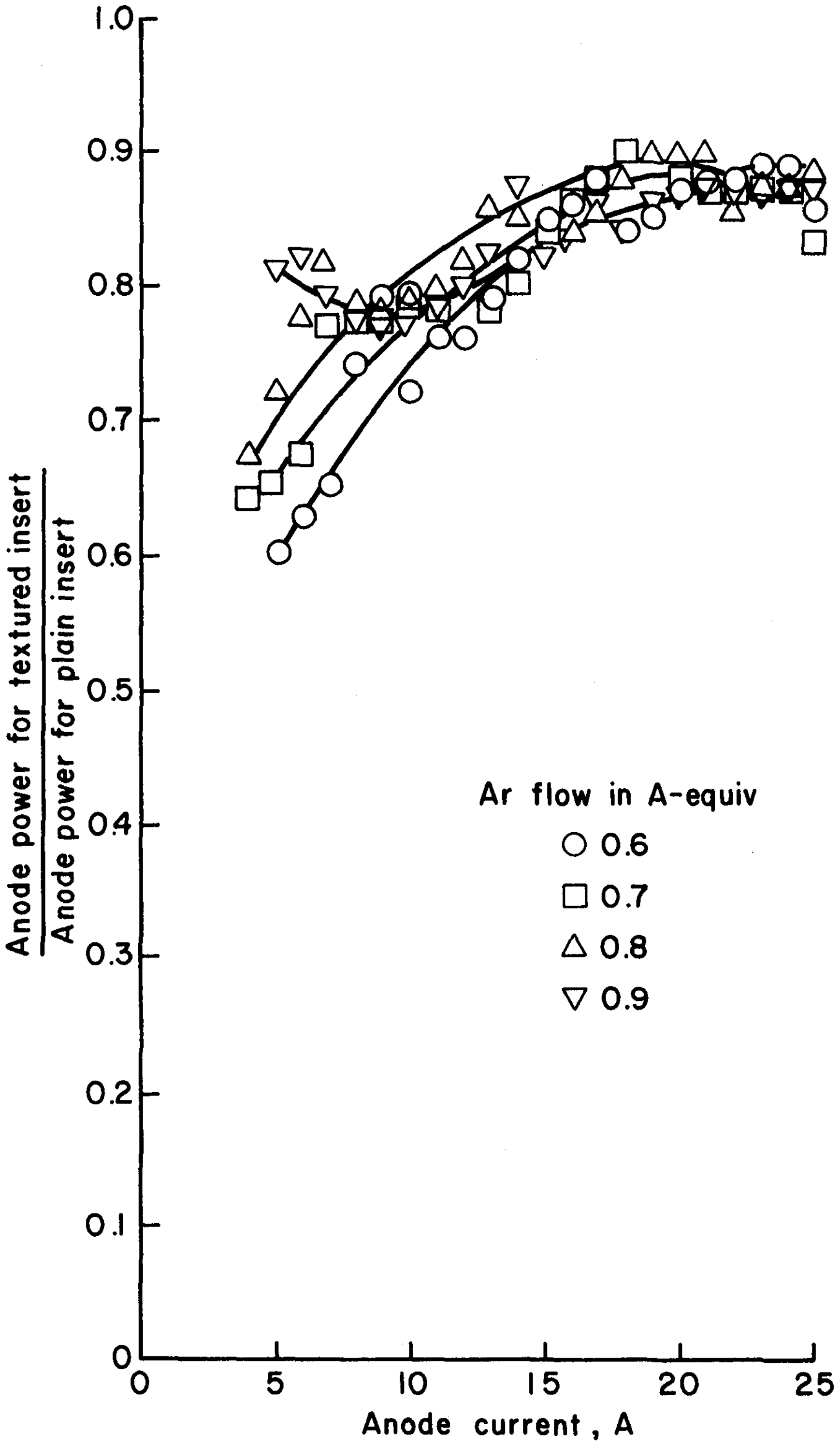

Fig. 3-6. Comparison of cathode performance for textured and plain inserts. (Tip geometry of Fig. 3-2(a) with 1.1 mm orifice diameter.)

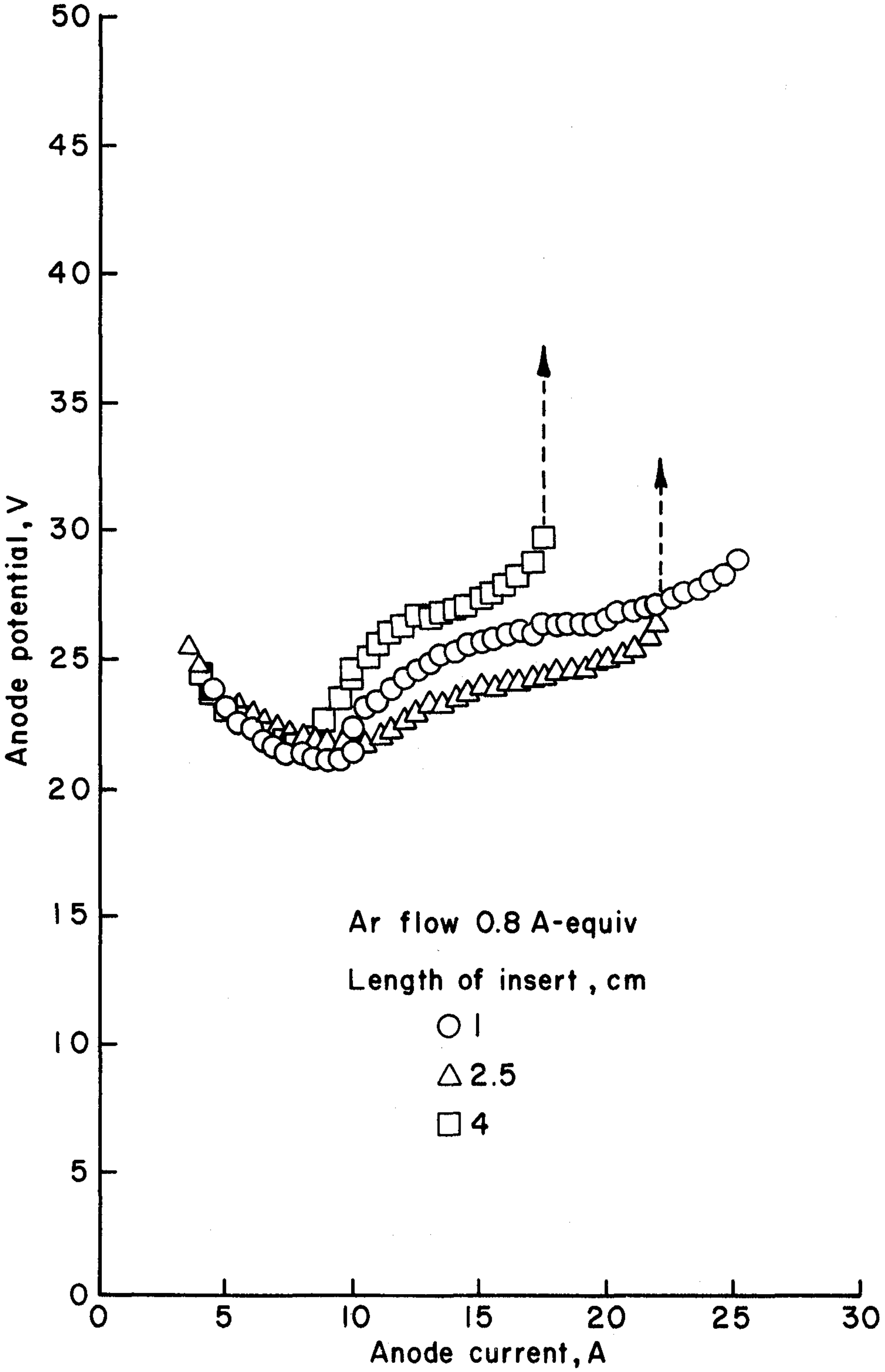

Fig. 3-7. Comparison of cathode performance with different insert lengths. (Tungsten tip used with 1.0 mm diameter orifice, textured insert, and thick walled Ta tube.)

The effect of wall thickness is shown in Fig. 3-8 for an Ar flow of 0.8 A-equiv. In all cases tested, the thin-walled tubes showed somewhat higher maximum emissions. For the purposes of the investigation reported herein, the change in wall thickness was not considered to be critical.

Magnetic field. A magnetic field was used with a hollow cathode in an attempt to increase the maximum emission. The attempt was not successful, but is reported here because it might be of interest.

As indicated several times in discussions of this investigation, a maximum electron emission is encountered for each combination of Ar flow rate and hollow-cathode configuration. A possible reason for this limit is the "starvation" of the discharge due to the too rapid escape of electrons. No similar maximum has been encountered with Hg propellant. It may be that a similar limit does, in fact, exist with Hg, but is simply at too high an emission to be encountered in the usual experiments.

In comparing cross sections of Ar with those of Hg, it is apparent that, for electrons with of the order of 1 eV energy, the ratio of ionization to collision cross section is much smaller for Ar than for Hg. This observation is consistent with the Ramsauer-Townsend effect, generally observed with inert gases.

The hope was that the presence of a transverse magnetic field would enhance the collisional processes with an inert-gas propellant, resulting in performance close to that observed with mercury.

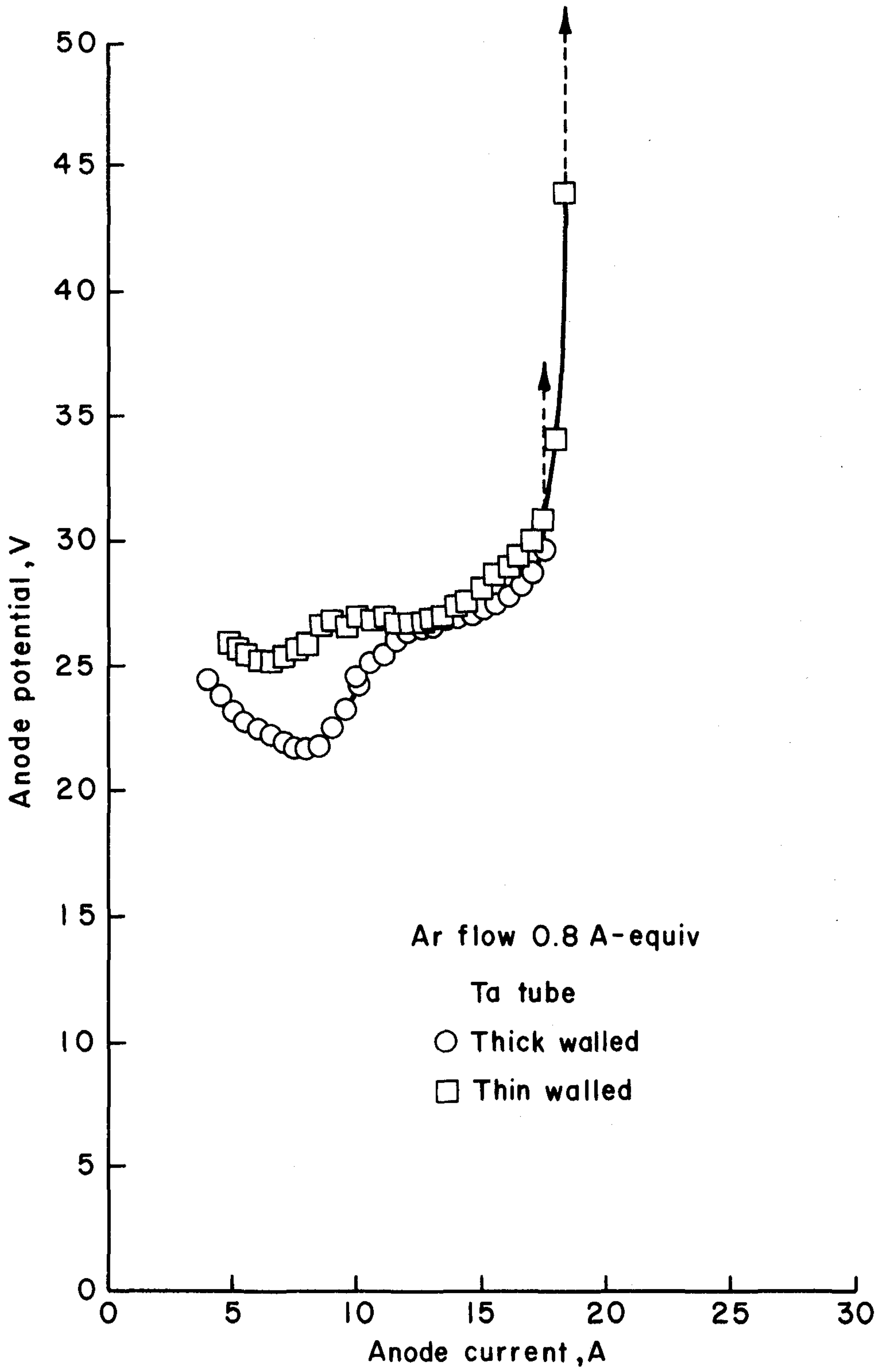

Fig. 3-8. Comparison of cathode performance for thick and thin walled cathode tube. (Tungsten tip with 1.0 mm diameter orifice used with textured insert.)

A change in anode position was necessary to provide space for the magnets between the anode and cathode. Tests were therefore conducted to determine the effect on performance of this change. The anode change investigated, and used as a basis of comparison with a magnetic field, was with a 1.5 cm gap between the cathode tip and the near end of the anode. This 1.5 cm change in anode position did not result in a significant performance change when no magnetic field was introduced.

The first magnetic configuration tested used 6.4 mm diameter magnets positioned radially with respect to the cathode axis of symmetry, as indicated in Fig. 3-9(a). Magnet separations (see Fig. 3-9(a)) of 0.7, 1.5, 2.0, and 3.0 cm were tested, but only with a 3.0 cm separation could the cathode discharge be started. The magnetic field for a 3.0 cm separation is shown in Fig. 3-10(a). The magnetic integral downstream from the orifice was 217 Gauss-cm for this configuration.

From discharge-chamber tests, 217 Gauss-cm should be considered a high value of integral. Another configuration, shown in Fig. 3-9(b), was devised to obtain a lower value of integral. The magnetic field for this latter configuration is shown in Fig. 3-10(b). The integral downstream from the orifice was found to be 52 Gauss-cm for this lower field configuration.

The performance of the configuration shown in Fig. 3-9(a) is compared to that of a similar configuration without magnets in Fig. 3-11. The most noticeable change is the general 10-15 V increase in anode voltage with the presence of a magnetic field. The maximum emission was only slightly increased by the magnetic field.

The performance of the configuration shown in Fig. 3-9(b) is compared with that of a similar configuration without magnetic field

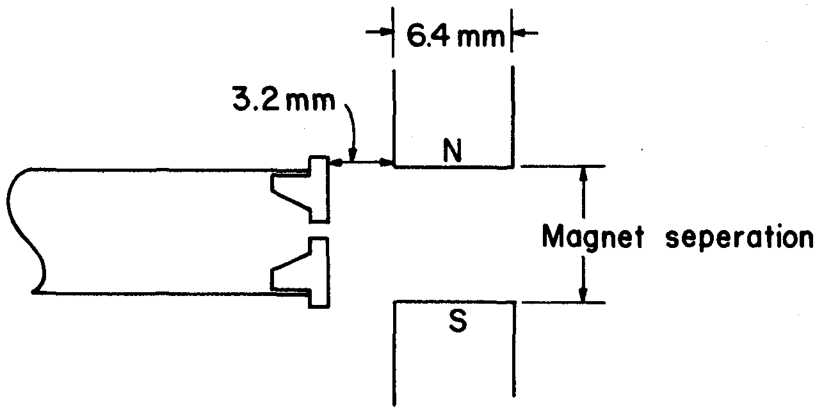

(a) Cylindrical magnets.

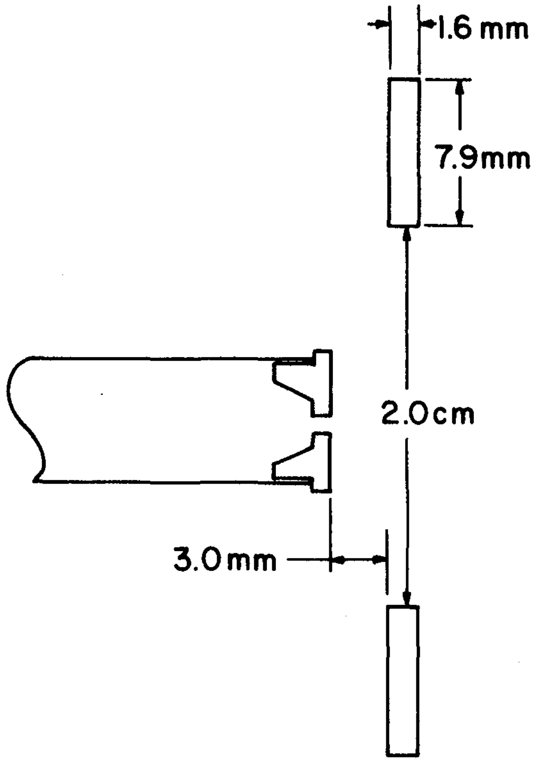

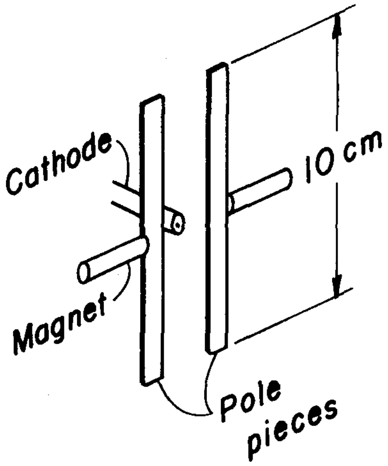

Assembly of configuration in Fig. 3-9(b).

(b) Strip pole pieces (magnet not shown).

Fig. 3-9. Magnetic field configurations.

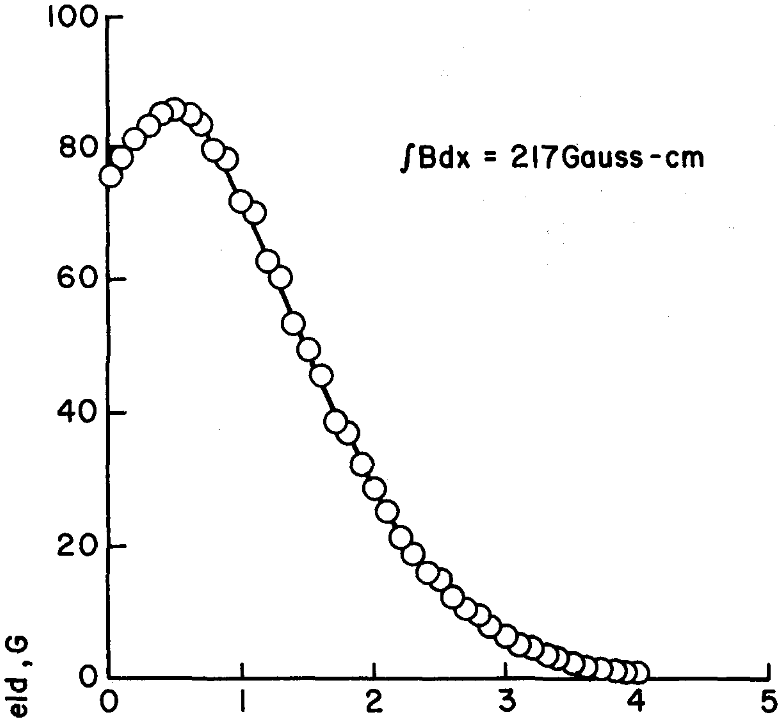

(a) 3.0 cm magnet separation.

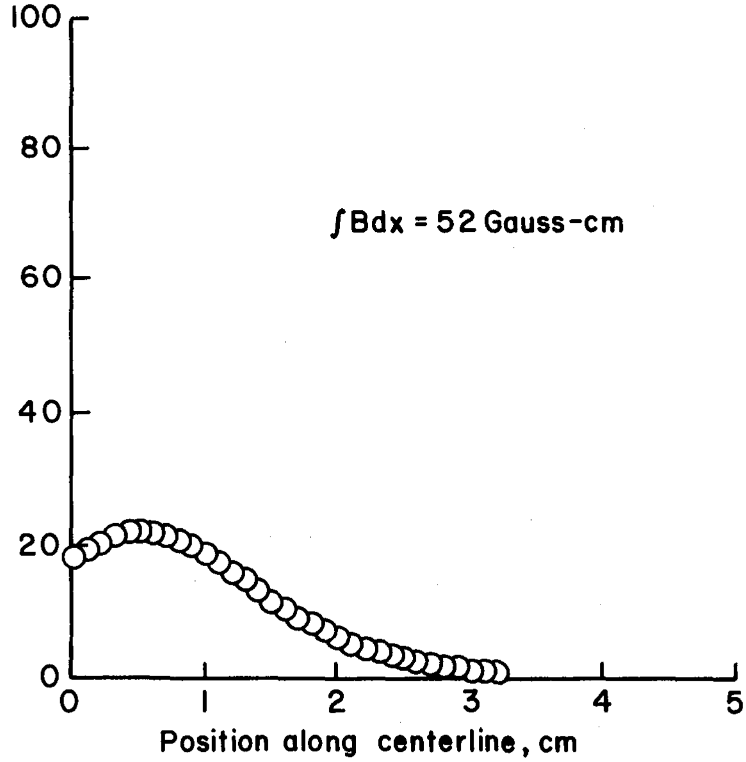

(b) 2.0 cm magnet separation.

Fig. 3-10. Magnetic field profiles for cylindrical magnets positioned radially to cathode axis.

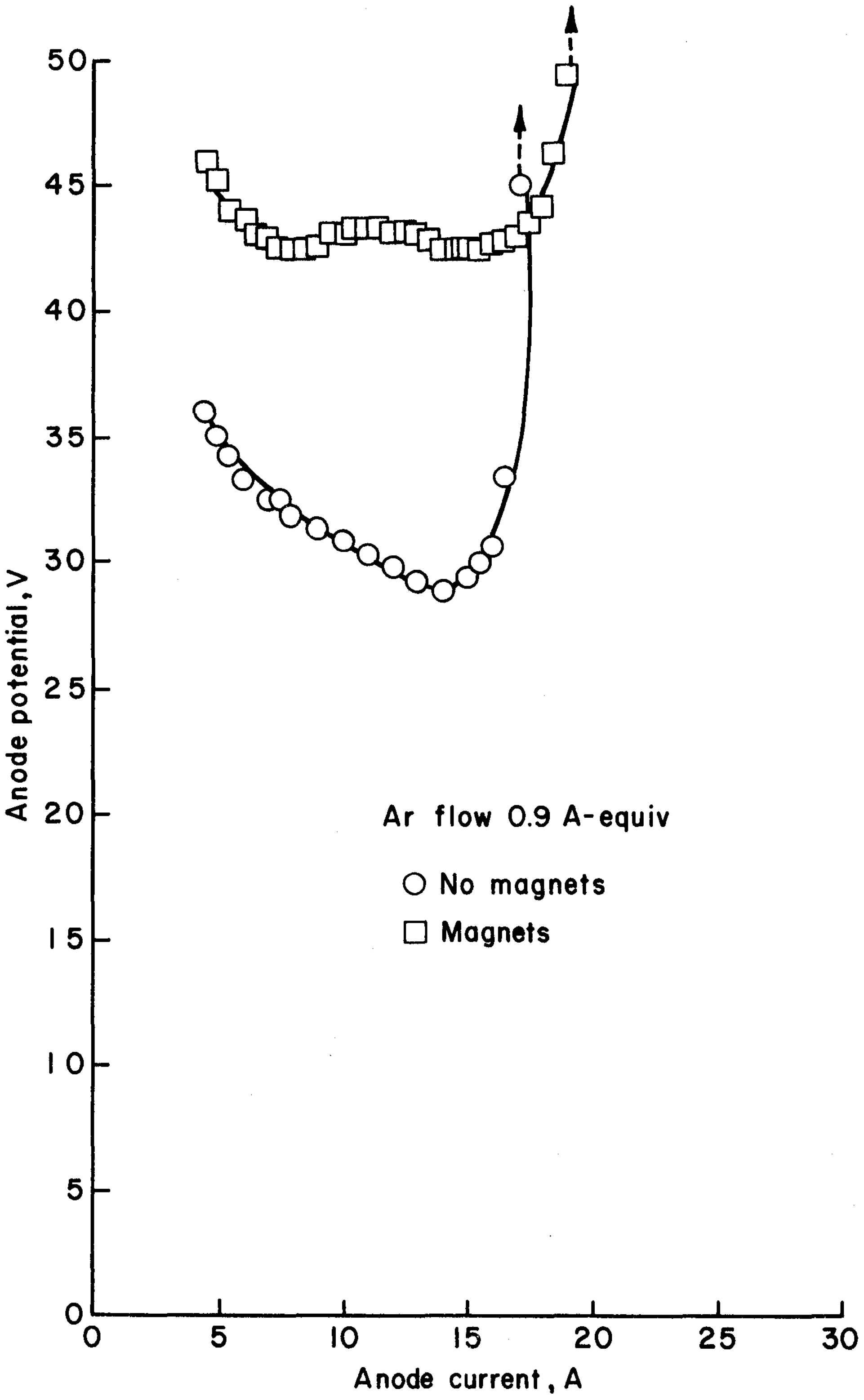

Fig. 3-11. Comparison of cathode performance with and without the magnetic field. (Cylindrical magnets 3 cm apart. Tip of Fig. 3-2(c) used with orifice diameter 0.76 mm and plain insert.)

in Fig. 3-12. With the smaller magnetic integral of 52 Gauss-cm, the increase in anode voltage due to the presence of the magnetic field is only about 5 V. There was no significant trend for maximum emission.

Also shown in Fig. 3-12 are the results of locating the pole pieces of Fig. 3-9(b) upstream of the orifice, instead of downstream as shown in that figure. The results are intermediate of the downstream configuration and the no magnetic field field configuration. This result is consistent with the magnetic integral downstream of the orifice being reduced below 52 Gauss-cm. No significant results appear to be due to the magnetic field increase upstream of the orifice.

The tests conducted with transverse magnetic fields in the plume region thus covered a range of anode voltage effect from <5 V to 10-15 V as the magnetic integral of the transverse magnetic field downstream of the orifice was increased. If beneficial effects on maximum emission were possible, they should have been evident in the range covered.

Conclusions

A number of detailed conclusions were drawn from the oxide-free hollow cathode tests described herein. The use of graphite as tip material resulted in unacceptably high erosion rates. The substitution of W for graphite greatly reduced this erosion. The use of W for the tip also reduced the required discharge power at a given Ar flow rate and emission level. Power reductions (up to 40%) were also found for a textured foil insert, compared to a plain one. Higher maximum emissions for a given Ar flow rate were also found with the W tip. No beneficial results were observed for a transverse magnetic field downstream of the orifice.

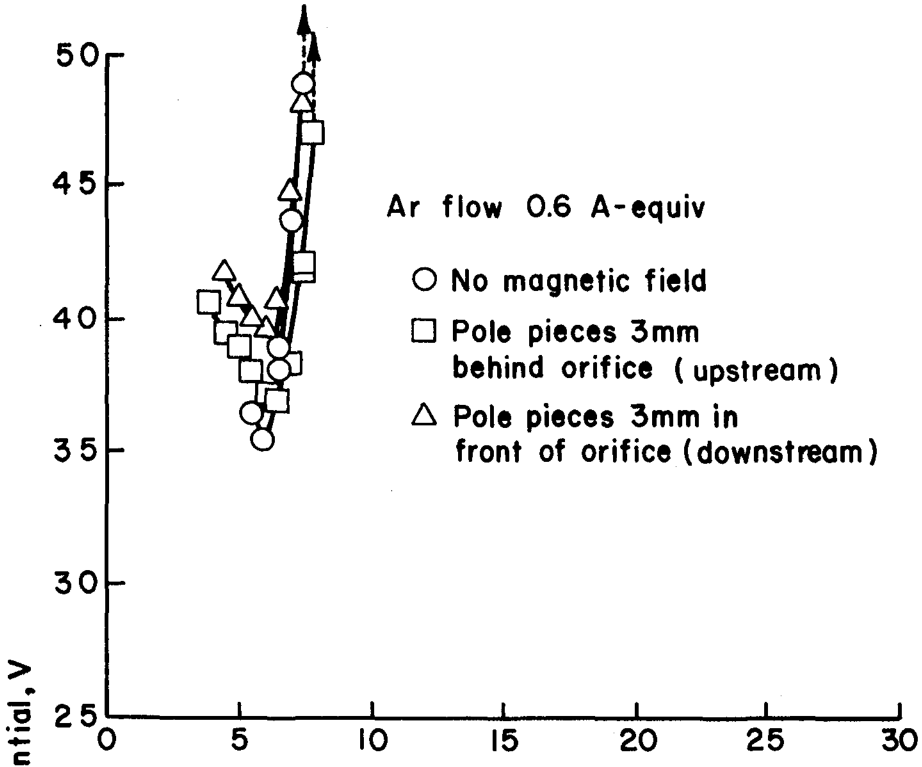

(a) 0.6 A-equiv Ar flow.

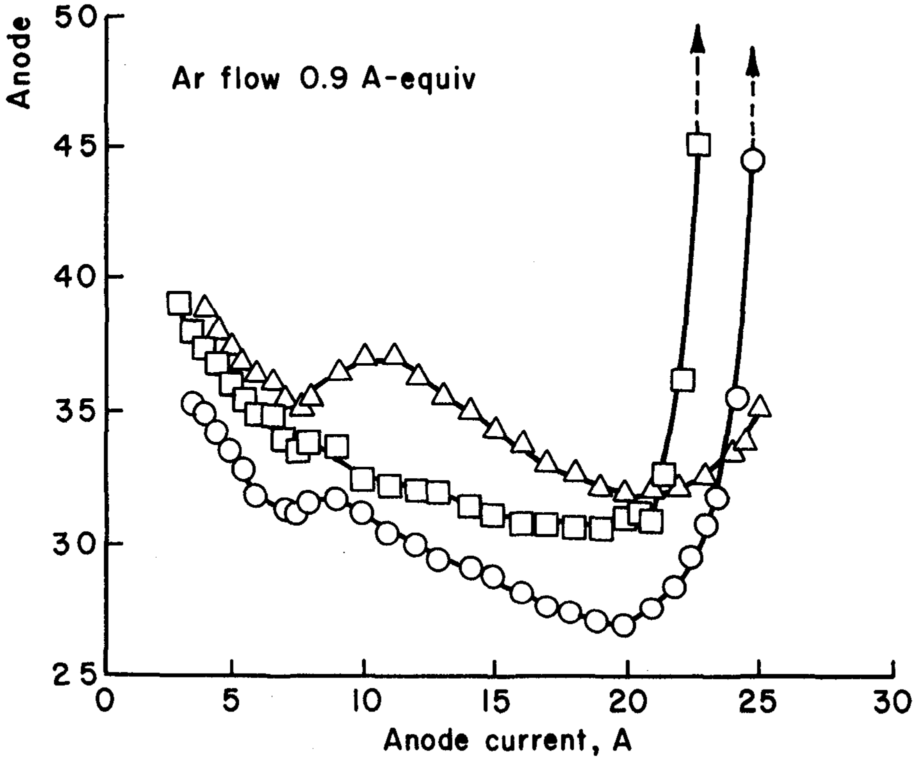

(b) 0.9 A-equiv Ar flow.

Fig. 3-12. Comparison of cathode performance with and without the magnetic field. (Pole pieces 2 cm apart. Tip of Fig. 3-2(c) used with orifice diameter of 1 mm and plain insert.)

The results observed for oxide-free hollow cathodes are generally in agreement with a thermally controlled model, where the anode voltage reaches whatever value is necessary to maintain emission temperature at some surface. For the designs tested, this surface is almost certainly the inside of the rolled foil insert.

The ability to define surface work function (with no emissive oxide present) makes the oxide-free design well suited to a more thorough analysis of the interplay between emission and thermal losses. The non-welded, mechanically assembled construction also appears to be promising for future large-cathode applications, where thermal-expansion problems could be serious at welds.

From the absence of any beneficial effect of a transverse magnetic field downstream of the orifice, it appears that the too-rapid escape of electrons to the anode may not be a significant factor in the maximum electron emission observed for each combination of inert-gas flow rate and cathode configuration.

References

1. H. R. Kaufman and R. S. Robinson, "Inert Gas Thrusters," NASA Contr. Rep. CR-165332, Dec. 1980.

2. H. R. Kaufman and R. S. Robinson, "Inert Gas Thrusters," NASA Contr. Rep. CR-159813, Nov. 1979.

3. D. Siegfried and P. J. Wilbur, "Studies on an Experimental Quartz Tube Hollow Cathode," AIAA Paper No. 79-2056, Oct. 1979.

IV. EXPERIMENTAL HALL-CURRENT ACCELERATOR

by Gregory M. Plank

Electric propulsion needs for interplanetary missions appear to be best met by specific impulses of 3000 sec or more, depending on mission difficulty. The electrostatic thruster, with ion acceleration provided by electric fields between closely spaced grids, performs well in this specific impulse range.[1-2]

For geocentric missions, a lower range of specific impulse appears to be of interest, probably 3000 sec, or less. The need for lower specific impulses in geocentric applications results from considerations of mission lifetime. In interplanetary missions, the added mission time associated with the use of electric propulsion is usually a small fraction of total mission time. In geocentric missions, however, a mission time of hundreds of days can be a serious problem when the equivalent chemically propelled mission takes only a few hours.

The most serious obstacle to the use of electrostatic thrusters at low specific impulses (<3000 sec) is probably the ion-current limitations of electrostatic acceleration. Hall-current acceleration is an alternative to electrostatic acceleration between grids.

Hall-current accelerators have been studied as electric thrusters in the past in this country, but were dropped because of low efficiency.[3-4] It was, for example, difficult to accelerate more than about one ion downstream for each electron that traveled upstream. This limitation put an upper limit on thruster efficiency of about 50% due to the acceleration process alone. In comparison, the electrostatic thruster has an overall efficiency of about 70% at 3000 sec, and is capable of higher efficiencies at higher specific impulses. This relatively poor performance of the Hall-current accelerator at the high specific impulses that were then being considered resulted in its demise in the U.S. about 1970.

If we consider low specific impulses, though, the relative performance of the Hall-current accelerator is at much less of a disadvantage. As indicated above, the electrostatic thruster becomes increasingly limited in ion current capacity as specific impulse is reduced. The Hall-current accelerator has no such limitation. The electron backflow results in a serious loss at high specific impulses. But at low specific impulses this backflow is more easily recovered by using it to generate ions.

The investigation of the Hall-current accelerator reported herein was undertaken as part of a preliminary attempt to re-evaluate this type of thruster for electric propulsion. The preliminary nature of this investigation should be emphasized. It has been over a decade since the Hall-current accelerator was last seriously considered for electric propulsion in the U.S.

Apparatus and Procedure

Ion acceleration in a Hall-current thruster is due to the electric field generated by an electron current interacting with a magnetic field. The generation and shape of this magnetic field is thus equivalent in importance to the design of grids in electrostatic thrusters.

Construction. The Hall-current thruster investigated herein (Fig. 4-1) uses two cylindrical magnetic pole pieces to generate an essentially radial magnetic field. As indicated in Fig. 4-2, a nonmagnetic annular anode is located at the upstream end of the

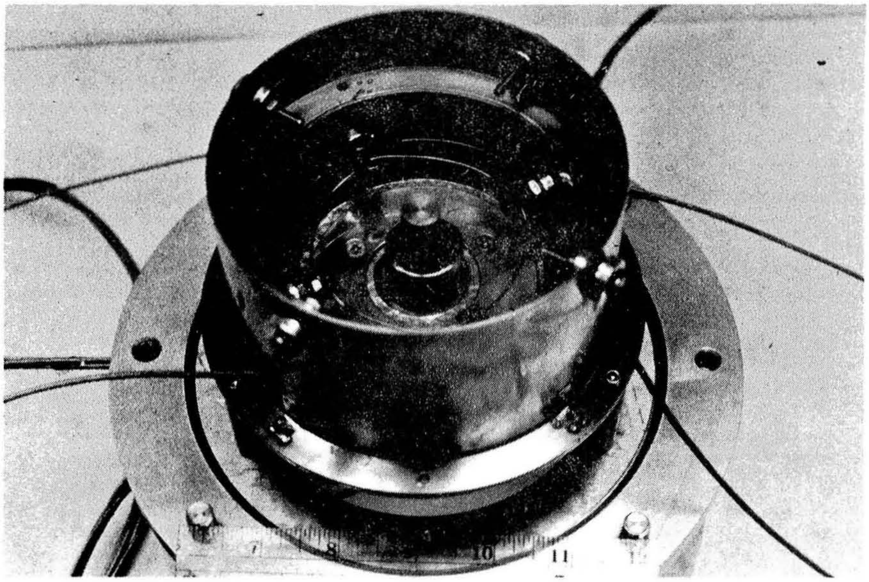

(a) Upstream view (open end).

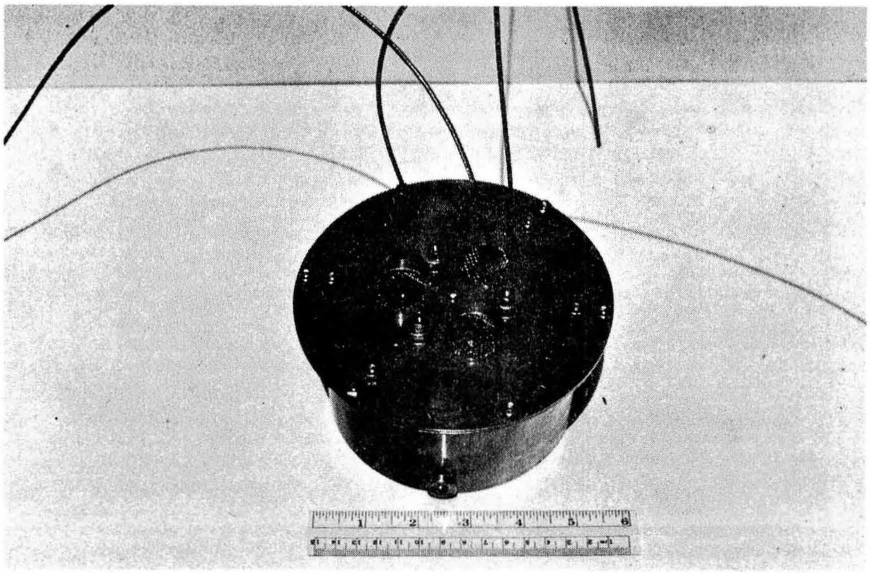

(b) Downstream view (closed end).

Fig. 4-1. Photographs of Hall-current thruster.

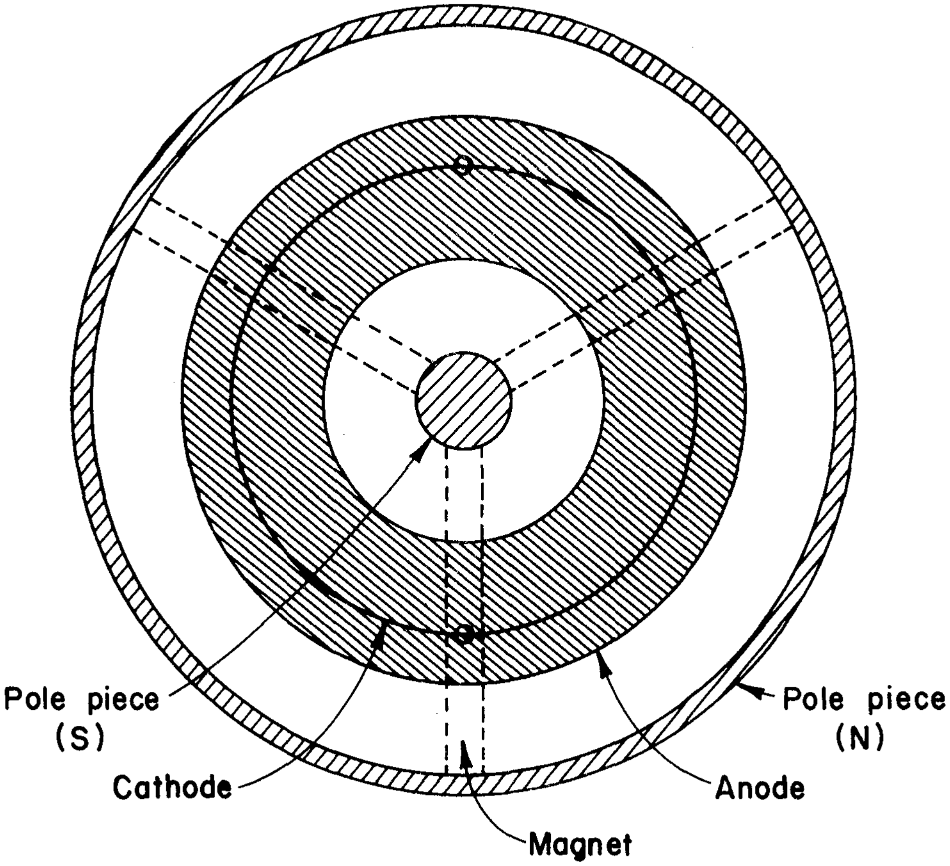

(a) End view.

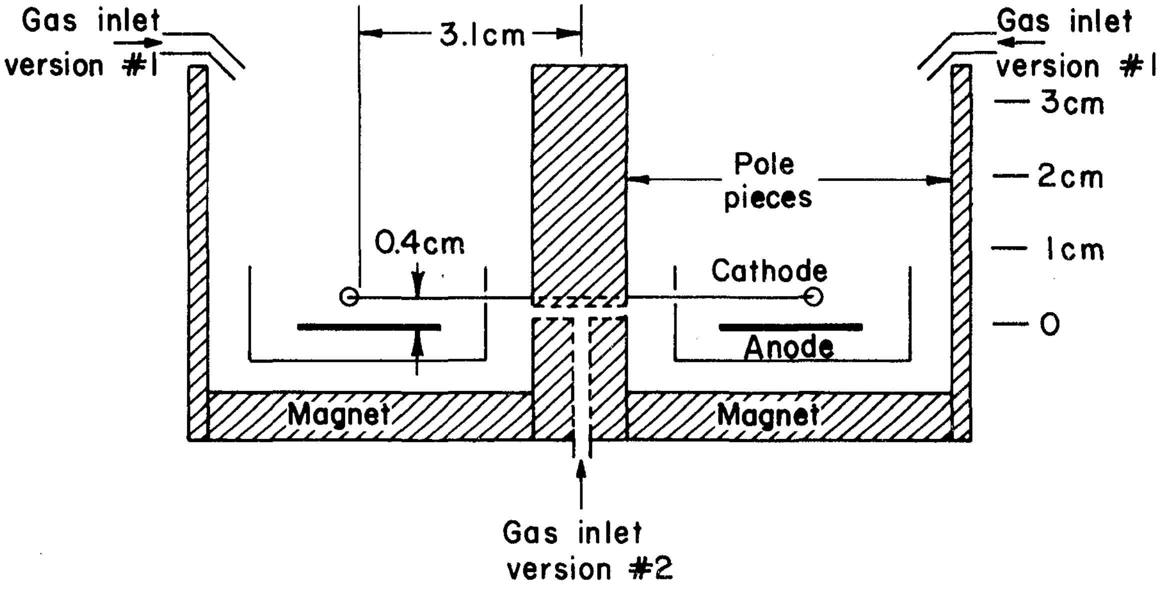

(b) Side view.

Fig. 4-2. Drawings of Hall-current thruster.

accelerator (the bottom of Fig. 4-2(b)). A nonmagnetic annular cup to contain the discharge surrounds the anode. Two refractory metal cathodes were used, one located as indicated in Fig. 4-2(b) near the anode, the other a neutralizer cathode at the exit plane of the acceleration channel (not shown in Fig. 4-2(b)). The cathode close to the anode was fabricated of 0.51 mm diameter W, with a nominal emission of 1 A for a 17.5 A heating current. (The two semicircular segments of this cathode were effectively in parallel, resulting in a heater power supply current of 35 A.) The neutralizer cathode was a single strand of 0.25 mm diameter Ta wire, with a nominal emission of 1 A for a 5 A heating current.

The magnetic integral in a radial-field configuration varies with the radius at which the integration is performed. Still, the concept of the magnetic integral is a useful one for general design considerations. At the radius of the cathode, the magnetic integral between the anode and cathode (see Fig. 4-2(b)) was 20×10^{-6} T-m (20 Gauss-cm). This value was low compared to the typical $50\text{-}60 \times 10^{-6}$ T-m between anode and cathode in an electron-bombardment discharge chamber.

The original configuration that was fabricated used six permanent magnets instead of three, and had the cathode farther from the anode, with a magnetic integral more typical of electron-bombardment thrusters between the anode and cathode. This configuration proved almost impossible to operate in the <100 V range that was felt to be of interest. Subsequent tests indicated that discharges could be started and maintained with the reduced number of magnets and relocated cathode.

The gas flow was originally introduced through two tubes on opposite sides of the thruster, resulting in a nonuniform pressure distribution. The thruster was then modified to permit the gas flow to be introduced through the central pole piece. When the gas flow was introduced in this latter manner, rings of insulator were used to force the gas flow through evenly distributed small holes in the inner cylinder of the annular cup. Also not shown in Fig. 4-2 are the insulators used to support anode and annular cup, as well as to block the upstream end of the thruster and shield the Alnico V magnets from the heat.

Magnetic field. The magnetic field of the operating Hall-current thruster has two major components to the local field strength. First there is the radial magnetic field produced by the magnets and the cylindrical pole pieces. The strength of this component is indicated in Fig. 4-3, which shows contours of constant magnetic field strength at the axial location of the cathode, and in Fig. 4-4, which shows the mean axial variation of magnetic field strength. The second component is the contribution from the cathode heater current. To avoid the problem of measuring the magnetic field close to a current-carrying cathode, the cathode field component was calculated. The combination of these two fields is indicated in Fig. 4-5, with the axial location 1 mm upstream from the cathode. The combination is also shown in Figs. 4-6 through 4-8 for the axial variation at different radii. The cathode heater current was 17.5 A for Figs. 4-5 through 4-8.

The cathode heater current clearly has a significant effect on the total magnetic field distribution. On the one side of the thruster, the 17.5 A heater current drops the anode-cathode magnetic integral to 14×10^{-6} T-m, and on the other side increases it to 34×10^{-6} T-m, both compared to 20×10^{-6} T-m without a cathode heater current.

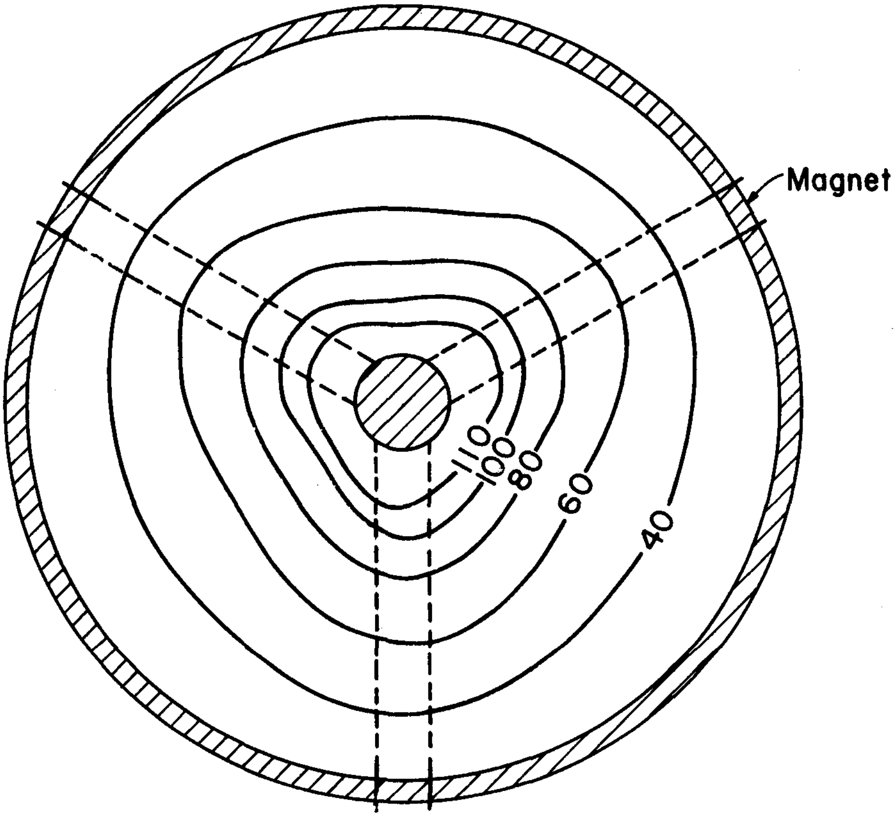

Fig. 4-3. Contours of constant magnetic field strength at the axial location of the cathode. (Field strength is indicated in Gauss. Cathode not operating.)

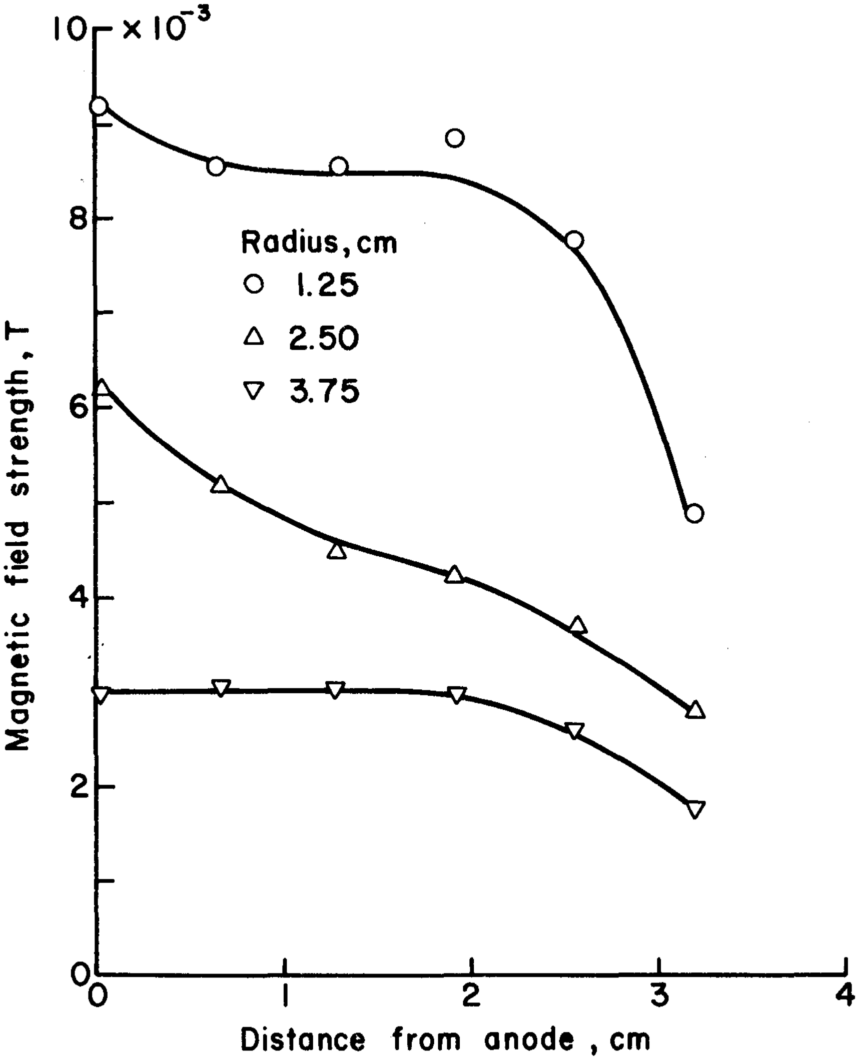

Fig. 4-4. Mean axial variation of magnetic field strength at different radii.

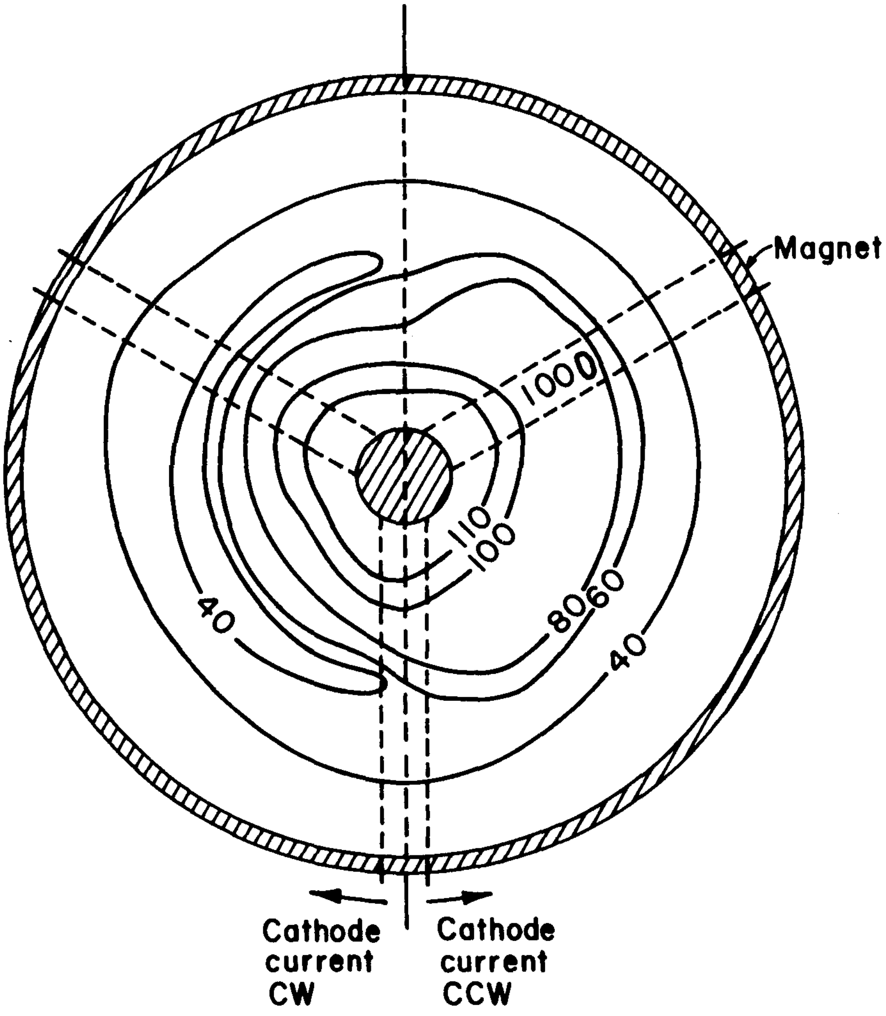

Fig. 4-5. Contours of constant magnetic field strength at an axial position 1 mm upstream of the cathode. (Constant field of Fig. 4-3 plus the calculated effect of 17.5 A current through each branch of the cathode.)

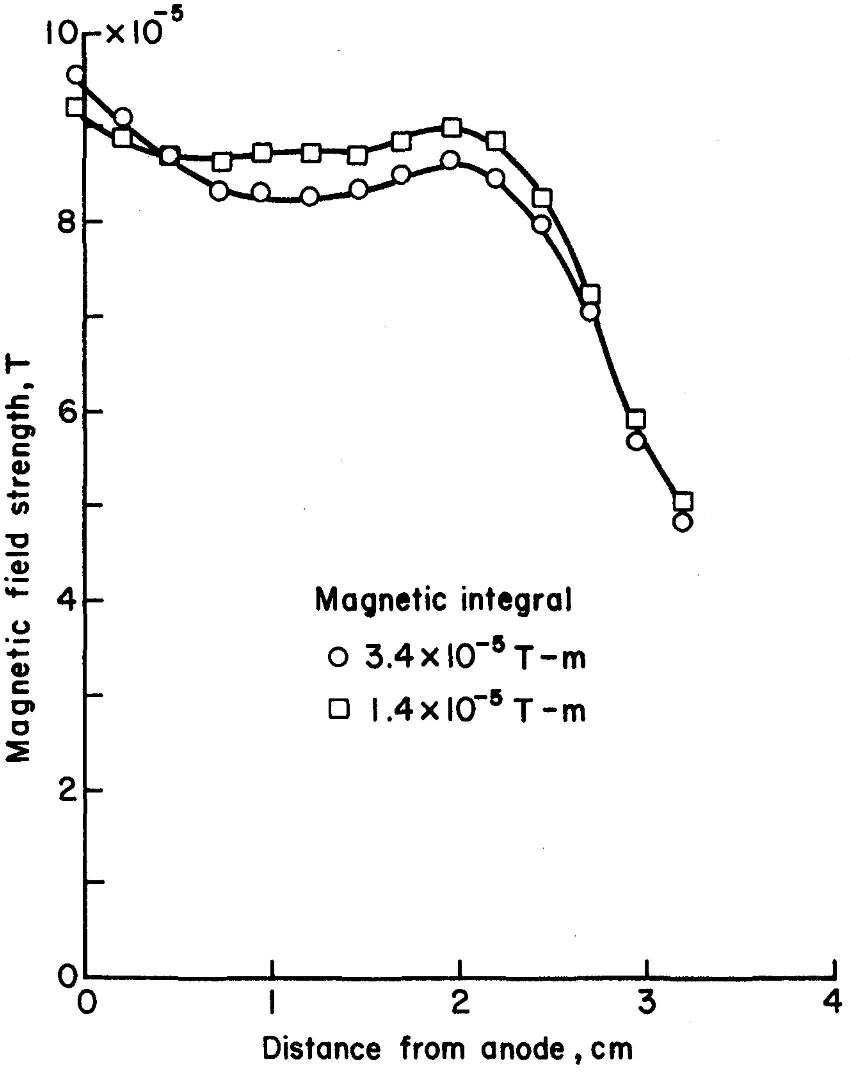

Fig. 4-6. Mean axial magnetic field at a radius of 2.3 cm. (Constant field plus effect of ±17.5 A cathode current.)

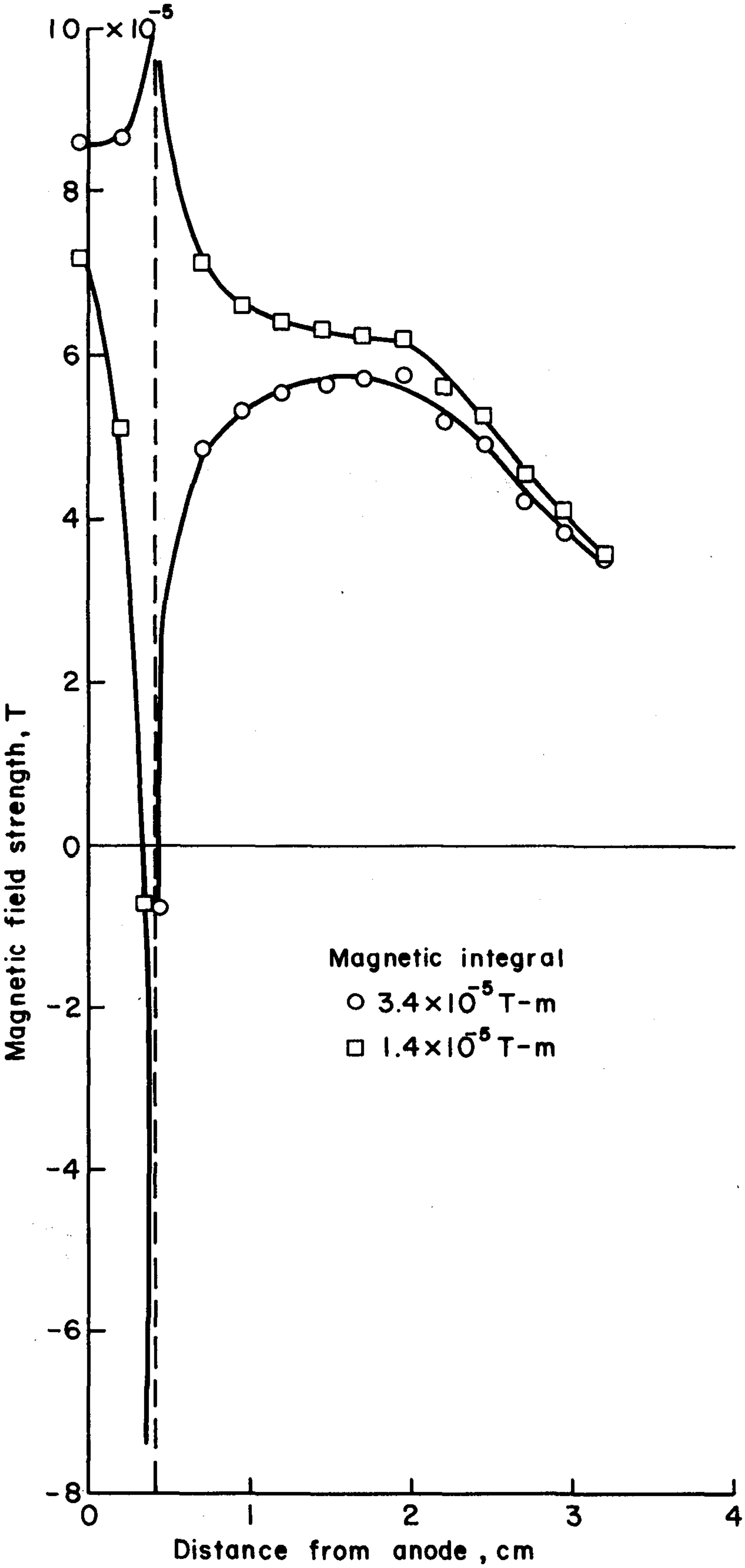

Fig. 4-7. Mean axial magnetic field at cathode radius, 3.1 cm. (Constant field plus effect of ±17.5 A cathode current.)

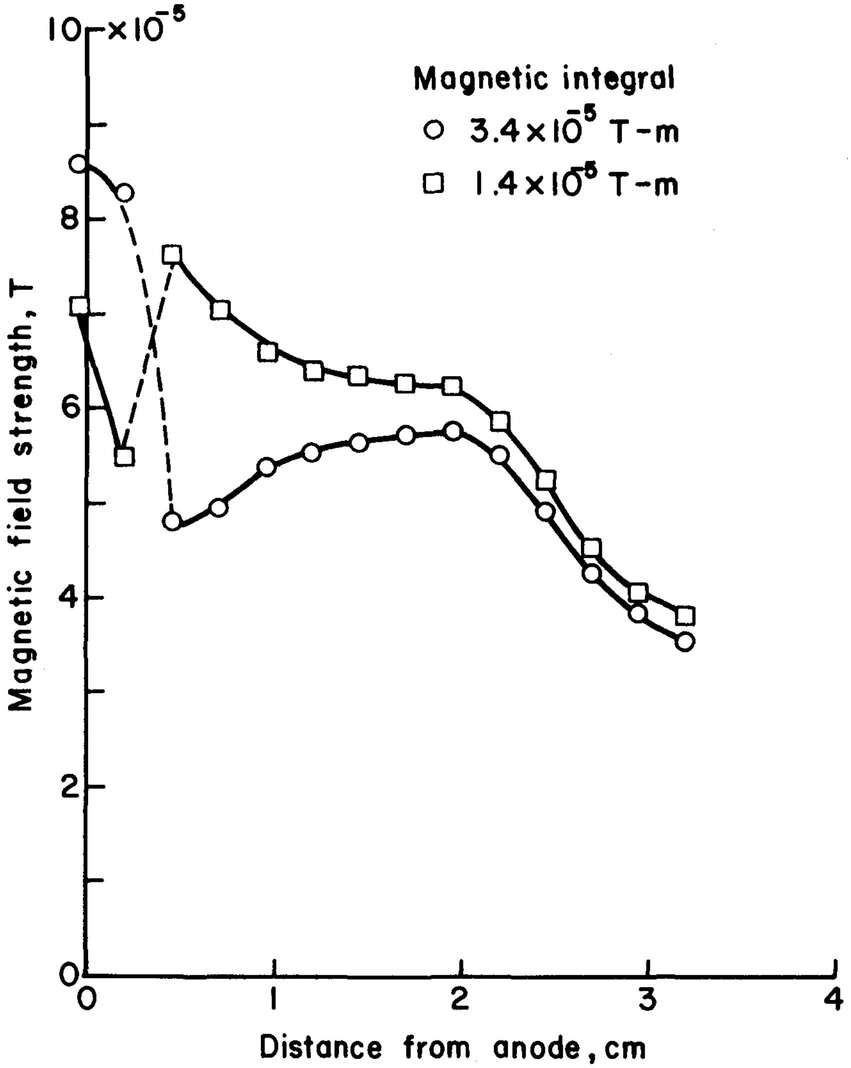

Fig. 4-8. Mean axial magnetic field at radius of 3.2 cm. (Constant field plus effect of ±17.5 A cathode current.)

This significance of the heater current appears to be a sharp distinction from electron-bombardment thruster experience. In the latter, the background field near a refractory cathode is normally quite small. Inasmuch as the cathode heater current is not enough to result in localized containment of the emitted electrons, the effect of the heater current on discharge-chamber performance is usually not significant.

Operation. The Hall-current thruster design tested can be operated in three different modes: main cathode only, neutralizer cathode only, or both cathodes together. The electrical circuitry for all three modes is indicated in Fig. 4-9. The Ar introduction could also be changed as indicated in Fig. 4-2(b). Unless otherwise noted, all operation was with the uniform Ar feed. For the flows of Ar of about 100-1000 mA-equiv, the vacuum chamber pressure was in the range of $1\text{-}10 \times 10^{-4}$ Torr. (The relation between flow rate and pressure was close to linear.)

Results and Discussion

Operating range. The voltages required to start and to maintain the discharge were investigated with both Ar feeds. The results of these tests are shown in Fig. 4-10. As discussed in the section on the magnetic field, the magnetic field strength was reduced from the initial value to facilitate operation. The reduced field strength used for the operating range tests of Fig. 4-10 (indicated in Figs. 4-3 through 4-8) thus represent a compromise between the low value required for discharge operation and the high value desired to minimize the electron backflow in the acceleration region.

The results of Fig. 4-10 were obtained with only the main cathode heated to emission temperature, using a 17.5 A heating current. Up to

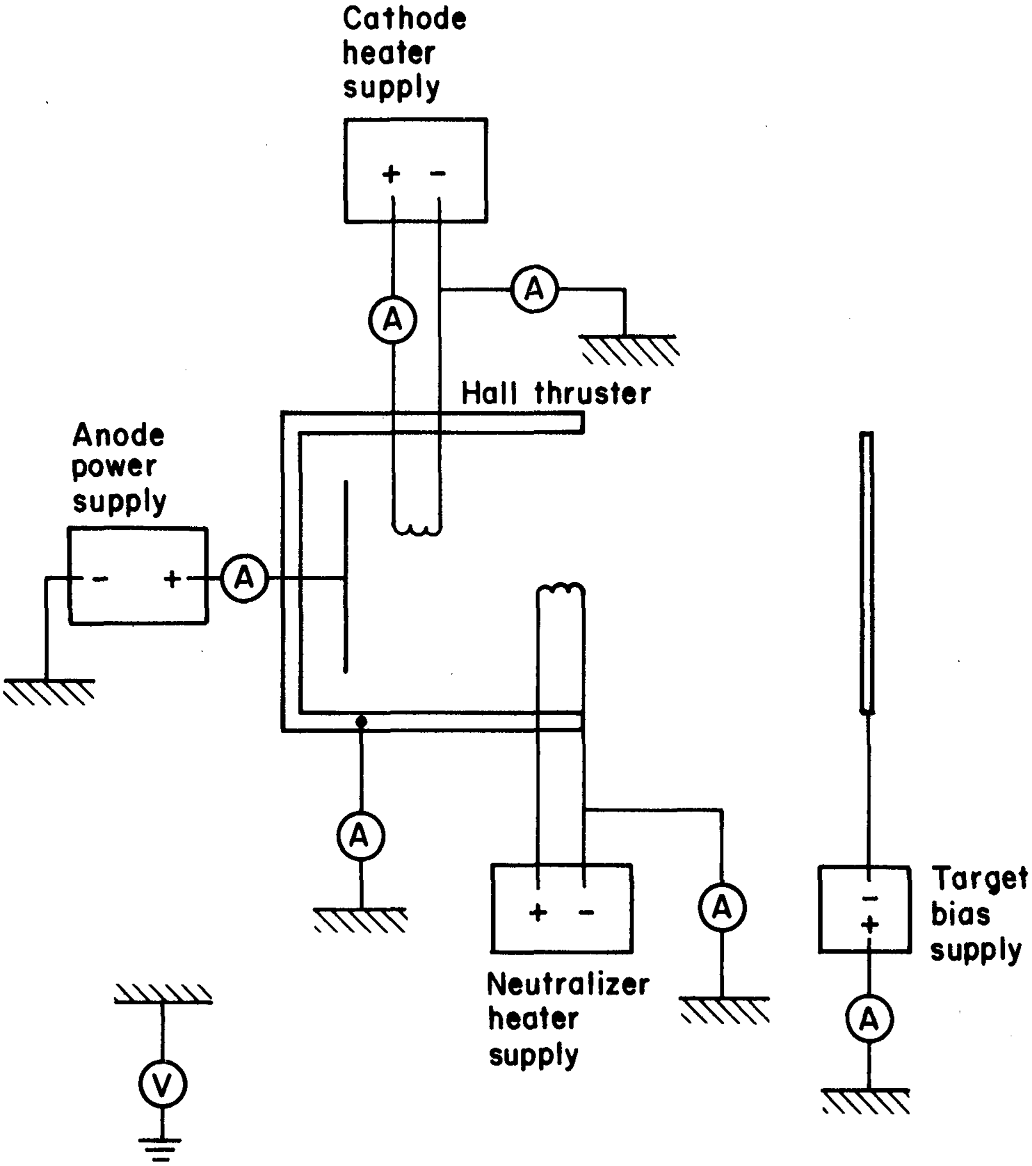

Fig. 4-9. Electrical power and instrumentation schematic.

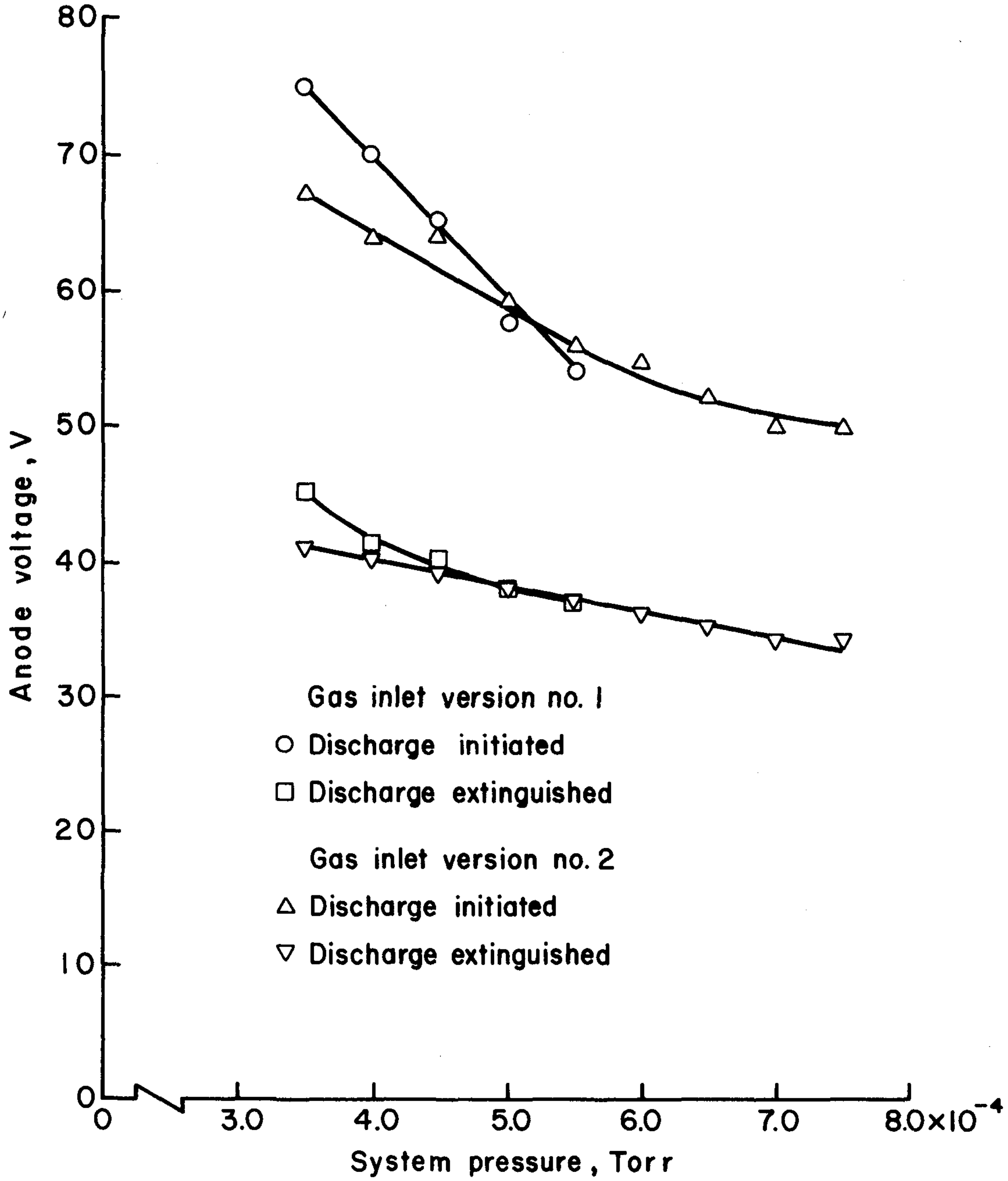

Fig. 4-10. Anode voltage required to start and maintain a discharge. (No neutralizer emission.)

an 8 V increase in starting voltage was observed with the nonuniform Ar feed, while the minimum voltage for the same feed was increased up to 4 V.

The effect of the neutralizer cathode on the operating range is indicated in Fig. 4-11 for uniform Ar feed. It was found that with a neutralizer emission current of about 1 A (corresponding to 5 A heater current), the neutralizer emission caused the minimum operating voltage to approach the starting voltage over most of the pressure range investigated.

The interaction between the two cathodes indicated in Fig. 4-11 was typical of this investigation. Simply increasing the neutralizer emission at a fixed main cathode emission usually resulted in the discharge being extinguished. On the other hand, if the main cathode emission were reduced as the neutralizer emission was increased, it was occasionally possible to continue operation.

Operation with the neutralizer cathode only was possible at higher facility pressures and voltages, as indicated in Fig. 4-12. The operating range shown does not include starting the discharge. The discharge was started with the main cathode, then the emission was gradually shifted over to the neutralizer cathode. The crosshatched region in Fig. 4-12 is, therefore, simply the operating range for the neutralizer cathode after the discharge was started using the main cathode. The pressure range of 6-9 × 10^{-4} Torr corresponded to Ar flows of about 600-900 mA-equiv. The minimum pressure of 6.5 × 10^{-4} Torr gave operation at only 94 V, which (in eV) is close to the electron energy for maximum ionization cross section of Ar.

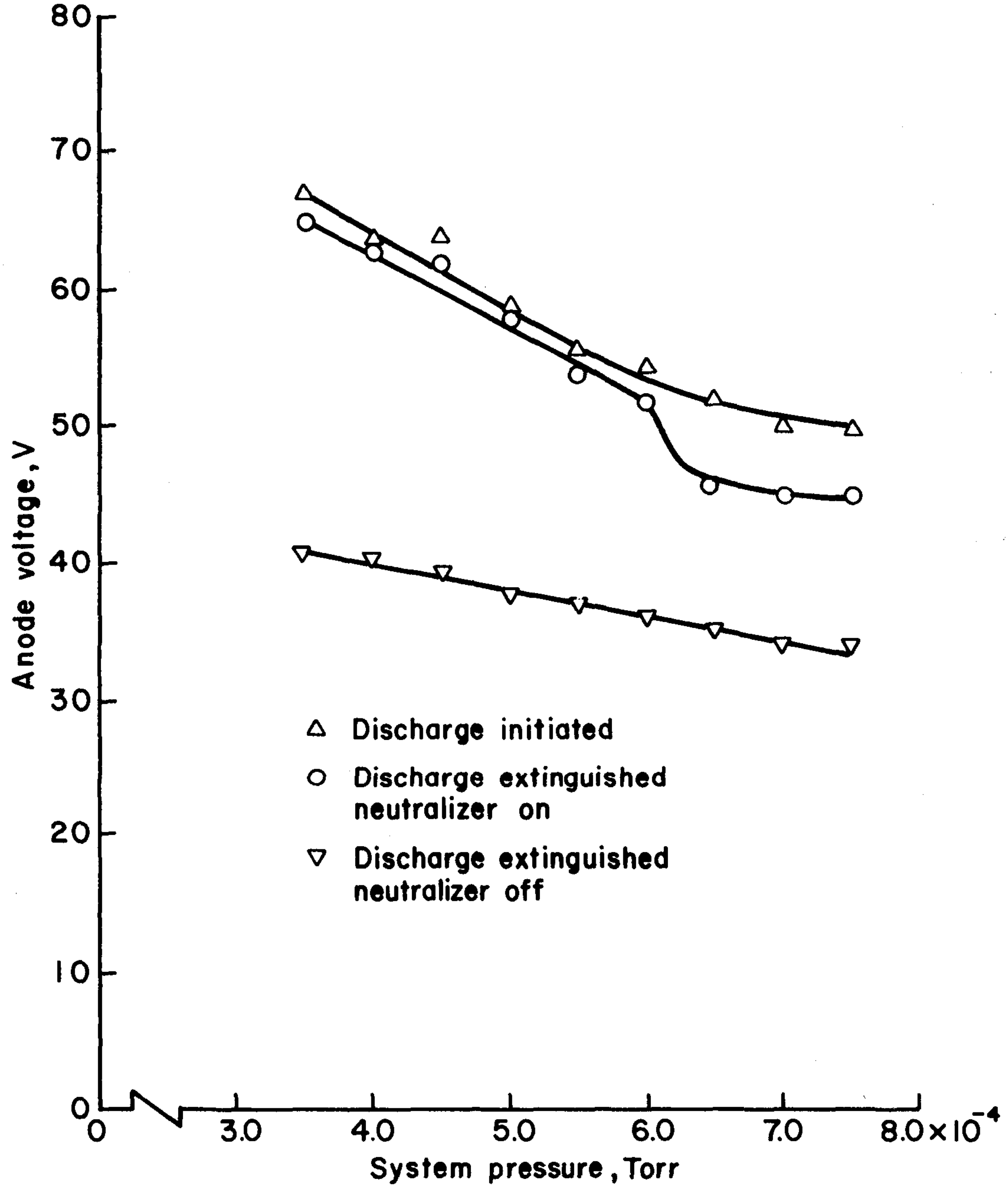

Fig. 4-11. Effect of neutralizer operation on operating voltage range with uniform gas flow. (When on, neutralizer emission was 1 A.)

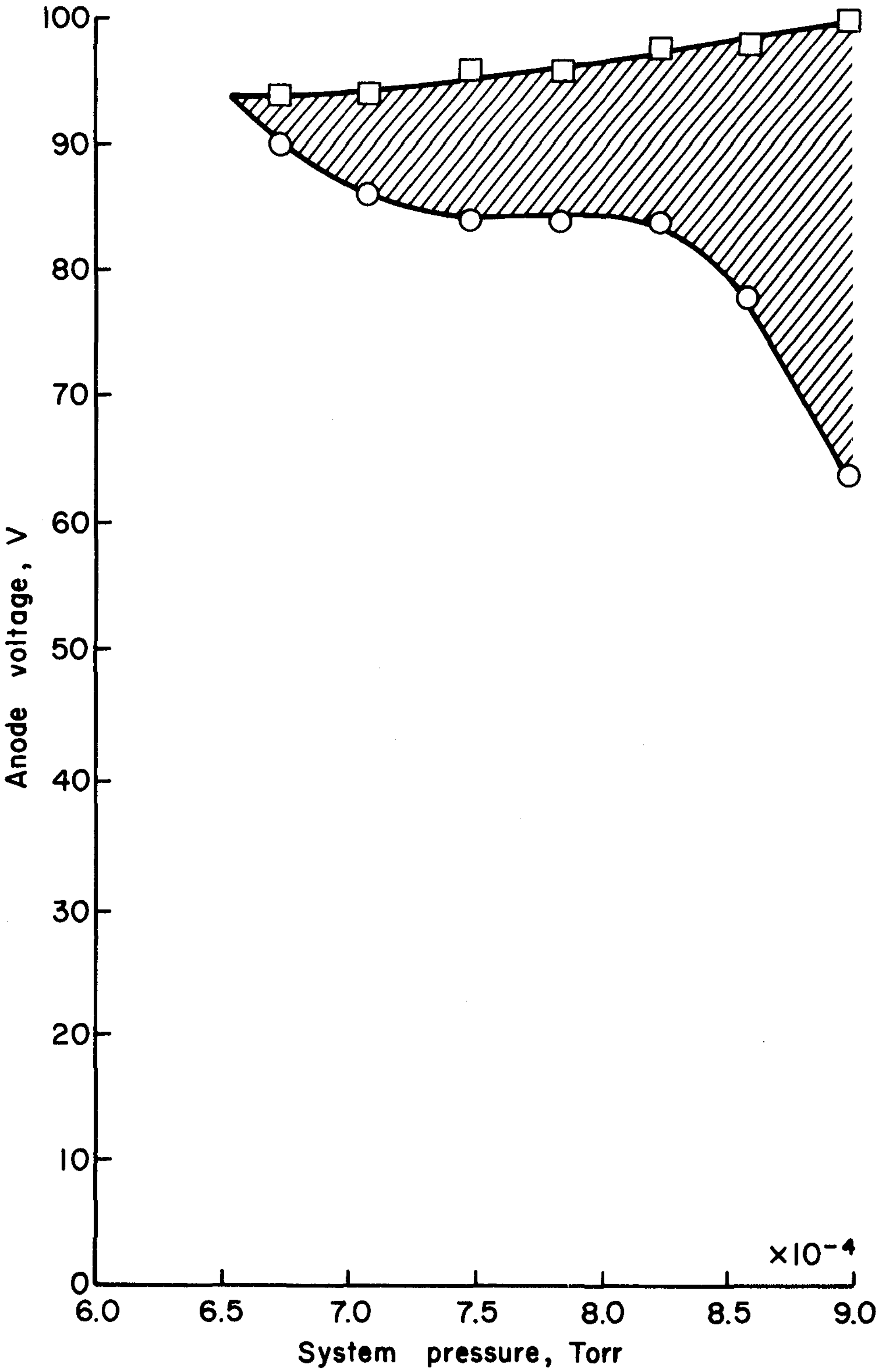

Fig. 4-12. Range of operation using only the neutralizer cathode. (Neutralizer emission, 1.5 A.)

Plasma properties. A Langmuir probe was used to measure the plasma properties in the channel of the Hall-current thruster. The plasma properties were all evaluated at a radius of 3.2 cm, which is 1 mm more than the cathode radius. The operating conditions were: Ar flow, 772.5 mA-equiv; pressure, 4×10^{-4} Torr (this higher flow-to-pressure ratio was caused by a change in the pumping system); main cathode heated to emission of 1 A; neutralizer cathode heated to an emission of 0.6 A; anode set at 70 V with a plasma discharge of 2.5 A.

Results obtained with the nonuniform gas flow are shown in Figs. 4-13 through 4-15. The two sides of the thruster are indicated by the two magnetic integral values. Although the flow was nonuniformly introduced through two tubes, the plasma probing was symmetrical with these two tubes. The differences for the two sides are thus believed to represent the results of the different magnetic fields on the two sides, and not due to a flow difference.

Both magnetic integrals in Fig. 4-13 indicate that the plasma potential outside the thruster is about 20 V less than anode potential, which is still about 50 V positive of the common potential near ground. It is clear that the magnetic field between the main cathode and neutralizer cathode is inadequate for voltage isolation. To be more specific, the reductions of field strength that were made to facilitate low voltage starting and operation resulted in too little field for acceleration purposes.

The plasma properties for uniform and nonuniform Ar flow are compared in Figs. 4-16 through 4-18 for the 34×10^{-6} T-m side of the thruster. All circumferential nonuniformities tend to reduce the voltage isolation capabilities of Hall-current channels. The added

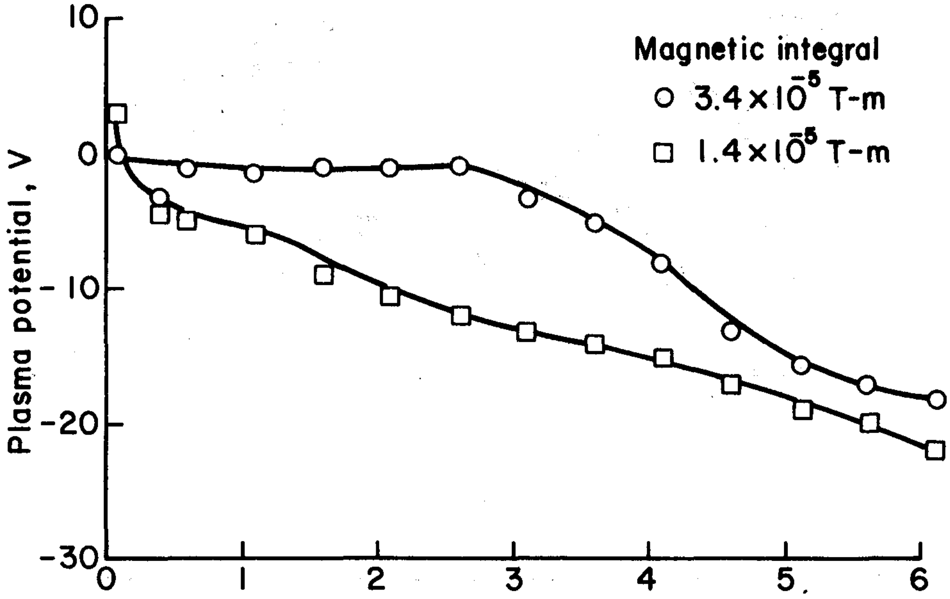

Fig. 4-13. Effect of cathode current (±17.5 A) on the axial variation of plasma potential.

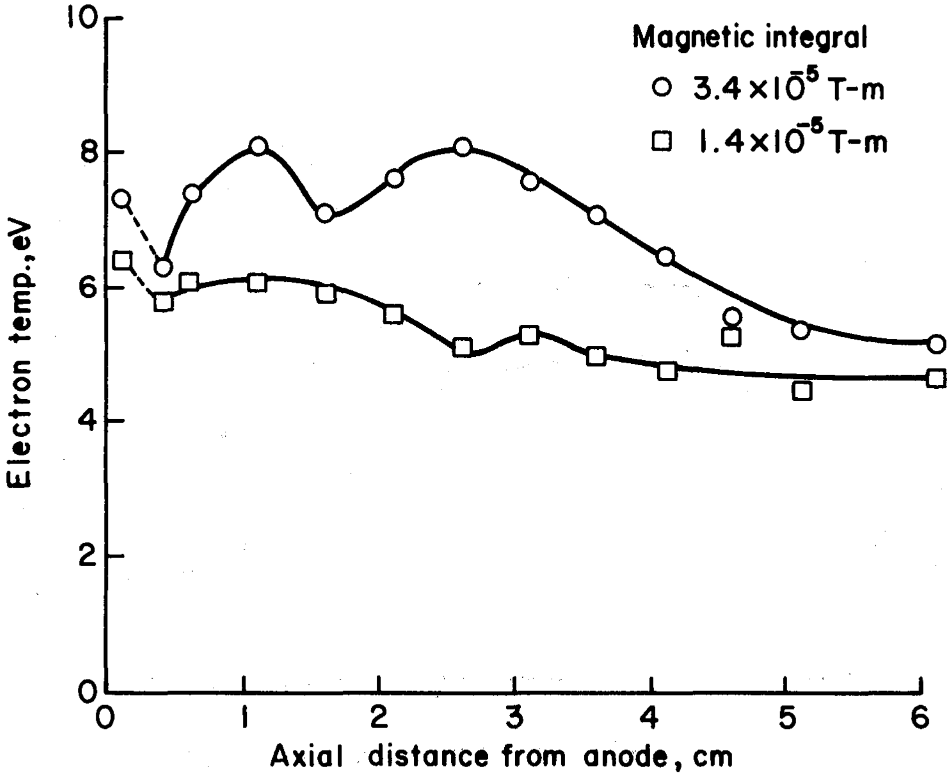

Fig. 4-14. Effect of cathode current (±17.5 A) on the axial variation of electron temperature.

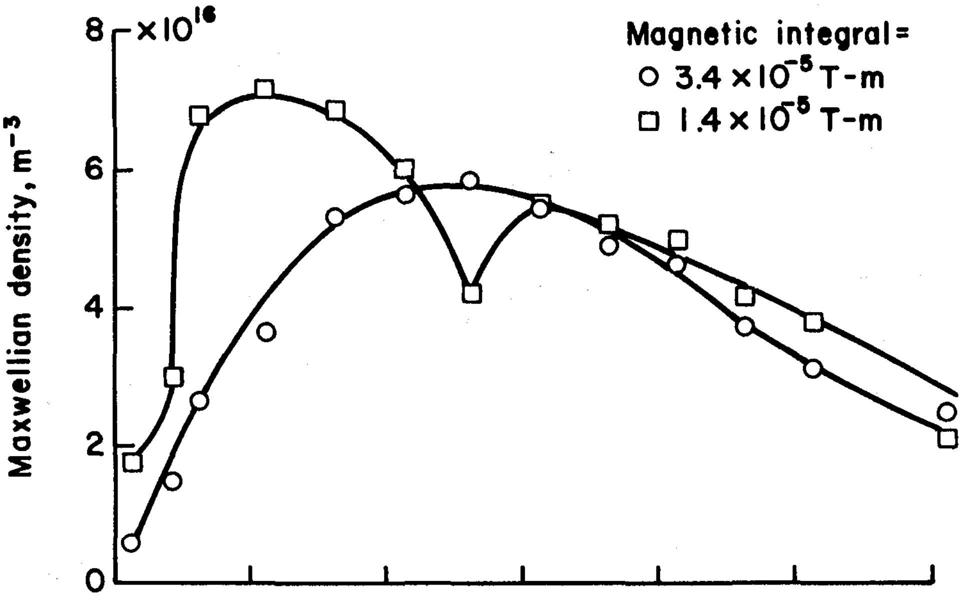

Fig. 4-15. Effect of cathode current (±17.5 A) on the axial variation of electron density.

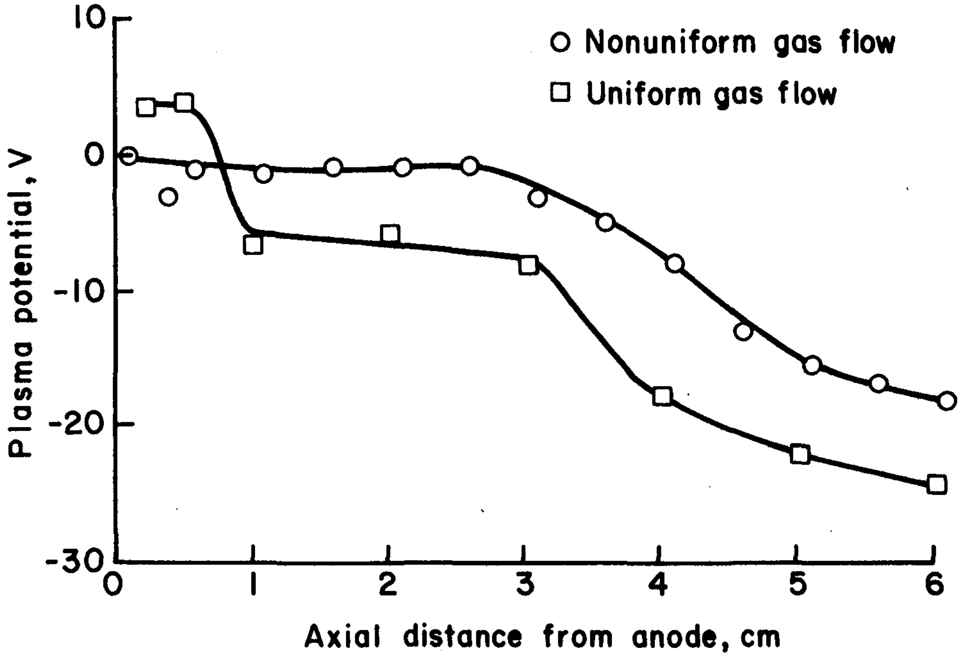

Fig. 4-16. Effect of gas flow uniformity on the axial variation of plasma potential.

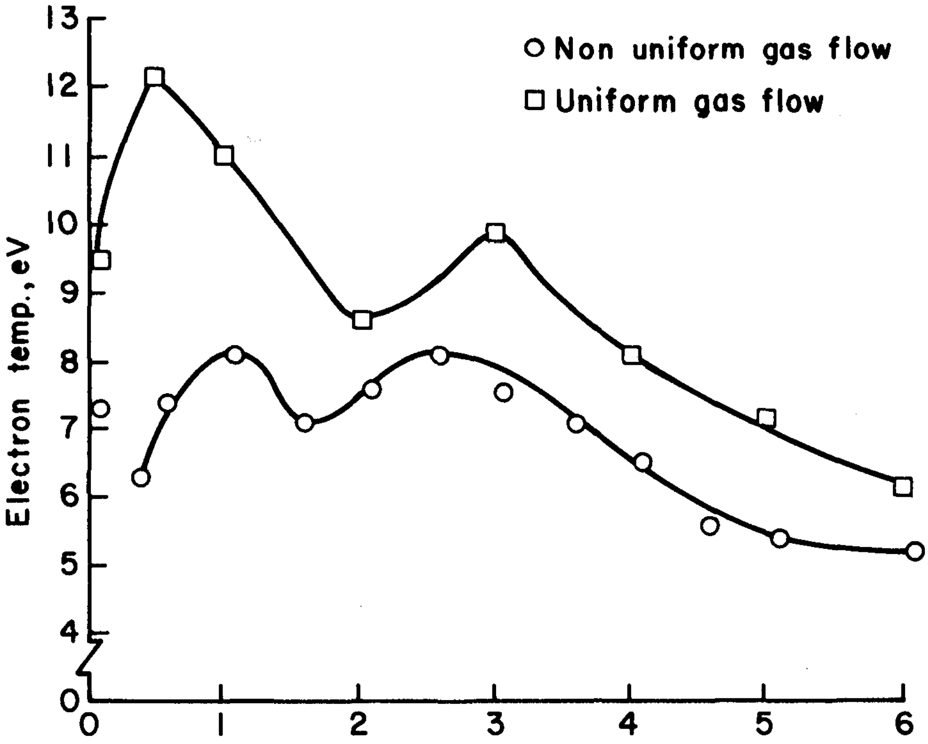

Fig. 4-17. Effect of gas flow uniformity on the axial variation of electron temperature.

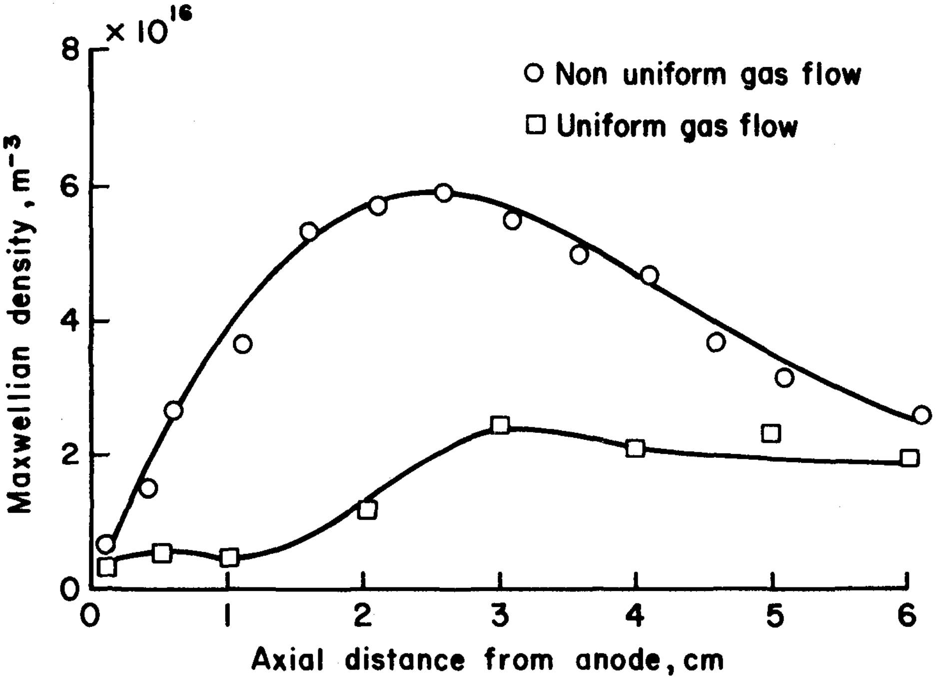

Fig. 4-18. Effect of gas flow uniformity on the axial variation of electron density.

uniformity of a uniform gas flow might be expected to improve voltage isolation capability, which it does by 5-6 V. But the plasma potential outside the thruster is still about 45 V above the common potential.

Conclusions

An experimental Hall-current thruster was tested with refractory metal cathodes. The magnetic field was reduced from the initial design to facilitate starting and operation at low voltages (<100 V). Although various operating modes were possible with the main and neutralizer cathodes, the voltage isolation capability of the acceleration channel was severely limited at the reduced field used. Circumferential variations are always detrimental for isolation capability, and a small improvement was noted when uniform Ar flow was used to replace a more nonuniform flow from only two tubes.

The use of refractory metal cathodes resulted in serious circumferential variations in the magnetic field, which resulted in corresponding variations in plasma properties. Some of the limited voltage isolation capability observed was probably also due to the adverse affects of the refractory cathode on circumferential uniformity.

As a major conclusion, then, the heating current for a refractory cathode can adversely affect circumferential uniformity in a Hall-current thruster.

As another major conclusion, the low field strength used to facilitate starting and operation resulted in inadequate voltage isolation for acceleration.

One approach for avoiding the field-strength compromise used herein is to have a "discharge chamber" upstream of the acceleration region, so that the ion generation can take place with only moderate field strengths in this region, while high field strengths are still available for acceleration. This is the general approach used in Hall-current accelerators in the U.S.S.R.[5]

Another approach might be to use more sophisticated approaches to electron diffusion in the "discharge chamber" region. Electron-bombardment thrusters have discharge problems when the magnetic integral between the anode and cathode becomes too large. This problem is aggravated when the anode area is only a small fraction of the total wall area for the discharge chamber.[6] It is suspected both of these factors are involved in field-strength problems encountered in this investigation. Inasmuch as the diffusion of electrons to the anode is the common limit when too high an integral or too small an anode area is used, alternate escape mechanisms for electrons may effectively solve these problems.

References

1. Staff of NASA Lewis Research Center, "30-cm Ion Thrust Subsystem Design Manual," NASA Tech. Mem. TM-79191, June 1979.

2. H. R. Kaufman, "Performance of Large Inert-Gas Thrusters," AIAA Paper No. 81-0720, April 1981. (A closely related paper is H. R. Kaufman and R. S. Robinson, "Large Inert-Gas Thrusters," AIAA Paper No. 81-1540, July 1981.)

3. M. C. Ellis, Jr., "Survey of Plasma Accelerator Research," in Proc. NASA - University Conference on the Science and Technology of Space Exploration - Vol. 2, NASA, Washington, D.C., pp. 361-381, Nov. 1962.

4. G. S. Janes and R. S. Lowder, "Anomalous Electron Diffusion and Ion Acceleration in a Low-Density Plasma," Phys. Fluids, Vol. 9, pp. 1115-1123, June 1966.

5. Papers of IV All-Union Conf. on Plasma Accelerators and Ion Injectors, Moscow, 1979 (in Russian).

6. H. R. Kaufman and R. S. Robinson, "Ion Source Design for Industrial Application," AIAA Paper No. 81-0668, Apr. 1981. (Also NASA Contr. Rep. CR-165334, Jan. 1981.

V. THEORY OF ION ACCELERATION WITH CLOSED ELECTRON DRIFT

A class of ion accelerators, called Hall-current accelerators in the U.S., use the electric field generated by electrons diffusing through a magnetic field to accelerate ions. To avoid large electron sources and sinks due to $\vec{E} \times \vec{H}$ drift, the acceleration channels have closed drift paths, usually annular in shape. A theory is developed in this section for ion acceleration with closed electron drift paths.

The major assumptions in this theory are: (1) the radial and circumferential variations in properties are small, so that the time-averaged properties vary only with x, the acceleration direction; (2) the ion current density is constant throughout the acceleration region; and (3) the electron current density is constant throughout this region. Assumptions (2) and (3) imply (with energy conservation for ions) a constant-area flow channel, and localized ion generation at the upstream end of the acceleration channel. In practice, constant ion current density usually also means a channel of uniform radius and length. Using an integral approach to electron diffusion that was developed previously,[1] it is not necessary to make assumptions regarding the detailed distribution of magnetic field intensity.

Differential Diffusion Equation

Assuming Bohm diffusion for both the potential and density gradient terms, the equation governing electron diffusion in the upstream direction is

$$j_e = \frac{en}{16B}\frac{dV}{dx} - \frac{eT}{16B}\frac{dn}{dx}, \tag{5-1}$$

where j_e is the electron current (opposite to conventional current) in A/m^2, e is the absolute electronic charge in C, n is the electron density in m^{-3}, V is the plasma potential in V, T is the electron temperature in eV, B is the magnetic field in T, and x is the distance in m in the direction of the electron diffusion measured from the exhaust plane. Note that this equation is concerned only with the electron motion opposite to the applied electric field, and not the circulating or Hall current.

If ion production and losses are both negligible in the acceleration region, and the ion acceleration is restricted to the x direction, then the ion density can be expressed as

$$n = n_o V_o^{1/2}/(V_o - V)^{1/2} , \qquad (5\text{-}2)$$

where n_o is the ion density after acceleration and V_o is the potential through which the ions are accelerated. The plasma potential V is defined as zero at the exhaust plane of the accelerator. From the quasi-neutrality assumption for a plasma, Eq. (5-2) also gives the electron density.

Zero Electron Temperature

The simplest case to calculate is the one in which electron temperature is negligible throughout the acceleration region. Substituting Eq. (5-2) in Eq. (5-1) and rearranging the results,

$$16Bj_e dx = en_o V_o^{1/2} dV/(V_o - V)^{1/2} . \qquad (5\text{-}3)$$

With j_e assumed a constant throughout the acceleration region, Eq. (5-3) can be integrated from the exhaust plane ($V = 0$) to obtain*

$$16 j_e \int B dx = e n_o V_o \{2 - 2(1 - V/V_o)^{1/2}\} . \tag{5-4}$$

To facilitate comparison with other solutions, it is convenient to rearrange terms:

$$j \int B dx / e n_o V_o = \{1 - (1 - V/V_o)^{1/2}\}/8 . \tag{5-5}$$

For integration over the entire acceleration region, to $V = V_o$, the right side of Eq. (5-5) becomes 1/8.

In practice, the acceleration process described by Eq. (5-5) might result from the continual collection of high energy electrons by, and emission of low energy electrons from, the walls of the acceleration channel. The electron temperature might also be maintained at a low value by excitations of ions and neutrals. In the latter case, however, one might also expect the assumption of negligible ionization in the acceleration region to be violated.

Zero Initial Electron Temperature

As another fairly simple case, the electron temperature can again be assumed zero at the exhaust plane, but then to increase as the electrons pass through the acceleration region. If energy is conserved, one would expect the electron temperature to be

---

*The integral of $\int B dx$ is assumed to have B normal to dx for the problem herein. If this orientation is not used, a cross product must be used in the integration, i.e., $\int \vec{B} \times d\vec{x}$.

$$T = 2V/3 \ . \tag{5-6}$$

That is, the energy gained in passing through a potential difference of V results in a rms electron temperature of 2V/3. Note that this approach ignores thermal conduction by the electron population. The assumed Bohm diffusion is believed to result from electron scattering by ion-plasma waves, which can be generated by much lower electron-ion drift velocities than electron-plasma waves. This electron scattering is usually orders of magnitude greater than the scattering due to "soft" or Coulomb collisions by other electrons. Yet the thermal conductivity of an electron population is a function mostly of these Coulomb collisions. The scattering collisions with ion-plasma waves tend to result in a much slower transfer of energy to and from the electron population. Ignoring thermal conduction by electrons thus appears to be consistent with the assumption of Bohm diffusion.

For a nonzero electron temperature, the second term of Eq. (5-1) becomes important. The expression for n, Eq. (5-2), can be differentiated to obtain

$$dn = n_o V_o^{1/2} dV/2(V_o - V)^{3/2} \ . \tag{5-7}$$

Substituting Eqs. (5-2), (5-6) and (5-7) into Eq. (5-1) and rearranging the results,

$$16Bj_e dx = en_o V_o^{1/2} \left(\frac{-dV}{(V_o - V)^{1/2}} + \frac{VdV}{3(V_o - V)^{3/2}} \right) . \tag{5-8}$$

Again assuming j_e a constant throughout the acceleration region, Eq. (5-8) can be integrated from the exhaust plane (V = 0) to obtain

$$j_e \int B dx / e n_o V = \{5 - 4(1 - V/V_o)^{1/2} - 1/(1 - V/V_o)^{1/2}\}/24 \ . \qquad (5\text{-}9)$$

This result is not as straightforward as Eq. (5-5). For example, integration of V to the limit of V_o results in an infinitely negative value for the right side of Eq. (5-9). To illustrate the problem in more detail, Eq. (5-9) is plotted in Fig. 5-1, together with Eq. (5-5) for comparison.

The values in Fig. 5-1 represent integrals from V = 0 to a particular value of V/V_o. For the integration limit of V/V_o much closer to zero than unity, the two approaches (Eqs. (5-5) and (5-9)) give very similar results. As the limit V/V_o is increased, the divergence between the two approaches becomes greater. Both Eq. (5-5) and Eq. (5-9) include electron diffusion from the potential gradient (first term in Eq. (5-1)). But only Eq. (5-9) has a diffusion in the opposite direction due to the increase in plasma density as potential increases. Note that the assumption of zero electron temperature for Eq. (5-5) results in no such opposing diffusion. Due to this opposing diffusion effect in Eq. (5-9), less additional magnetic field is required to offset an additional potential difference at the same current density. The effect is proportional to electron temperature, so the difference between the two solutions increases with V/V_o. (Note that from Eq. (5-6), T/V_o is proportional to V/V_o.)

At a $V/V_o = 3/4$, the opposing diffusion due to increasing plasma density exactly balances the diffusion due to potential gradient.

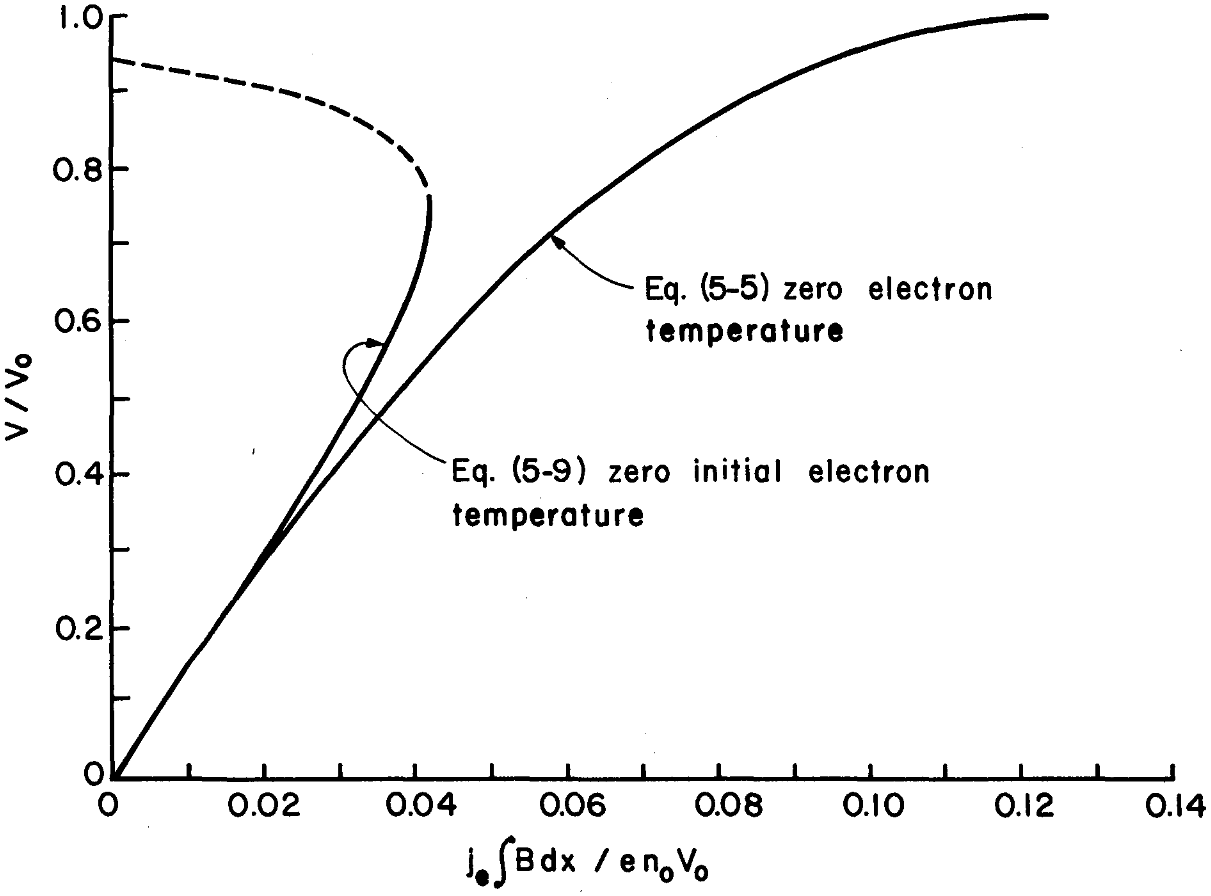

Fig. 5-1. Comparison of theoretical solutions for acceleration region in steady-state plasma thruster.

An incremental increase in V/V_o at this point thus requires no additional magnetic field to maintain a given value of current density. Beyond $V/V_o = 3/4$, the solutions become double valued, which is clearly unrealistic.

In the derivations of Eqs. (5-5) and (5-9), the diffusion processes were assumed to be continuous. That is, the finite sizes of electron orbits were not considered. The physical expectation for Eq. (5-9), then, is that the electrons would pass from $V/V_o = 3/4$ to $V/V_o = 1$ by means of a single, collision-free orbit. Using momentum considerations, the magnetic-field integral that can be crossed by this single orbit is

$$\int B dx = (2m_e/e)^{1/2}(2T^{1/2} + V_o^{1/2}/2) , \tag{5-10}$$

where T is the electron temperature in eV and the potential difference from beginning to end of the orbit is $V_o/4$. The rms velocity was used to calculate the contribution in Eq. (5-10) due to random electron energy. Having passed through a potential difference of $3V_o/4$, Eq. (5-6) indicates an electron temperature of $V_o/2$ at the start of the orbit for substitution in Eq. (5-10). With this substitution, together with the electron charge and mass, the magnetic integral crossed is

$$\int B dx = 6.45 \times 10^{-6} V_o^{1/2} . \tag{5-11}$$

The maximum value of abscissa in Fig. 5-1 (the start of the escape orbit) is

$$j_e \int B dx \,/ e n_o V_o = 0.0417 \,. \tag{5-12}$$

Substituting for electronic charge and solving for the magnetic integral,

$$\int B dx = 6.68 \times 10^{-21} \, n_o V_o / j_e \,. \tag{5-13}$$

It should be clear from Eqs. (5-11) and (5-13) that the escape orbit does not correspond to any particular fraction of the diffusion magnetic integral indicated in Fig. 5-1. It is, therefore, not possible to show the specific value of abscissa in Fig. 5-1 that is associated with the end of the escape orbit.

Constant Electron Temperature

The constant electron temperature case is the more general formulation of the zero electron temperature case. For a constant electron temperature, Eqs. (5-2) and (5-7) are substituted into Eq. (5-1),

$$16 B j_e dx = e n_o V_o^{1/2} \left(\frac{-dV}{(V_o - V)^{1/2}} + \frac{T dV}{2(V_o - V)^{3/2}} \right) . \tag{5-14}$$

Integration upstream from the exhaust plane, again assuming a constant j_e, yields

$$j_e \int B dx \,/ e n_o V_o = \left[1 + \frac{T}{2V_o} - (1 - V/V_o)^{1/2} - \frac{T/V_o}{2(1 - V/V_o)^{1/2}} \right] /8 \,. \tag{5-15}$$

The numerical results for Eq. (5-15) are similar to those from Eq. (5-9), in that results become double valued for V/V_o above a certain value. For Eq. (5-15), the limit for single-valued operation is

$$V/V_o = 1 - T/2V_o \ . \tag{5-16}$$

Values for Eq. (5-5) ($T/V_o = 0$) and Eq. (5-15) are shown in Table 5-1 and Fig. 5-2.

At first glance, the results shown in Table 5-1 and Fig. 5-2 indicate that a potential jump may be expected for acceleration with constant electron temperature, similar to that shown in Fig. 5-1 for zero initial electron temperature. If the ions are assumed to come from a plasma at the start of acceleration, they should have an initial velocity corresponding to ion acoustic velocity (the minimum velocity found by Bohm for a stable plasma sheath). With this initial velocity, the ions will have gone through just enough preacceleration to avoid the dashed portions of the curves shown in Fig. 5-2, hence avoid any sudden potential jump. In most practical applications, a constant electron temperature can, therefore, be expected to correspond to a continuous potential variation throughout the acceleration region.

Conserved Electron Energy

The conserved electron energy case is the more general formulation of the zero initial electron temperature case. The electron energy was assumed to be conserved in the derivation of Eq. (5-9), but the initial electron temperature in the exhaust plane, T_o, was assumed to be zero. The case of interest here is a nonzero initial temperature. The electron temperature as a function of local potential V then becomes

$$T = T_o + 2V/3 \ . \tag{5-17}$$

Substituting Eqs. (5-2), (5-7), and (5-17) into Eq. (5-1) yields

Table 5-1. Solutions for Constant Electron Temperatures. (Equations (5-5) and (5-15).) Values of $j_e \int B dx / e n_o V_o$.

$\frac{V}{V_o}$	$\frac{T}{V_o} = 0$	$\frac{T}{V_o} = 0.1$	$\frac{T}{V_o} = 0.2$	$\frac{T}{V_o} = 0.5$
0.0	0.0000	0.0000	0.0000	0.0000
0.1	0.0064	0.0061	0.0057	0.0047
0.2	0.0132	0.0125	0.0117	0.0095
0.3	0.0204	0.0192	0.0180	0.0143
0.4	0.0282	0.0264	0.0245	0.0191
0.5	0.0366	0.0340	0.0314	0.0237
0.6	0.0459	0.0423	0.0387	0.0278
0.7	0.0565	0.0514	0.0462	0.0307
0.75	0.0625	0.0562	0.0500	0.0312
0.8	0.0691	0.0614	0.0536	0.0305*
0.9	0.0855	0.0720	0.0584	0.0179*
0.09375	0.0938	0.0750	0.0562*	-0.0000*
0.95	0.0970	0.0753	0.0536*	-0.0115*
0.99	0.1125	0.0562*	0.0000*	-0.1688*
0.9975	0.1188	0.0000*	0.1188*	-0.3562*
1.0	0.1250	$-\infty$*	$-\infty$*	$-\infty$*

*These values are believed to be in a physically unrealistic operating regime.

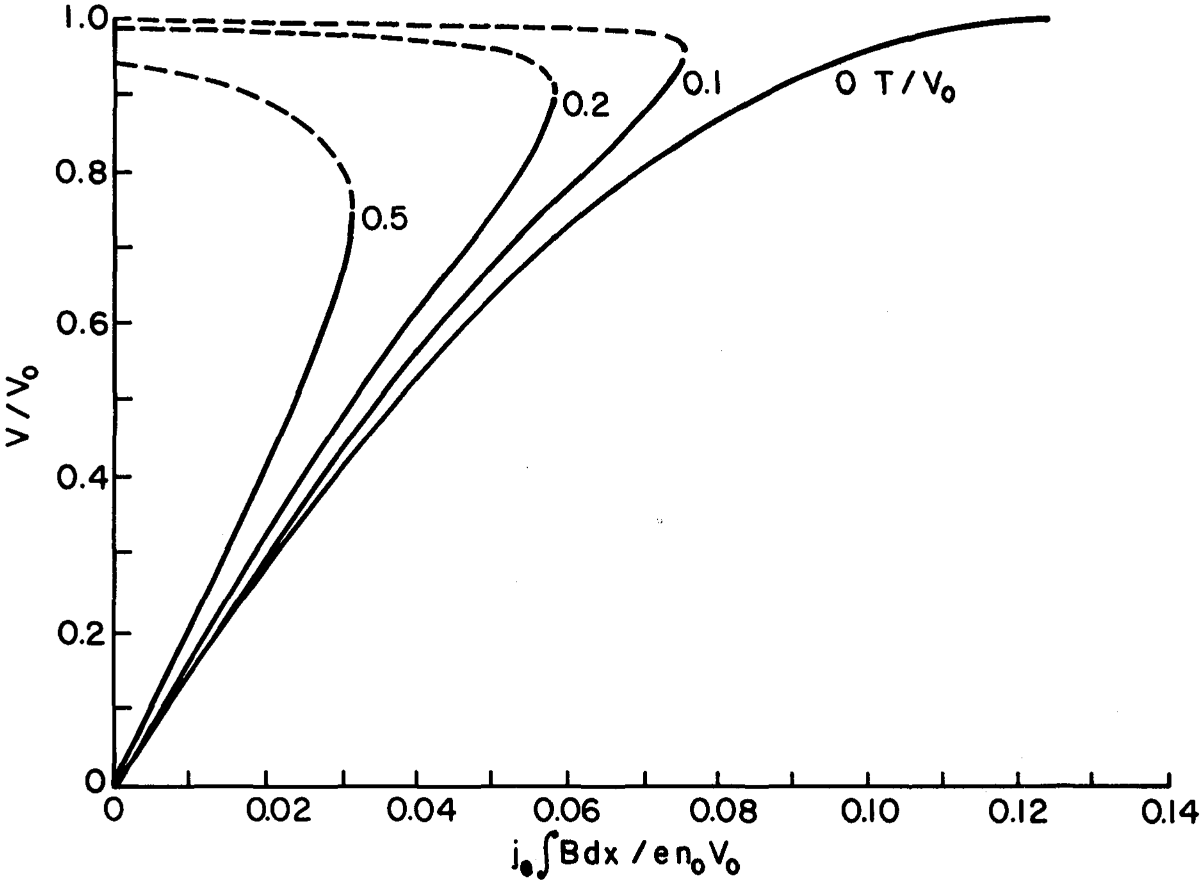

Fig. 5-2. Solutions for constant electron temperatures. (T/V_o in eV/V.)

$$16j_e B dx/en_o V_o^{1/2} = \frac{dV}{(V_o - V)^{1/2}} - \frac{T_o dV}{2(V_o - V)^{3/2}} - \frac{V dV}{3(V_o - V)^{3/2}} . \qquad (5\text{-}18)$$

Integrating from the exhaust plane then gives

$$j_e \int B dx \,/en_o V_o = \left(5 + \frac{3T_o}{2V_o} - 4(1 - V/V_o)^{1/2} - \frac{2 + 3T_o/V_o}{2(1 - V/V_o)^{1/2}}\right)/24 . \qquad (5\text{-}19)$$

The limit for single valued results is

$$V/V_o = (3/4)\ (1 - T_o/2V_o) . \qquad (5\text{-}20)$$

Values for Eq. (5-9) ($T_o/V_o = 0$) and Eq. (5-19) are shown in Table 5-2 and Fig. 5-3.

A finite initial electron temperature, T_o, is shown to result in the requirement for a potential jump, similar to that described in connection with Eq. (5-9) and Fig. 5-1. It is true that the magnitude of this jump decreases relative to V_o as T_o increases, when an initial velocity equal to the ion acoustic velocity is assumed. But the jump will still exist for all $T_o/V_o < 1$.

Comparison with Experimental Results

The value of the Bohm diffusion coefficient used herein is the one most widely used,[2,3]

$$D_B = T_e/16B , \qquad (5\text{-}21)$$

with T_e again in eV and B in T. Although this value has been used to correlate diffusion data for a wide range of experiments,[3] it should be

Table 5-2. Solutions for Conserved Electron Energy. (Equations (5-9) and (5-19).) Values of $j_e \int B dx / e n_o V_o$.

$\frac{V}{V_o}$	$\frac{T_o}{V_o} = 0$	$\frac{T_o}{V_o} = 0.1$	$\frac{T_o}{V_o} = 0.2$	$\frac{T_o}{V_o} = 0.5$
0	0.0000	0.0000	0.0000	0.0000
0.1	0.0063	0.0060	0.0056	0.0046
0.2	0.0127	0.0119	0.0112	0.0090
0.3	0.0191	0.0179	0.0166	0.0130
0.4	0.0254	0.0236	0.0218	0.0163
0.5	0.0316	0.0290	0.0264	0.0186
0.05625	0.0351	0.0319	0.0287	0.0191
0.6	0.0370	0.0334	0.0298	0.0189[*]
0.675	0.0402	0.0355	0.0308	0.0167[*]
0.7	0.0410	0.0358	0.0307[*]	0.0152[*]
0.7125	0.0413	0.0359	0.0304[*]	0.0142[*]
0.75	0.0417	0.0354[*]	0.0296[*]	0.0104[*]
0.8	0.0406[*]	0.0329[*]	0.0252[*]	0.0020[*]
0.8086	0.0402[*]	0.0321[*]	0.0241[*]	0.0000[*]
0.8944	0.0260[*]	0.0130[*]	0.0000[*]	-0.0389[*]
0.9	0.0239[*]	0.0104[*]	0.0032[*]	-0.0437[*]
0.9173	0.0175[*]	0.0000[*]	-0.0155[*]	-0.0620[*]
0.9375	0.0000[*]	-0.0188[*]	-0.0375[*]	-0.0938[*]
1.0000	$-\infty$[*]	$-\infty$[*]	$-\infty$[*]	$-\infty$[*]

[*] These values are believed to be in a physically unrealistic operating regime.

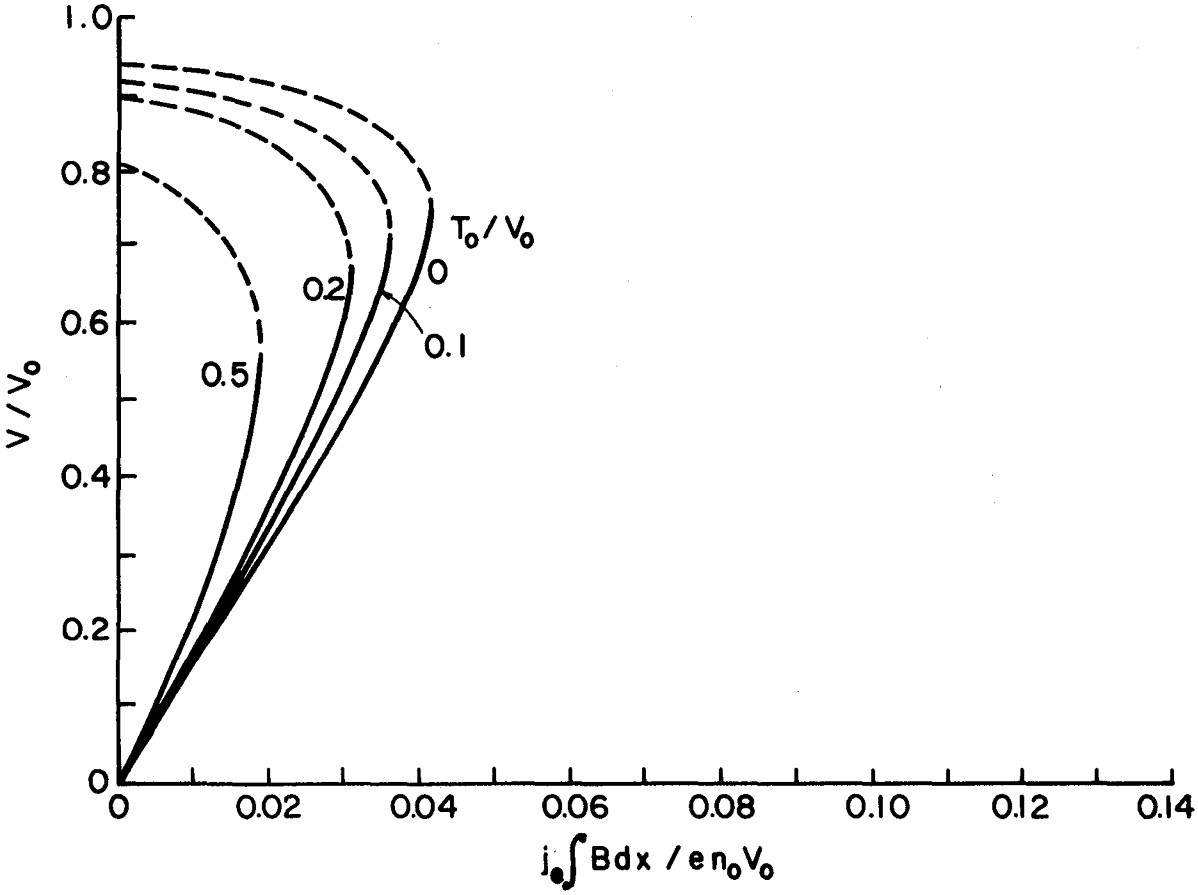

Fig. 5-3. Solutions for conserved electron energy and various exhaust-plane electron temperatures. (T_o/V_o in eV/V.)

kept in mind that it is only a semiempirical approximation and there is considerable data scatter. Perhaps more important, anomalous diffusion has been found to follow 1/B relationships in a wide variety of tests. Further, if one accepts a 1/B relationship proportional to Eq. (5-21), the results of Eqs. (5-15) and (5-19) should be expected to follow as qualitative consequences.

The constant-electron-temperature solution, Eq. (5-15), does not depart significantly from our intuitive expectations. The solution with conserved electron energy, Eq. (5-19), is less obvious. A similar sudden potential jump at the positive end of the accelerating region, though, has been described in Soviet literature (see Appendix). The continuous potential variation of Eq. (5-15) is associated with a "hybrid accelerator with closed electron drift," which is normally translated as a "Hall-current accelerator." The version where the potential jump is encountered is called an "accelerator with anode layer," with no equivalent type in U.S. literature. An experimental study was made in which both accelerator types were studied with essentially the same experimental apparatus.[4] (This Soviet paper by Bardadimov, et al., is included in the Appendix.) The only essential difference was that the insulator (item 2 in Fig. 1 of the Soviet paper) was included for the Hall-current accelerator and omitted for the anode-layer version. The presence of the insulator in close proximity to the accelerating channel would be expected to result in the collection of the higher energy electrons, and their replacement with lower energy secondaries. The presence of the insulator would thus be expected to correspond more to Eq. (5-15). Without the insulator, there would be a barrier of lower density plasma between the plasma in the accelerating channel and any solid surface. The electrons flowing back from the neutralizer would thus be expected to reach a higher temperature before escaping, and the acceleration process would be expected to correspond more to Eq. (5-19).

Numerical comparisons were also attempted. Using the Ar propellant points included in the table of Bardadimov, et al., and assuming that they correspond to Fig. 5-3 and the 400 V points of Fig. 5-2, Eq. (5-15) was found to be about 10 times higher than the experimental electron back-flow for the Hall-current accelerator, and Eq. (5-19) was found to be about three times higher than that of the anode layer accelerator. Inasmuch as the tabulated data used represent the product of some optimization, it is perhaps reasonable that the experimental values are lower than predictions based on mean experimental electron diffusion. The sensitivity of operation of such accelerators to optimization is indicated in another paper by Ivashchenko, et al.

Conclusions

Solutions were derived for ion accelerators with closed electron drift. Two classes of solutions were found, depending on whether the electron temperature is constant throughout the acceleration channel or it is allowed to rise as electrons flow toward the anode. In the latter case, a near discontinuous jump in potential is predicted at the positive end of the channel. Details of the acceleration process (such as the initial electron temperature) do change particulars of the calculated results. But the existence of the potential jump appears to be a persistent phenomenon when electron potential energy is converted into random energy.

The continuous potential solution associated with the assumption of constant electron temperature corresponds, from the experimental viewpoint, to the Hall-current accelerator. The solution with a potential jump near the anode corresponds to the anode-layer accelerator, described in Soviet literature.

References

1. H. R. Kaufman and R. S. Robinson, "Plasma Processes in Inert Gas Thrusters," AIAA Paper No. 79-2055, Oct./Nov. 1979.

2. L. Spitzer, Jr., Physics of Fully Ionized Gases, 2nd ed., Interscience Publishers, N.Y., 1962, pp. 47-48.

3. F. F. Chen, Introduction to Plasma Physics, Plenum Press, N.Y., 1974, p. 169.

4. N. A. Bardadimov, A. B. Ivashkin, L. V. Leskov, and A. V. Trofimov, "Hybrid Accelerator with Closed Drift of Electrons," IV All-Union Conference on Plasma Accelerators and Ion Injectors, Moscow, 1978.

5. S. S. Irashchenko, N. A. Mashtylev, and V. A. Tkachenko, "On Increased Stability of Parameters for Ionization Stage of Accelerator with Anode Layer, Ibid.

VI. CONCLUDING REMARKS

No reductions in discharge losses were obtained in any of a variety of bias experiments conducted with a multipole discharge chamber of an electrostatic thruster. This absence of any reductions in discharge losses was observed despite repeated demonstration of anode potentials more positive than the bulk of the discharge plasma.

The most promising trend in these bias experiments was the reduction of the penalty associated with biased anode operation as the magnetic integral above the biased anodes was increased. The obvious next step appears to be further bias tests with even higher magnetic integrals.

The use of hollow cathodes with assembled construction, as opposed to welded construction, appears practical. This approach is particularly promising for larger cathodes at higher missions, where the thermal expansion problems would be more serious with the present welded construction. Successful operation without emissive oxide offers the opportunity for accurate analyses of the electron emission and heat flow in a hollow cathode. Operation without oxide also offers the possibility of more reliable starting in programs where repeated or prolonged exposure to air after operation is a necessity.

As indicated in the Introduction, the study of the Hall-current accelerator represents a sharp departure from past work of this Grant. The experimental configuration of the Hall-current thruster that was tested had a uniform field throughout the ion generation and acceleration regions. To obtain reliable ion generation, it was necessary to reduce the magnetic field strength, to the point where excessive electron backflow was required to establish ion acceleration. This problem should be resolvable by using a nonuniform magnetic field strength, with ion generation restricted to a reduced field strength region. It also may be resolvable by the use of a more sophisticated electrode geometry in the ion generation region.

The theoretical study of ion acceleration with closed electron drift paths resulted in two classes of solutions. One class has the continuous potential variation in the acceleration region that is normally associated with a Hall-current accelerator. The other class has an almost discontinuous potential step near the anode end of the acceleration region. This step includes a significant fraction of the total acceleration potential difference. This latter class corresponds to the anode-layer accelerator in U.S.S.R. literature.

APPENDIX A

The five summary papers included in this Appendix were selected to show typical Soviet technology in what, in the U.S., would all be called Hall-current accelerators. These papers were presented in the *IV All-Union Conference on Plasma Accelerators and Ion Injectors*, sponsored by the U.S.S.R. Academy of Science, Scientific Council on the Combined Problems of Plasma Physics, Moscow, 1978. The papers were, in the order presented, pages 21-22, 25-26, 31-32, 35-36, and 68-69 in the Proceedings. Assistance from William Lewus in the translation of these papers is gratefully acknowledged.

ОБ УВЕЛИЧЕНИИ СТАБИЛЬНОСТИ ПАРАМЕТРОВ ФОРМИРУЮЩЕЙ СТУПЕНИ УСКОРИТЕЛЯ С АНОДНЫМ СЛОЕМ

Иващенко С.С., Маштылев Н.А., Ткаченко В.А.

В работе [I] показано, что при работе ускорителя с анодным слоем в низковольтных режимах (менее 500В) накладываются жесткие требования на стабильность параметров магнитной системы, формирующей ступени, ускоряющей ступени и расхода ионнообразующего материала (в данном случае – цезий). Особенно жесткие ограничения накладываются на параметры формирующей ступени. Уменьшение тока на величину более 2% от номинального значения приводит к срыву ускорительного режима, а увеличение тока в формирующей ступени приводит к значительному возрастанию тока утечки на полюса магнитной системы и, следовательно, снижению эффективности работы ускорителя. В случае применения источников питания с активными балластными элементами выдержать такие жесткие требования по стабильности параметров формирующей ступени довольно затруднительно. Анализ условий устойчивой совместной работы ускорителя и системы электропитания показывает, что для достижения максимальной устойчивости по формирующей ступени ускорителя с анодным слоем необходимо, чтобы внешняя характеристика системы электропитания соответствовала источнику тока. Экспериментально проверена работоспособность ускорителя с анодным слоем при питании формирующей ступени от двух источников с внешними характеристиками, приведенными на рис.I и рис.2. При питании формирующей ступени от источника тока (рис.2) отмечено значительное повышение устойчивой работы всей системы.

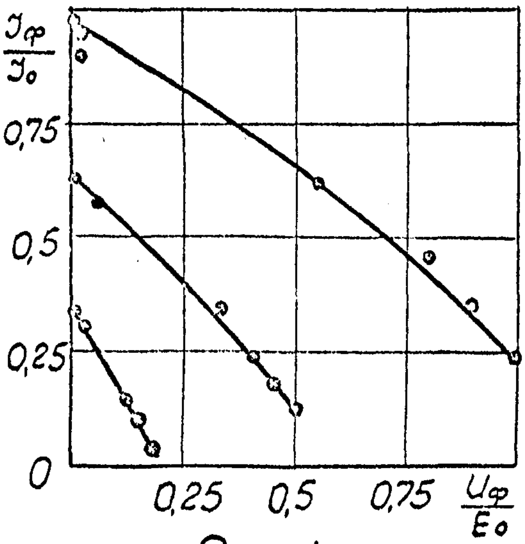

Рис.1

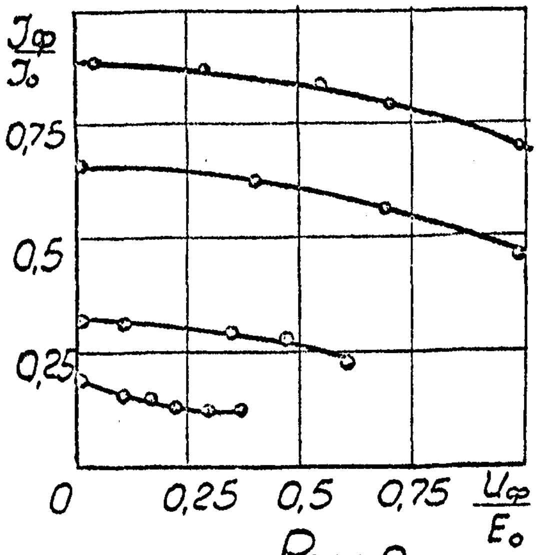

Рис.2

Литература

I. Иващенко С.С., Парщик А.С., Ткаченко В.А., Шипилов Ю.В. "Особенности работы ускорителя с анодным слоем в низковольтных режимах". Тезисы данного сборника.

ON INCREASE OF STABILITY OF PARAMETERS FOR IONIZATION STAGE OF ACCELERATOR WITH ANODE LAYER

S. S. Ivaschenko, N. A. Mashtylev, and V. A. Tkachenko

In the work of Ref. 1 is shown that during the operation of the accelerator with anode layer in low-voltage regimes (less than 500 V) there are imposed close requirements on the stability of the parameters of the magnetic system, which forms the acceleration of the stage and the discharge of ion-forming material (in this case cesium). Particularly close restrictions are imposed on parameters of the ion generation stage. A decrease of current at a value more than 2% from the nominal magnitude causes a breakdown of the acceleration regime, and an increase of the current in the forming stage causes considerable increase of current loss on the poles of the magnetic system and, consequently, a reduction in effectiveness of operation of accelerator. It is rather difficult to maintain such strict demands for stabilization of parameters of the ionization stage using power sources with active elements. An analysis of the conditions of stable joint operation of the accelerator and the system of the power supply shows that to attain the maximum stability for the ionization stage of the accelerator with an anode layer, it is necessary for the external characteristics of the power suppy system to correspond to a current source. The working capability of the accelerator with an anode layer using the ionization-stage supplies from two sources with (different) exterior characteristics, has been proven experimentally and is shown in Figs. 1 and 2. With power supplied to ionization stage from current sources (Fig. 2), there is noted a significant increase in the working stability of the entire system.

References

1. S. S. Ivaschenko, A. S. Parschik, V. A. Tkachenko, and Yu. V. Shipilov, "Working Features of Accelerator with Anode Layer in Low-Voltage Regime," Thesis of given (this) symposium.

In Fig. 1 and Fig. 2 (Рис. 1 and Рис. 2), I_ϕ/I_o and U_ϕ/E_o are the relative current and voltage of the discharge of ionization stage.

ХАРАКТЕРИСТИКИ ОДНОСТУПЕНЧАТОГО УСКОРИТЕЛЯ С АНОДНЫМ СЛОЕМ НА ЦЕЗИИ

В.И.Гаркуша, В.С.Ерофеев, Е.А.Ляпин
С.П.Чугина

В настоящей работе представлены характеристики одноступенчатого ускорителя с анодным слоем, использующего в качестве рабочего вещества цезий. Схематическое изображение модели и схема электропитания приведены на рис. I. В качестве катода на выходе ускорителя использовались либо прямонакальная вольфрамовая нить, либо специальный полый катод, также работающий на цезии. В случае выключенного катода минимальное разрядное напряжение составляло ~ 200 В. Использование катода позволило снизить напряжение менее чем до 20 В. Характеристики одноступенчатого аксиального ускорителя исследовались при изменении разрядного напряжения U_p от 20 до 200 В, магнитного поля H от 0,005 до 0,04 Тл при этом расход рабочего вещества поддерживался постоянным в течение всего эксперимента. В основном работа проводилась при расходе рабочего вещества в токовых единицах I÷3 А, но в ряде случаев он доводился до I0 А, при этом характеристики оставались аналогичными.

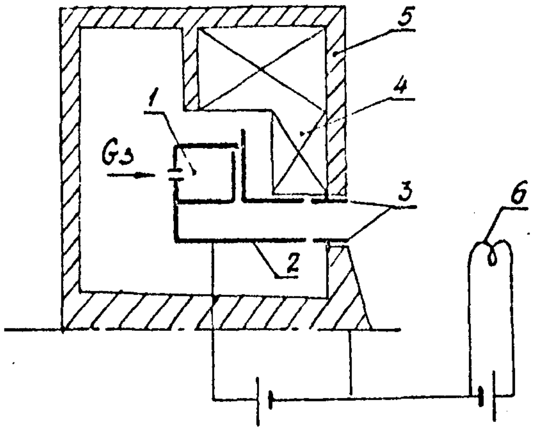

Рис. I
I-парораспределительная камера, 2-анод, 3-полюсные экраны, 4-катушка, 5-магнитопровод, 6-катод.

Вольт-амперная характеристика одноступенчатого ускорителя представлена на рис. 2. В области напряжений менее I00 В вольт-амперная характеристика падающая и ток разряда в два и более раза превышает величину расхода. При напряжении больше I00 В разрядный ток слабо зависит от напряжения и отношение разрядного тока к расходу на этом участке составляет ~ I,5.

На рис. 3 приведена зависимость среднемассовой скорости ионов от разрядного напряжения при различных расходах рабочего вещества. Разброс значений среднемассовой скорости от эксперимента к эксперименту составляет менее I0%. На этом же рисунке показана зависимость теоретического значения среднемассовой скорости от разрядного напряжения. Как видно, полученная из эксперимента среднемассовая скорость близка к теоретическому значению и к.п.д. ускорения составляет 0,75÷0,87, т.е. образующиеся ионы ускоряются электрическим полем соответствующим (0,75÷0,87)U_p.

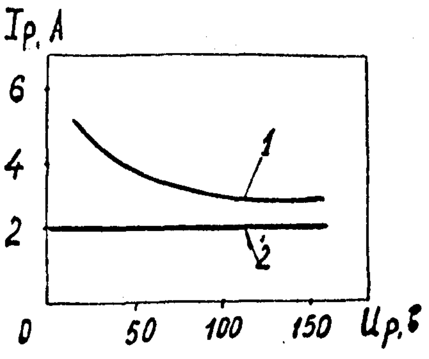

Рис. 2
I–вольт–амперная характеристика, 2–расход рабочего вещества
Q =2,I A.

В ходе исследования была снята зависимость I_p и среднемассовой скорости от магнитного поля. Они существенно зависят от величины магнитного поля и имеют оптимум при некотором значении $H_{\text{опт}}$. Это оптимальное значение в исследуемом диапазоне разрядного напряжения изменяется в пределах от 0,005 до 0,025 Тл.

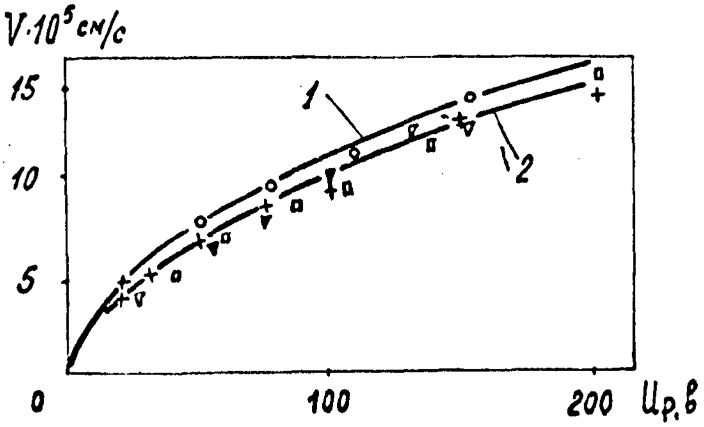

Рис. 3
I–расчетная кривая, 2–экспериментальная кривая (х – Q = 2,I A, ∇ – Q =I,76 A,
□ – Q =I,43 A).

CHARACTERISTICS OF SINGLE-STAGE ACCELERATOR WITH ANODE LAYER ON CESIUM

V. I. Garkusha, V. S. Yerofiev, E. A. Liapin, and S. P. Chugina

In this work are presented the characteristics of a single-stage accelerator with anode layer, which uses cesium as a working material. The schematic representation of the model and the power-supply scheme are presented in Fig. 1. As a cathode at the exit of the accelerator, use was made either of a directly heated tungsten filament or of a special hollow cathode, also working on cesium. In the event that the neutralizer was turned off, the minimum discharge voltage constituted about 200 V. Utilization of a cathode permitted a reduction of this voltage to less than 20 V. Characteristics of the single-stage axial accelerator were investigated with a variation of discharge voltage U_d from 20 to 200 V, of the magnetic field H from 0.005 to 0.04 Tesla, with the consumption of working material maintained constant in value for all of the experiment. The work was mainly conducted at a flow rate of working material in current units of 1 to 3 A, but in a number of cases it was brought up to 10 A, with the characteristics remaining similar.

Volt-ampere characteristics of single-stage accelerator are presented in Fig. 2. In the region of voltage less than 100 V, volt-ampere characteristics are decreasing and the current of discharge is two and more times greater in value than the flow. With a voltage of more than 100 V, the discharge current depends slightly on voltage, and the ratio of discharge current to flow in this range is about 1.5.

In Fig. 3 is presented the mean-mass velocity of ions as a function of discharge voltage for different flows of working material. The spread of values for mean-mass velocity from experiment to experiment constituted less than 10%. This drawing shows the dependence of theoretical value of mean-mass velocity on discharge voltage. As is seen, the obtained mean-mass velocity is close to the theoretical value, and coefficient of useful operation constitutes 0.75-0.87. That is, the ions generated are accelerated by means of an electric field corresponding to (0.75-0.87) U_d.

In the course of the investigation was gathered the dependence of I_d and mean-mass velocity on magnetic field. They essentially depend on the value of the magnetic field and there exists an optimum with some value H_{OPT}. This optimum value in the investigated range of discharge voltage varied from 0.005 to 0.025 Tesla.

In Fig. 1 (Рис. 1): 1 is the gas distributor, 2 is the anode, 3 are the pole screens, 4 is the magnet winding, 5 is the magnetic circuit, and 6 is the cathode. The left-hand power supply in Fig. 1 is the discharge power supply. In Fig. 2 and Fig. 3 (Рис. 2 and Рис. 2); I_p,A and U_p,B are discharge current I_d in Amp and discharge voltage U_d, in V; while V in cm/c is velocity V in cm/sec. In Fig. 3, 1 is the calculated curve and 2 is the experimental curve, while Q is the flow rate in A-equiv.

О ВЛИЯНИИ НАПРАВЛЕНИЯ ПОДАЧИ РАБОЧЕГО ВЕЩЕСТВА НА ХАРАКТЕРИСТИКИ РАЗРЯДА С АНОДНЫМ СЛОЕМ

С.Д.Гришин, В.К.Калашников, Ю.В.Саночкин

Экспериментальные исследования свойств $E \perp H$ разряда с замкнутым дрейфом электронов указывают, что направление подачи рабочего вещества существенно влияет на структуру анодного слоя /I,2/. Подробнее изучен разряд в ускорителях, где подача вещества осуществляется через анод (случай А). Обратный случай подачи (случай Б) теоретически исследован значительно слабее. Поэтому представляет интерес решение задачи для случаев А,Б и сравнение результатов. Рассмотрение проводилось в диффузионном приближении. Для А использовалась система уравнений и граничных условий /3/, для Б они имеют следующий вид: $\frac{dj_e}{ds} = q n_e$, $\frac{dj_i}{ds} = -q n_e$,

$$\varkappa \frac{d^2\eta}{ds^2} = n_e - n_i, \quad q = \sqrt{j_i^2 - N_0^2}, \quad j_e = q n_e \frac{d\eta}{ds}, \quad N_0 = q(s_0),$$

$$n_i = \beta \int_s^{s_0} \frac{q' n' ds'}{\sqrt{\eta' - \eta + \varepsilon}}, \quad \beta = \frac{n_0}{\omega_e}\left(\frac{M}{2m}\langle\sigma_i v_e\rangle\langle\sigma_0 v_e\rangle\right)^{\frac{1}{2}}, \quad \varkappa = \frac{m\omega_e}{4\pi e^2}\left(\frac{e\varphi_0}{m v_0^2}\right)^{\frac{1}{2}} \frac{\langle\sigma_i v_e\rangle^{\frac{3}{2}}}{\langle\sigma_0 v_e\rangle^{\frac{1}{2}}}.$$

$$\eta(0) = \eta'(0) = 0, \quad j_e(0) = 0, \quad j_i(s_0) = 0.$$

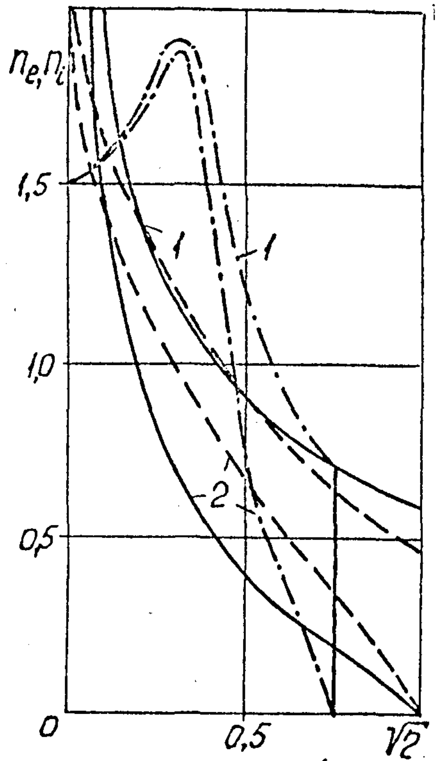

Рис. 1

Решение дало распределение по слою основных характеристик разряда и их изменение с ростом расхода для различных величин магнитного поля. На рисунках сплошные линии соответствуют случаю Б, пунктирные – А, штрихпунктирные – Б, но с учетом реальности процессов – зависимости частоты ионизации от энергии электронов, потерь энергии электронов и наличия области срыва у анода. На рис.I даны распределения n_e (кривая I) и n_i (кривая 2) в зависимости от потенциала η для

$\varkappa$ =0,2 и β =0,8, типичные в широком диапазоне изменения параметров $\varkappa$ и β . На рис.2 показаны профили потока нейтралов $q(z)$ для различных β (цифры на кривых). В случае Б максимум концентраций n_0 и n_e в начале слоя и поэтому здесь реализуются условия для наибольшей скорости ионизации. С ростом расхода область, в которой ионизуется основная часть нейтралов, в отличие от А смещается к началу слоя. Кроме того, низкая энергия электронов в начале слоя и монотонное убывание $S_0(\beta)$ (рис.3, цифры на кривых – значения $\varkappa$) указывают на то, что учет реальности вышеупомянутых процессов для случая Б более важен. Расчеты, проведенные с их учетом подтверждают это, давая значения $S_0 \simeq 2 \div 3$ и средней энергии электронов ~ 0,2. Электрическое поле E и электронный ток j_e в случае Б растут быстрее и у анода имеют большие величины в широком диапазоне чисел β . Анализ результатов показывает, что перемена направления подачи вносит ряд существенных изменений в структуру анодного слоя.

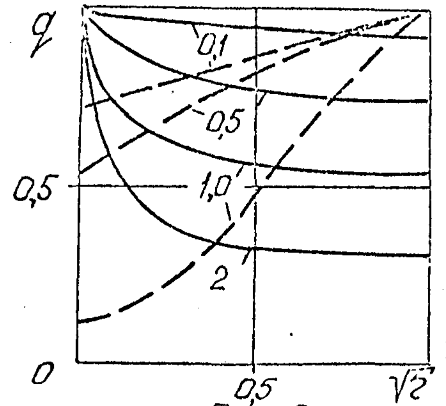

Рис. 2

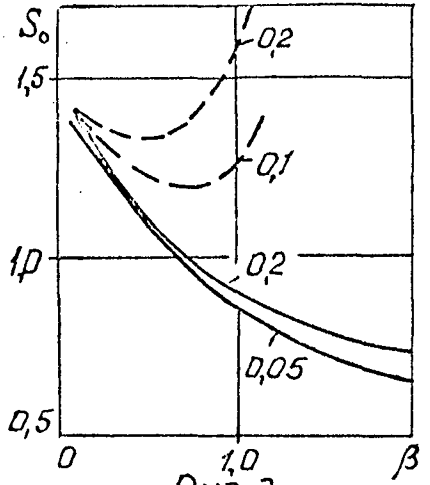

Рис. 3

1. Н.А.Кервалишвили, А.В.Жаринов. Характеристики разряда низкого давления в поперечном магнитном поле. ЖТФ, 35, вып.12, 1965.
2. Плазменные ускорители с замкнутым дрейфом. Материалы II Всесоюзной конф. по плазменным ускорителям. Минск, изд.Ин-та физики АН БССР, стр.126.
3. В.С.Ерофеев, Ю.В.Саночкин, С.С.Филиппов. Прианодный электрический слой в разряде с замкнутым холловским током. ПМТФ, 5, 69.

THE EFFECT OF DIRECTION OF SUPPLY OF WORKING MATERIAL ON CHARACTERISTICS OF DISCHARGE WITH ANODE LAYER

C. D. Grishin, V. K. Kalashnikov, Yu. V. Sanochkin

Experimental investigations of the properties of E × H discharge with closed drift of electrons indicate that the direction of supply of working material essentially affects the structure of the anode layer, Refs. 1 and 2. Detailed study was made of the discharge in accelerators where the flow of material occurs through the anode (case A). Reverse case of supply (case B) has been theoretically studied significantly less. Therefore the answer is of interest for the problem of cases A and B, and the comparison of results. The treatment was carried out in the diffusion approximation. For A, use was made of a system of equations and of boundary conditions, Ref. 3, for B they exhibit the following appearance:

$$\frac{dj_e}{ds} = qn_e, \quad \frac{dj_i}{ds} = -qn_e,$$

$$H\frac{d^2\eta}{ds^2} = n_e - n_i, \quad q = \sqrt{j_i^{\,2} - N_o^{\,2}}\ , \quad j_e = qn_e\frac{d\eta}{ds}\ , \quad N_o = q(s_o)\ ,$$

$$n_i = \beta \int_s \frac{q'n'ds'}{\sqrt{\eta' - \eta + \varepsilon}}\ , \quad \beta = \frac{n_o}{\omega_e}\left(\frac{M}{2m}<\sigma_i v_e><\sigma_o v_e>\right)^{1/2}\ ,$$

$$H = \frac{m\omega_e}{4\pi e^2}\left(\frac{e\phi_o}{mv_o^{\,2}}\right)^{1/2}\frac{<\sigma_i v_e>^{3/2}}{<\sigma_o v_e>^{1/2}}\ ,$$

$$\eta(o) = \eta'(0) = 0, \quad j_e(o) = 0, \quad j_i(s_o) = 0 .$$

The solution gave the distribution over the layer of the fundamental characteristics of the discharge and their variation with increase of discharge for various values of magnetic field. In the illustrations the continuous lines correspond to case B, the dashed lines to case A, and the dot-dash lines to case B, but with account taken of real processes - the dependence of ionization frequency on electron energy, and existence of breakdown at the anode. In Fig. 1 is given the distribution of n_e (curve 1) and of n_i (curve 2) in terms of potential η for $H = 0.2$ and $\beta = 0.8$, typical for a wide range of variation of parameters of H and β. In Fig. 2 are shown profiles of neutral flow $q(\eta)$ for various β (numbers on curves). In case B, the maximum concentration of n_o and n_e is in the beginning of the layer, and therefore here is realized the condition for the greatest rate of ionization. With increase of discharge, the region in which the majority of neutrals is ionized, in contrast to A, is displaced to the beginning of the layer. Apart from that, low energy of electrons in beginning of layer and monotonic decrease of $s_o(\beta)$ (Fig. 3, numbers on curves are values of H) indicate that the effects of the above mentioned real processes are more important for case B. Calculations carried out with the inclusion of these effects confirm this, giving values of $s_o \approx 2$-3 and mean electron energy of ~ 0.2. The electric field E and electron current j_e in case B increase more quickly and at the anode exhibit greater values in a wide range of quantities than of β. Analysis of the results shows that change of the direction of supply brings about a sequence of important changes in the anode layer structure.

ЗОНДОВЫЕ ИССЛЕДОВАНИЯ РАСПРЕДЕЛЕНИЯ ПАРАМЕТРОВ В КАНАЛЕ УЗДП

А.И.Бугрова, В.С.Версоцкий, В.К.Харчевников

Распределения концентрации n_e и температуры T_e электронов, а также потенциала плазмы φ_n измерялись с помощью электростатического зонда по стандартной схеме. Торцевой зонд устанавливался на различных расстояниях от анода и с помощью координатного устройства перемещался по радиусу модели.

Зондовые вольтамперные характеристики обрабатывались согласно методик предложенных в работах /I-2/.

Как известно, метод обработки зондовой характеристики по Бому применим в том случае, когда температура T_e больше температуры ионов T_i . Данные условия соблюдаются в области канала близкой к аноду. В зоне ионизации ионы набирают энергию порядка потенциала и соотношение $T_e \gg T_i$ не выполняется.

Поэтому в выходной части канала вольтамперные характеристики зонда были обработаны по методике, предложенной Лафрамбуазом и Сонином.

Из анализа кривых распределения температуры и концентрации электронов по длине канала (фиг.I) следует, что n_e и T_e принимают экстремальные значения, положения которых зависят от режима работы модели.

Характерной особенностью является некоторое смещение максимальных значений n_e по сравнению с максимальными значениями T_e в область более удаленную от анода.

Максимальное значение температуры электронов определяется напряжением разряда и с увеличением U_p значения T_e увеличиваются. Распределение температуры электронов по радиусу модели свидетельствует об увеличении T_e вблизи внутренней стенки канала.

Пунктирными линиями на фиг.I показано распределение концентрации электронов, полученное при обработке вольтамперной характеристики зонда по Лафрамбуазу. Видно, что в этом случае в выходной части канала концентрация электронов имеет более пологий спад и большую абсолютную величину. При этом область максимальных значений n_e еще более смещается к срезу. Для сравнения сплошной линией обозначено распределение концентрации, полученное по Бому. Точками отмечены результаты вычислений n_e и T_e по функции распределения электронов (ФРЭ) по энергиям. ФРЭ была получена двойным радиотехническим дифференцированием зондовой характеристики /3/ .

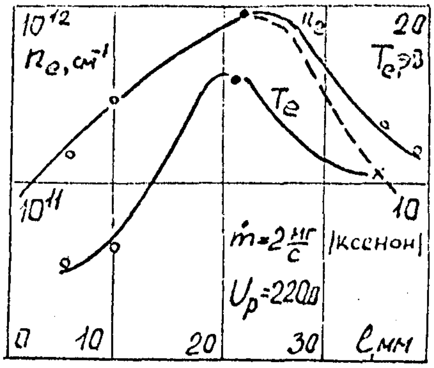

Фиг.1

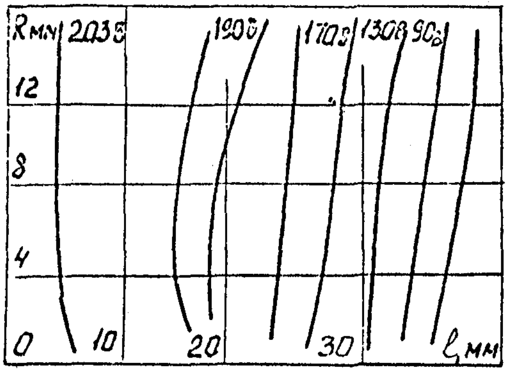

Фиг. 2

Потенциал плазмы рассчитывался из зондовых характеристик и сравнивался с результатами, полученными горячим зондом. Картина эквипотенциальных линий представлена на фиг.2. Распределение потенциала плазмы по длине канала показало, что его величина незначительно изменяется до зоны ионизации. В зоне ионизации происходит спад потенциала и на выходе канала $\varphi_и$ имеет значения порядка 25–40 в.

1. „Диагностика плазмы" под. ред. Хаддстоуна Р., Москва 1967 г.
2. Sonin AAIA journal n 9, 1966.
3. А.И. Бугрова и др. III Всесоюзн. конф. по плазменным ускорителям, Минск 1976.

PROBE INVESTIGATION OF THE DISTRIBUTION OF PARAMETERS IN THE CHANNEL OF UZDP*

A. I. Bugrova, V. S. Versotskii, and V. K. Kharchevnikov

The distribution of concentration n_e and of temperature T_e of electrons, and also the potential of the plasma ϕ_p was measured with the aid of an electrostatic probe of standard design. The end-facing probe was mounted at various distances from the anode and with the aid of a coordinate mechanism was displaced over the radius of the model.

Probe volt-ampere characteristics were processed according to the procedure in Refs. 1 and 2.

As is well known, the method of analysis of probe characteristics of Bohm applies in the case where the temperature T_e is greater than the temperature of the ions T_i. These given conditions are observed in the region of the channel near the anode. In the zone of ionization, ions gather energy approximately with the potential, and the relationship $T_e >> T_i$ is not carried out.

Therefore in the exit region of the channel, volt-ampere characteristics of the probe were processed by the procedure proposed by Laframbois and Sonin.

From the analysis, of curves of temperature and concentration distribution over the length of the channel (Fig. 1) it follows that

---

*UZDP is an accelerator with closed drift of electrons and extended acceleration zone.

n_e and T_e assume experimental values, with status which depends on the working regime of the model.

As a characteristic feature there appears some displacement of maximum value n_e by comparison with maximum values T_e in the region more remote from the anode.

Maximum value of electron temperature is determined by electric stress of the discharge and with increase of U_d the values of T_e are increased. The distribution of electron temperature over the radius of the model indicates the increase of T_e near the inside wall of the channel.

The dashed line in Fig. 1 shows the distribution of electron concentration, obtained during analysis of the volt-ampere characteristics of the probe by Lafrombois. As is seen, in this case, in the exit region of the channel, the concentration of the electrons has more of a gentle fall and a more absolute value. In this case, the region of maximum values of n_e is still more displaced at the edge. For comparison of the solid line, there was designated the distribution of concentration, obtained according to Bohm. Dots mark the calculated n_e and T_e by function of the distribution of electrons (FDE) by energy. FDE was produced by double differentiation of probe characteristics (Ref. 3).

The potential of the plasma was calculated out of probe characteristics and compared with the results obtained with a hot probe. The picture of equipotential lines is presented in Fig. 2. The distribution of plasma potential over the length of the channel shows that the variation changes insignificantly up to the ionization zone. In the ionization zone there occurs a decrease of potential and at the exit of the channel ϕ_p exists at values of about 25-40 V.

References

1. "Diagnostics of Plasmas," ed. R. Khaddstouna, Moscow, 1967.

2. Sonin, AAIA (probably should be AIAA) Journal, No. 9, 1966.

3. A. I. Bugrova et al., IIIrd All-Union Conference on Plasma Accelerators, Minsk, 1976.

In Fig. 1 (Рис. 1), the electron density n_e in cm^{-3} (cm^{-1} looks like a mistake) and T_e in eV (T_e, эВ) are plotted against ℓ in mm for a mass flow rate $\dot{m}$ of 2 mg/sec of xenon at a discharge potential U_d of 220 V (U_p = 220 B). In Fig. 2 (Рис. 2) equipotential lines at constant voltages (B) are plotted in terms of radius R in mm and length ℓ in mm.

Гибридный ускоритель с замкнутым дрейфом электронов

Н.А Бардадымов, А.Б. Ивашкин, Л.В. Лесков
А.В. Трофимов

В работе приводятся результаты экспериментального исследования гибридного ускорителя с замкнутым дрейфом электронов (УЗДГ) и дано сравнение с рабочими характеристиками ускорителя с анодным слоем одноступенчатого типа (УАС).

Схема конструкции экспериментальной модели УЗДГ показана на Рис.I Компенсация объемного заряда ионов на выходе ускорителя производилась при помощи плазменного цезиевого нейтрализатора. Модель УАС отличалась от модели УЗДГ только отсутствием диэлектрических вставок 2,поэтому длина ускорительного канала УАС составляла -9мм.Межэлектродный зазор анод-катоды был- Iмм.

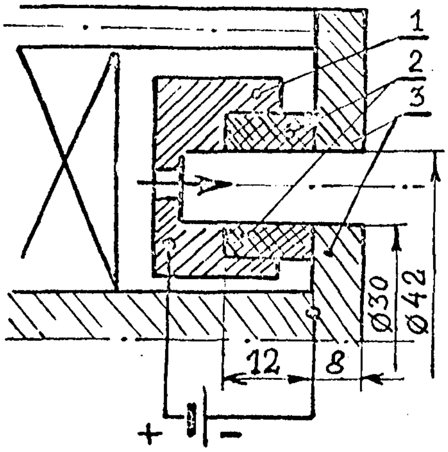

Рис.1 1 - анод; 2 - диэлектрические вставки; 3 - катоды.

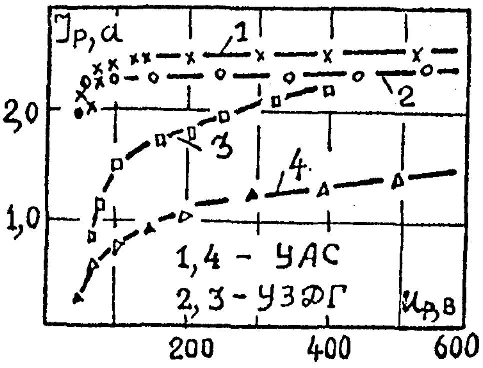

Рис.2 В А Х разряда.
1,2-Ar, $\dot{m}$ = 0,84мг/сек;
3,4-H_2, $\dot{m}$ = 0,35мг/сек.

Исследования модели УЗДГ проводились с целью пространственного разделения зон ионизации и ускорения в одноступенчатом ускорителе,с тем чтобы приблизить его характеристики к результатам,достигнутым на двухступенчатом УАС I . Кроме того, некоторое увеличение общей длины ускорительного канала за счет диэлектрических вставок 2 должно способствовать увеличению вероятности ионизации рабочих тел с малой атомной массой - и др. В ускорителе с анодным слоем длина ускорительного канала составляют порядка α_i является достаточно малой,

$$\alpha \simeq \rho_e(U_p)\cdot\sqrt{\nu_0/\nu_i}\ ; \qquad (I)$$

вследствие чего в низковольтном режиме эффективность ионизации легких атомов низка.

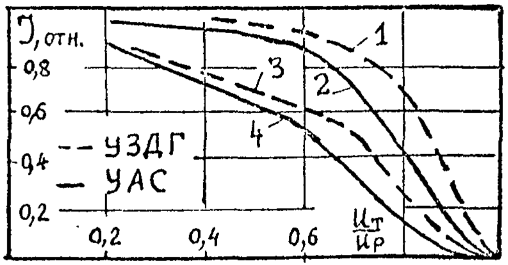

Рис.3 U_p=400в; 1,2-Ar; $\dot{m}$=0,84 мг/сек; 3,4-H_2; $\dot{m}$=0,35мг/сек.

Таблица 1.

	УЗДГ			УАС		
	Ar	Ne	H_2	Ar	Ne	H_2
$j_i, \frac{a}{см^2}$	0,29	0,31	0,25	0,28	0,20	0,15
$\dot{m}_s, \frac{a}{см^2}$	0,3	1,0	2,6	0,3	1,0	2,6
J_i, a	2,0	2,2	1,8	1,9	1,5	1,1
H_0, э	200	100	70	300	200	180

Сравнение вольтамперных характеристик разряда(ВАХ) на аргоне,на котором была достигнута вероятность ионизации $P_i \cong 1$ на обеих моделях,показывает,что последние практически идентичны для одного и того же режима разряда,Рис.2 При P_i<0,2 ВАХ разряда обеих моделей являются растущими,см.кривые 3 и 4-водород,но в случае УЗДГ ВАХ разряда смещена в сторону бо́льших значений J_p.Как следует из результатов измерений энергии ионов в пучке,Рис.3,ионообразование в прианодной области выше в УЗДГ и,соответственно,средняя энергия ионов является более высокой по сравнению с УАС.В таблице I приведены характерные величины магнитного поля H_0 и максимально достигнутые значения интенсивности j_i и полного тока J_i пучка в стационарном режиме.Расходимость ионов Ar, Ne, H_2 при условии, что $0{,}85\cdot J_{i/2}$ заключено в угол $\alpha/2$,не превышала 10° на обеих моделях.Максимальное отношение J_i/J_p для УЗДГ и УАС составляло 0,9 и 0.8 соответственно.

1. В.С.Ерофеев, Л.В.Лесков в кн."Физика и применение плазменных ускорителей", стр.18-47, г.Минск, 1974г.

HYBRID ACCELERATOR WITH CLOSED DRIFT OF ELECTRONS

N. A. Bardadimov, A. B. Ivashkin, L. V. Leskov, and A. V. Trofimov

In this paper, the results of an experimental investigation of a hybrid accelerator with closed electron drift (Hall-current accelerator, HCA) are shown and compared with the working characteristics of an accelerator with anode layer of the single-stage type (anode-layer accelerator, ALA).

The scheme of construction for the experimental model of the HCA is shown in Fig. 1. Volume neutralization of the ions leaving the accelerator is obtained with a cesium plasma neutralizer. The ALA model differs from the HCA model only in the absence of the dielectric inserts 2 (Fig. 1). The length of the acceleration channel of the ALA is 9 mm. The interelectrode anode-cathode spacing was 1 mm.

Investigations of the HCA model were carried out with the goal of showing an ionization and single-stage acceleration zone, to bring its characteristics closer to the results obtained with the two-stage ALA I. Some increase in the overall length of the accelerator channel due to the dielectric insert 2 should increase the probability of ionization of working gases with small atomic masses, and closely related materials. In the ALA model, the length of the acceleration channel constitutes of the order of d,[1] and appears rather small,

$$d \sim \rho_e (U_d) \quad \nu_o/\nu_i \tag{1}$$

because in the low-voltage regime the efficiency of ionization of light atoms is low. Comparison of voltampere characteristics of the discharge with argon, with which ionization probability approached unity for both models, shows that the latter are practically identical for both (Fig. 2). With a probability of ionization of <0.2, the voltampere characteristics of both models are seen to increase - see curves 3 and 4, for hydrogen. But in the case of the HCA, the voltampere characteristics are displaced upwards in I_d. As shown by the measurements of ion-energy distribution, Fig. 3, the ions are formed more in the near-anode region for the HCA and, accordingly, the mean ion energy of ions appears higher than for the ALA. In Table 1, the typical values of magnetic field H_o and maximum attained values of intensity j_i and of field current I_i are shown for several operating conditions in the steady-state regime. The angular dispersion of ions of Ar, Ne, and H_2 did not exceed 10° in both models, with $0.85\ I_i/2$ included in this angle of $\alpha/2$. The maximum ratio of I_i/I_d for the HCA and the ALA agreed within a factor of 0.9 to 0.8.

References

1. V. C. Erofiev, L. V. Leskov, in Physics and Applications of Plasma Accelerators, pp. 18-47, Minsk, 1974.

In Fig. 1 (Рис. 1) all dimensions are in mm, with dimensions preceded by ϕ diameters. Also 1 is the anode, 2 are the dielectric spacers, and 3 is the cathode. In Fig. 2 (Рис. 2), I_p,a and U_p,B are the discharge current I_d in A and discharge potential U_d in V, while

УAC is the anode layer accelerator and УЗДГ is the Hall-current accelerator (hybrid accelerator with closed drift of electrons). The Ar flow rate is 0.84 mg/sec (curves 1 and 2), and the H_2 flow rate is 0.35 mg/sec (curves 3 and 4). For Fig. 3 I_{OTH} is the normalized (relative) current I_{rel}, while U_T/U_p is the ion formation (creation) voltage divided by the discharge voltage. The flow rates $\dot{m}$ are again 0.84 mg/sec for Ar and 0.35 mg/sec for H_2, and the discharge potential U_d (U_p) is 400 V. In Table 1 (Таблица 1) УЗДГ is again the Hall current accelerator and УAC is the anode layer accelerator. At the left of the table, j_i is ion current density in A/cm^2, $\dot{m}_s$ is the mass flow density in A/cm^2, I_a is the total ion current in A, and H_o is the magnetic field in Oersted.

DISTRIBUTION

	Copies
National Aeronautics and Space Administration	
Washington, DC 20546	
Attn: RS/Mr. Dell Williams, III	1
RTS-6/Mr. Wayne Hudson	1
RTS-6/Mr. Jerome Mullin	1
MT/Mr. Ivan Bekey	1
National Aeronautics and Space Administration	
Lewis Research Center	
21000 Brookpark Road	
Cleveland, OH 44135	
Attn: Research Support Procurement Section	
Mr. G. Golinski, MS 500-306	1
Technology Utilization Office, MS 3-19	1
Report Control Office, MS 5-5	1
Library, MS 60-3	2
Mr. N. Musial, MS 500-113	1
Dr. M. Goldstein, Chief Scientist, MS 5-3	1
Mr. T. Cochran, MS 501-8	1
Mr. D. Petrash, MS 501-5	1
Mr. N. Grier, MS 501-7	1
Mr. M. Mirtich, MS 501-7	1
Mr. R. Finke, MS 77-4	1
Mr. B. Banks, MS 501-7	1
Mr. D. Byers, MS 501-7	1
Mr. W. Kerslake, MS 501-7	1
Mr. V. Rawlin, MS 501-7	30
National Aeronautics and Space Administration	
Marshall Space Flight Center	
Huntsville, AL 35812	
Attn: Mr. Jerry P. Hethcoate	1
Mr. John Harlow	1
Mr. John Brophy	1
Mr. Robert T. Bechtel	1
Mr. M. Ralph Carruth, Jr.	1
NASA Scientific and Technical Information Facility	
P.O. Box 8757	
Baltimore, MD 21240	
Attn: Accessioning Department	1
National Aeronautics and Space Administration	
Goddard Space Flight Center	
Greenbelt, MD 20771	
Attn: Mr. W. Isley, Code 734	1
Dr. David H. Suddeth	1

National Aeronautics and Space Administration
Ames Research Center
Moffett Field, CA 94035
Attn: Technical Library 1

National Aeronautics and Space Administration
Langley Research Center
Langley Field Station
Hampton, VA 23365
Attn: Technical Library 1
Mr. B. Z. Henry 1

The Aerospace Corporation
P.O. Box 95085
Los Angeles, CA 90045
Attn: Dr. B. A. Haatunion 1
Mr. A. H. Silva 1

The Aerospace Corporation
Space Sciences Laboratory
P.O. Box 92957
Los Angeles, CA 90009
Attn: Dr. Y. T. Chiu 1

Bell Laboratories
600 Mountain Avenue
Murray Hill, NJ 07974
Attn: Dr. Edward G. Spencer 1
Dr. Paul H. Schmidt 1

Boeing Aerospace Company
P.O. Box 3999
Seattle, WA 98124
Attn: Mr. Donald Grim, MS 8K31 1
Mr. Russell Dod 1

Case Western Reserve University
10900 Euclid Avenue
Cleveland, OH 44106
Attn: Dr. Eli Reshotko 1

C.E.N.-F.A.R.
Service Du Confinement Des Plasmas
BP6
92260 Fontenay-Aux-Roses,
FRANCE
Attn: J. F. Bonnal 1

Circuits Processing Apparatus, Inc.
725 Kifer Road
Sunnyvale, CA 94086
Attn: Spencer R. Wilder 1

Commonwealth Scientific Corporation
500 Pendleton Street
Alexandria, VA 22314
Attn: George R. Thompson 1

Computing Center of the USSR Academy of Sciences
Vavilova 40
117333 Moscow, B-333
USSR
Attn: Dr. V. V. Zhurin 1

Comsat Corporation
950 L'Enfant Plaza, S.W.
Washington, DC 20024
Attn: Mr. Sidney O. Metzger 1

COMSAT Laboratories
P.O. Box 115
Clarksburg, MD 20734
Attn: Mr. B. Free 1
Mr. O. Revesz 1

CVC Products
525 Lee Road
P.O. Box 1886
Rochester, NY 14603
Attn: Mr. Georg F. Garfield, Jr. 1

DFVLR - Institut fur Plasmadynamik
Technische Universitat Stuttgart
7 Stuttgart-Vaihingen
Allmandstr 124
WEST GERMANY
Attn: Dr. G. Krulle 1

DFVLR - Institut fur Plasmadynamik
33 Braunschweig
Bienroder Weg 53
WEST GERMANY
Attn: Mr. H. Bessling 1

EG & G Idaho
P.O. Box 1625
Idaho Falls, ID 83401
Attn: Dr. G. R. Longhurst, TSA-104 1

Electro-Optical Systems, Inc.
300 North Halstead
Pasadena, CA 91107
Attn: Dr. R. Worlock 1
Mr. E. James 1
Mr. W. Ramsey 1

Electrotechnical Laboratory
1-1-4, Umezono, Sakura-Mura,
Niihari-Gun
Ibaraki,
JAPAN
Attn: Dr. Katsuya Nakayama 1

Fairchild Republic Company
Farmingdale, NY 11735
Attn: Dr. Domenic J. Palumbo 1

Ford Aerospace Corporation
3939 Fabian Way
Palo Alto, CA 94303
Attn: Mr. Robert C. Kelsa 1

General Dynamics
Kearney Mesa Plant
P.O. Box 1128
San Diego, CA 92112
Attn: Dr. Ketchum 1

Giessen University
1st Institute of Physics
Giessen,
WEST GERMANY
Attn: Professor H. W. Loeb 1

Hughes Aircraft Company
Space and Communication Group
P.O. Box 92919
Los Angeles, CA 90009
Attn: Dr. B. G. Herron 1

Hughes Research Laboratories
3011 Malibu Canyon Road
Malibu, CA 90265
Attn: Mr. J. H. Molitor 1
Dr. R. L. Poeschel 1
Dr. Jay Hyman 1
Mr. R. Vahrenkamp 1
Dr. J. R. Beattie 1
Dr. W. S. Williamson 1

IBM Corporation
Thomas J. Watson Research Center
P.O. Box 218
Yorktown Heights, NY 10598
Attn: Dr. Jerome J. Cuomo 1
Dr. James M. E. Harper 1

IBM East Fishkill
D/42K, Bldg. 300-40F
Hopewell Junction, NY 12533
Attn: Mr. James Winnard 1

Ion Beam Equipment, Inc.
P.O. Box O
Norwood, NJ 07648
Attn: Dr. W. Laznovsky 1

Jet Propulsion Laboratory
4800 Oak Grove Drive
Pasadena, CA 91102
Attn: Dr. Kenneth Atkins 1
Technical Library 1
Mr. Eugene Pawlik 1
Mr. James Graf 1
Mr. Dennis Fitzgerald 1
Dr. Graeme Aston 1

Joint Institute for Laboratory Astrophysics
University of Colorado
Boulder, CO 80302
Attn: Dr. Gordon H. Dunn 1

Kyoto University
The Takagi Research Laboratory
Department of Electronics
Yoshidahonmachi Sakyo-ku
Kyoto 606,
JAPAN
Attn: Dr. Toshinori Takagi 1

Lawrence Livermore Laboratory
Mail Code L-437
P.O. Box 808
Livermore, CA 94550
Attn: Dr. Paul Drake 1

Lockheed Missiles and Space Company
Sunnyvale, CA 94088
Attn: Dr. William L. Owens
Propulsion Systems, Dept. 62-13 1
Mr. Carl Rudey 1

Massachusetts Institute of Technology
Room 13-3061
77 Massachusetts Avenue
Cambridge, MA 02139
Attn: Henry I. Smith 1

University of New Mexico
Department of Electrical Engineering
Albuquerque, NM 87131
Attn: Dr. Robert McNeil 1

Optic Electronics Corporation
11477 Pagemill Road
Dallas, TX 75243
Attn: Bill Hermann, Jr. 1

Physicon Corporation
221 Mt. Auburn Street
Cambridge, MA 02138
Attn: H. von Zweck 1

Princeton University
Princeton, NJ 08540
Attn: Mr. W. F. Von Jaskowsky 1
Dean R. G. Jahn 1
Dr. K. E. Clark 1

Research and Technology Division
Wright-Patterson AFB, OH 45433
Attn: (ADTN) Mr. Everett Bailey 1

Rocket Propulsion Laboratory
Edwards AFB, CA 93523
Attn: LKDA/Mr. Tom Waddell 1
LKDH/Dr. Robert Vondra 1

Royal Aircraft Establishment
Space Department
Farnborough, Hants
ENGLAND
Attn: Dr. D. G. Fearn 1

Sandia Laboratories
Mail Code 5743
Albuquerque, NM 87115
Attn: Mr. Ralph R. Peters 1

Tektronix, 50-324
P.O. Box 500
Beaverton, OR 97077
Attn: Curtis M. Haynes 1

Texas Instruments, Inc.
MS/34
P.O. 225012
Dallas, TX 75265
Attn: Larry Rehn 1

TRW Inc.
TRW Systems
One Space Park
Redondo Beach, CA 90278
Attn: Dr. M. Huberman 1
Mr. Sid Zafran 1

United Kingdom Atomic Energy Authority
Culham Laboratory
Abingdon, Berkshire
ENGLAND
Attn: Dr. P. J. Harbour 1
Dr. M. F. A. Harrison 1
Dr. T. S. Green 1

University of Tokyo
Department of Aeronautics
Faculty of Engineering
7-3-1, Hongo, Bunkyo-ku
Tokyo,
JAPAN
Attn: Prof. Itsuro Kimura 1

Veeco Instruments, Inc.
Terminal Drive
Plainview, NY 11803
Attn: Norman Williams 1

University of Iowa
Department of Physics
Iowa City, IA 52242
Attn: Dr. R. T. Carpenter 1